UNIVERSITY
OF TRENTO - Italy

Department of Materials Engineering
and Industrial Technologies

Doctorate School in Materials Engineering – XXI cycle

Advances in the Production of Planar and Micro-Tubular Solid Oxide Fuel Cells

Marco Cologna

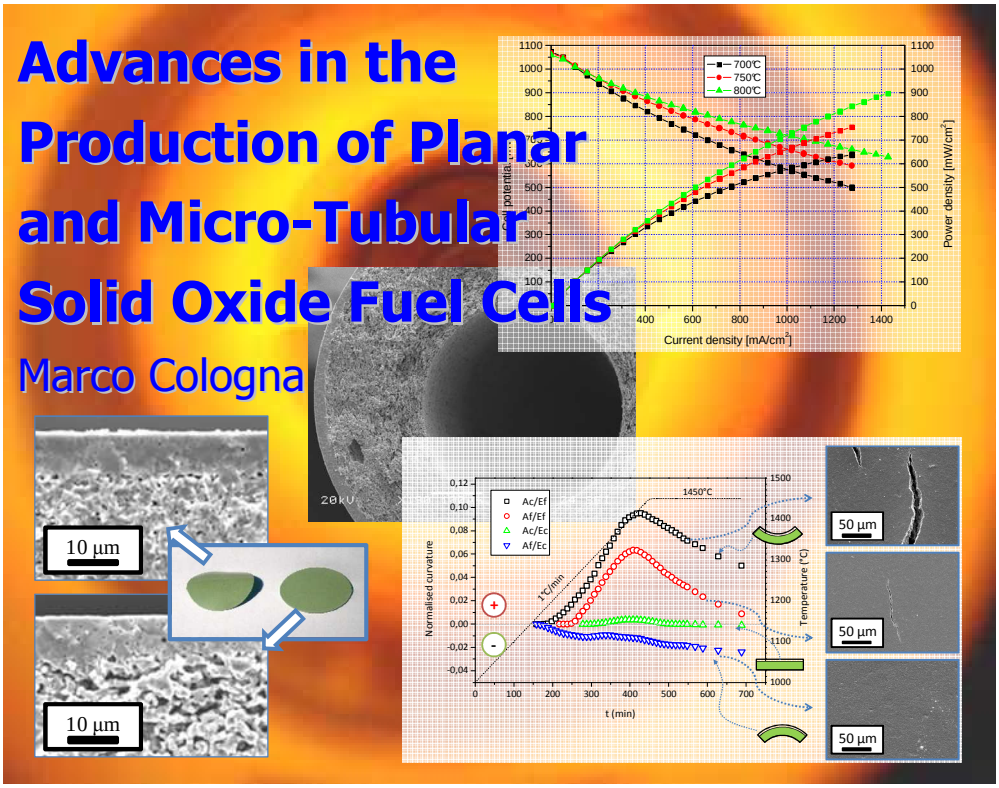

April 2009

Doctoral thesis

Advances in the Production of Planar and Micro-Tubular Solid Oxide Fuel Cells

Marco Cologna

Advisor:
Prof. Ing. V. M. Sglavo

Doctoral Committee:

Prof. Paul Gatenholm, Chalmers University of Technology

Prof. Claudio Migliaresi, Università degli Studi di Trento

Prof. Giacomo Moriconi, Università Politecnica delle Marche

Ad Alice

CONTENTS

1. Introduction

In the public opinion fuel cells are often associated with hydrogen and with the hydrogen economy. The feelings which arise from hydrogen fuel cells are often contradictory: from one side they are attracting many enthusiastic reactions since they are seen as possible clean energy conversion devices, from the other side they are looked at with skepticism.

One of the reasons for the negative impression fuel cells are originating to a part of the public, is that in recent years they have failed to respect the too optimistic promises of rapid commercialization which were made from some developers. Companies and governments invested large capitals, with limited returns. Moreover, two major points are often questioned by the skeptics: fuel cells are too expensive and the hydrogen economy will never become a reality. The cost issue is effectively a critical point, probably even more for low temperature fuel cells (such as the polymer electrolyte fuel cells). It must however be kept in mind that they are compared to other well established technologies which have more than hundred years of applications and developments. Among the different kind of fuel cells, the solid oxide based ones seem to be the most promising when cost is considered, since their high operative temperature allows the use of widely available non precious materials as catalysts. Therefore the material cost is no more the decisive factor. What must still be achieved is the knowledge and the experience needed for the application of inexpensive mass production technologies, such as those used for low cost electronic

packaging industry. There is no reason to believe that when first high volume and then mass production will take place, the cost will not be competitive. And this is in fact one of the reasons which is keeping investors in this field.

As far as the hydrogen economy is concerned, it seems to be actually too far to become a reality to justify the heavy medium-short term investments some companies are making. Until hydrogen from renewable sources is not available, it has to be produced from hydrocarbons. In such a case it is more efficient to produce electricity directly from the available fuels. However, the key point, which may render fuel cells (and in particular solid oxide fuel cells) widely applicable, is their multi-fuel operativeness (hydrogen, carbon monoxide, methane, etc.) and the possibility to utilize high temperature exhausts for cogeneration or hybrid applications. For instance methane can be in situ reformed to hydrogen and in some case even directly oxidized in the cell, with very high electrical conversion efficiency (more than 50%) even in residential micro-power plants (in the order of few kilowatts), and the waste thermal energy can be directly employed for heating or hot water production. In order to make fuel cells accepted by the public, the association hydrogen/fuel cells has not to be pushed too far. It remains however clear that the preferred fuel for any fuel cell is still hydrogen, and when the hydrogen economy will be a reality (if ever) it will greatly benefit from the developments in fuel cells science and technology.

The possibility to work on an emerging technology, which has the potential for decreasing the pollution related with energy production, is what first persuaded me to choose this topic for my PhD thesis. While getting closer to SOFC field I started to enjoy the complexity and multidisciplinary of this

field, which appears evident although the basic principle of operation of a fuel cell seems astonishing simple.

The worldwide research activity on SOFC is very active. A web search with the keyword SOFC in the topic field returned 935 articles published in international journals only in 2008 (source: ISI web of knowledge). Many aspects are currently under investigation; nevertheless it is generally agreed that the development of suitable low-cost fabrication technologies is presently the key technical challenge which needs to be faced. Two main SOFC designs are being studied by researches all over the world and are starting to open their ways towards commercialization, the planar configuration and the tubular one. Among the tubular cells, a general distinction is drawn between the traditional macro-tubular design (diameter > 15 mm) and the more recent micro-tubular one (diameter < 5 mm).

In the present thesis the two most promising geometries have been developed, *i.e.* the planar configuration and the microtubular one. Innovative aspects have been considered in both directions, as will appear evident in the following sections. The work on the planar cells was carried out in collaboration with the local company SOFCpower, which in particular dealt with the electrochemical characterization of the produced samples. The research activity on the fiber-like micro tubular design was carried out during a visiting period at the University of Colorado at Boulder (USA), in collaboration with Prof. Rishi Raj.

In both cases environmental impact and cost of the processing was minimized by using only water based ceramic powder production technologies.

a) Planar SOFC production

Planar anode supported cells (ASC) are constituted of stacked layers of different ceramic or metal ceramic composites each of them possessing different physical, chemical, mechanical and thermal properties. The fabrication of such devices typically requires the multi-step deposition and successive firing of the different layers. The cost of such high temperature treatments represents a significant fraction of the overall production expenses. In order to reduce the SOFC final costs, it is believed that scalable ceramic fabrication technologies, such as tape casting and co-sintering represent a very attractive production route.

A first aim of this work was to develop a processing technique capable of producing anode supported SOFC with thin electrolyte by sequential tape casting method (thus avoiding the lamination step) and co-sintering. In order to do this, different aspects associated with the processing steps, from colloidal suspension stability, to defects related with green forming and sintering had to be studied. One of the most critical factors in the co-sintering of ceramic multilayers is the stress generated because of different thermal expansion coefficients and sintering kinetics of the constituting layers. Such stresses, when not controlled, can lead to the formation of several types of defects, such as flaws, delaminations, retarded densification and warping. In order to understand and to solve the problems of defect formation and curvature development, a set up for monitoring in situ the sintering process has been built. The effect of different parameters (such as

green composition, type and amount of doping elements, powder granulometry etc.) on the sintering kinetics of the layers constituting the cells has been studied. The different sintering kinetics were related to the developed defects and curvature. Such analysis led to the fabrication of defect free cells which were successfully electrochemically characterised.
In order to being able to quantify the stresses which are developed and to predict the curvature behaviour of a bi-layer upon sintering, the knowledge of the very high temperature mechanical parameters of the materials is needed. A technique for measuring the uniaxial viscosity of thin tape cast layers upon sintering was therefore developed and is described in a section of this thesis.

b) Microtubular SOFC production

Whereas planar SOFC seem to be the preferred choice for future stationary application, micro tubular ones may be much more attractive for portable applications. The first advantage of the *micro tubular* SOFC design, is the potential very high volumetric power density, being it inversely proportional to the electrolyte diameter. The other advantages are resulting from low thermal mass: (i) high thermal shock resistance, and (ii) rapid turn on/off capability. However, miniaturization issues are arising when the diameter is decreased to less than 1 mm, mainly due to difficulties associated with the application of an internal current collector.
The novel approach, which is described in the present thesis, consists in fabricating the cell in the form of a fiber around a metallic wire. The problems related to the fabrication of such a device were faced and

eventually partially solved. The support for the cell fabrication consists of a thin nickel wire, on to which the porous anode layer, the electrode and the cathode, are deposited in succession. This nickel support acts as the current collector as well, and this opens totally new possibilities for downscaling tubular cells.

2. Theoretical background

2.1 Solid oxide fuel cells: state of the art

2.1.1 Types of fuel cells

Fuel cells are electrochemical energy conversion devices which directly transform the chemical energy of a fuel into electrical energy. The use of fuel cells for electrical power generation avoids the intermediate steps of producing heat and mechanical work typical of most conventional power generation methods. Therefore, fuel cells are not restricted by thermodynamic limitations of heat engines such as the Carnot efficiency. Moreover, because combustion is avoided, fuel cells produce power with minimal pollutant (1). Besides the high energy conversion efficiency and the environmental compatibility, fuel cells can have other advantages compared to traditional power generation system, the main being the size flexibility - they can be built in systems ranging from a few watts to megawatts, theoretically with the same efficiency- and the silent operation, since no moving part are involved in the energy conversion.

A variety of fuel cells have been developed. They are generally classified in terms of the type of electrolyte, which is also determining the operative conditions. The most studied are i) polymer electrolyte fuel cells (PEFC or PEM), ii) alkaline fuel cells (AFC), iii) phosphoric acid fuel cells (PAFC), iv) molten carbonate fuel cells (MCFC) and v) solid oxide fuel cells

(SOFC). The operating temperature and other characteristic features of such cells are summarized in Table 1.

Each of the above mentioned cells have different advantages and preferential application fields, depending upon the service temperature and the used fuel. One of the key advantages of SOFC, which is thought to make this technology more competitive in comparison to the other the fuel cells, is the multi-fuel capability. SOFC can in fact be operate with different fuels (*e.g.* hydrogen, carbon monoxide, methane, or even ammonia (2)), and are more tolerant to impurities compared to lower temperature cells. The ability to utilize high temperature exhausts for cogeneration or hybrid applications, represents another interesting feature (3), (4). The use of a solid and non corrosive electrolyte is another advantage compared to the other high temperature fuel cells (MCFC).

Table 1. Overview of the main fuel cell types and features.

	PEFC	**AFC**	**PAFC**	**MCFC**	**SOFC**
Electrolyte	Polymeric membrane	Potassium hydroxide	Phosphoric acid	Carbonate salt mixture	Ceramic
Catalyst	Platinum	Platinum	Platinum	Electrode material	Electrode material
Operating T (°C)	50 - 100	70 - 250	150 - 200	600 - 700	550 - 1000
Charge Carrier	H^+	OH^-	H^+	CO_3^{2-}	O^{2-}

The high operating temperature is from one side the reason for most of the intrinsic advantages (use of non expensive catalyst, high temperature exhaust, etc.), but, from the other side, it is the origin of some drawbacks. First of all, the materials involved in the core of a SOFC system have to be tolerant to high temperatures (say 700 – 800°C for a state of the art system). This is excluding all organic materials as well as the low temperature metal alloys. The material selection is therefore limited to ceramics or ceramic/metal composites and high temperature alloys. The thermal expansion coefficients of the materials composing the systems (in particular anode, electrolyte, cathode, sealing and interconnect), have to be carefully matched to guarantee the survival to the relevant temperature variation upon production and operation and the thermal cycles from room temperature to the operative point. Ceramics are fragile in nature, and this gives reason for one of the most critical drawbacks of SOFCs when used in a stack under real operative condition: they have low tolerance to stresses arising from thermal shocks, mechanical solicitations or RedOx cycles. Moreover, compressive sealings which require a high applied pressure cannot be used, thus further reducing the options for efficient sealing materials. The mechanical properties of the cells are dependent upon the fabrication process; the successful commercialization of such devices relies in advances in ceramic processing science.

A few recent books and review articles have covered the various aspects of fuel cells in general and SOFC in particular. Some of them are reported in the reference section (1), (3), (4), (5), (6), (7), (8), (9), (10). An extensive survey of the SOFC field is beyond the scope of this thesis; only a brief overview will be given here in order to better understand the choices and the results presented in the experimental section.

2.1.2 Solid oxide fuel cells basic principles

It has been previously stated (5) that solid oxide fuel cells are the most efficient devices yet invented for conversion of chemical fuels into electrical power. The first concept was reported and patented by Nernst at the end of the nineteenth century.

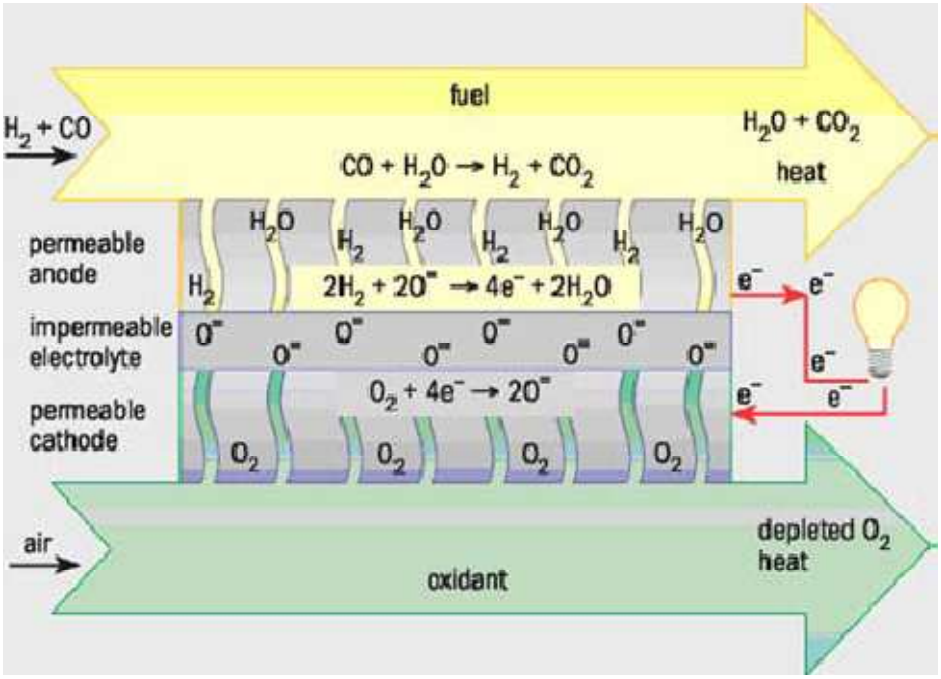

Fig. 1. Operating principle in solid oxide fuel cell, fuelled with a H_2/CO mixture. From Ref. (11).

Solid oxide fuel cells have a solid non-porous electrolyte, usually made by Y_2O_3-stablilized ZrO_2. The charge carrier through the electrolyte is the oxygen ion. The oxygen ion conductivity is determining the cell operating temperature, which is usually 550 – 1000°C, depending upon the electrolyte

materials and its thickness. Typically the anode is a Ni/ZrO_2 cermet and the cathode is a perowskyte, such as Sr-doped $LaMnO_3$ (12).

The basic principle of operation is reported in Fig. 1. Oxygen atoms are reduced into oxide ions on the porous cathode surface by electrons, and then flow through the ceramic electrolyte to the porous anode where the oxide ions react with the fuel, giving up electrons. The interconnect serves to conduct the electrons through an external circuit.

The half-cell reactions which occur at the anode and cathode are:

$$H_2 + O^{2-} \rightarrow H_2O + 2e^- \qquad \textit{Eq. 2-1}$$

$$\frac{1}{2}O_2 + 2e^- \rightarrow O^{2-} \qquad \textit{Eq. 2-2}$$

The performance of a fuel cell is measured as the voltage output at a given current flow. The current and the DC power output are usually normalized as current density and power density per unit surface of electrolyte, respectively.

At the equilibrium the cell voltage is given by the Nernst equation:

$$E = E^0 + \frac{RT}{2F} ln \left(\frac{P_{H_2} P_{O_2}^{1/2}}{P_{H_2O}} \right) \qquad \textit{Eq. 2-3}$$

where R is the perfect gas constant, F is the Farady constant, 2 is the number of electrons transferred in the half-cell reaction; the terms in the natural logarithmic are the partial pressures of the reactants and the product of the

reaction, respectively. E^0 is the standard potential difference between the two half cell reaction and is equal to:

$$E^0 = -\frac{\Delta G^0}{2F} = \frac{\Delta H^0 - T\Delta S^0}{2F} \qquad Eq.\ 2\text{-}4$$

with ΔG^0 the standard Gibbs free energy change of the hydrogen oxydation, ΔH^0 the standard enthalpy change and ΔS^0 the standard entropy change.

When the current is flowing, the measured potential is lower that the equilibrium potential, due to various losses (also called polarizations). The voltage can be expressed as:

$$E = E_{eq} - E_{leak} - \eta_{iR} - \eta_{act} - \eta_{conc} \qquad Eq.\ 2\text{-}5$$

The real voltage is therefore the ideal equilibrium voltage diminished by the losses due to electrolyte leakages E_{leak}, ohmic losses η_{iR}, activation η_{act} and concentration polarization η_{conc}. A typical i-V curve of a fuel cell is reported in Fig. 2.

The losses due to leakages in the electrolyte (for a material which is a pure ionic conductor) depend upon the electrolyte interconnected porosity and the absence of defects. In a SOFC both parameters are a direct consequence of the cell fabrication procedure and have to be minimized through a deep understanding and control of the processing conditions.

The ohmic polarization is the voltage loss due to ohmic resistance and is influenced by (i) the ionic conductivity of the electrolyte (depending upon thickness, material and temperature), (ii) the ionic and electronic

conductivity of the electrodes (depending upon materials, thicknesses and microstructure), and (iii) the contribution of the interfaces.

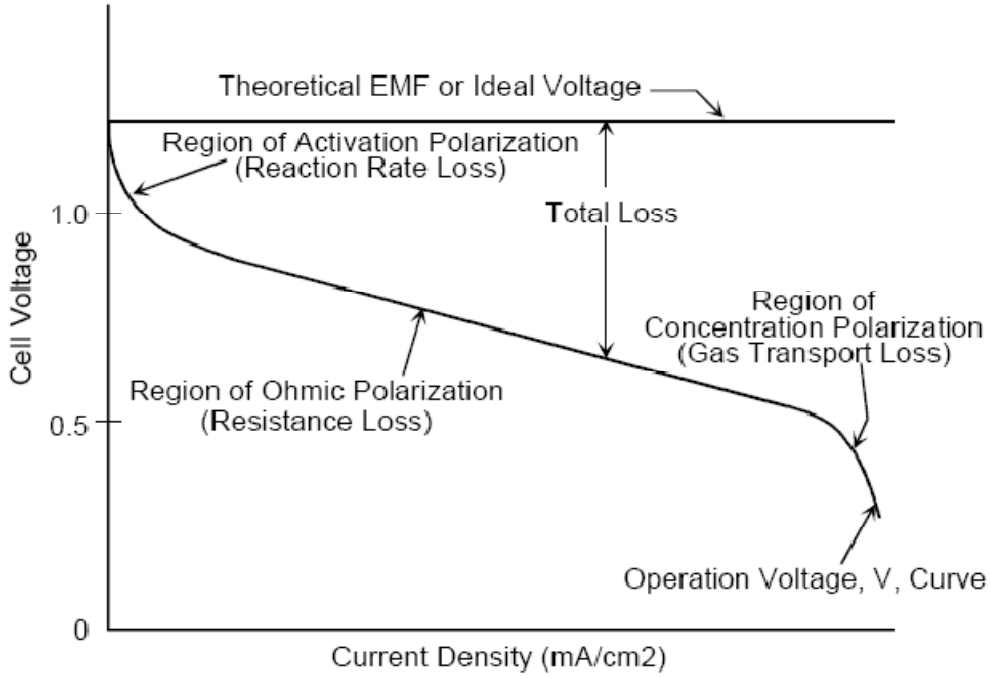

Fig. 2. Typical fuel cell i-V curve. (1)

The activation losses are associated with the rate of the charge transfer processes. For a fixed material composition, these decrease by increasing the points which are active for charge transfer. The charge transfer reactions are thought to occur within a limited distance from the electrolyte surface (in the order of 10 μm), where the three phases involved in the reaction meet: electrolyte / electrode catalyst / gas. Such zones are often referred as triple phase boundaries (TPB). One common way to reduce the activation losses consists in maximizing the TPB length, for instance through the creation of a finer electrode microstructure.

The concentration polarization is associated with the limits in the transport of gaseous species through the porous electrodes. For a well engineered cell, it is affecting the cell performances only at high fuel utilization (at high current densities). It is mainly influenced by the electrode porosity, pore size and pore distribution, and the electrode thickness.

2.1.3 Current research on SOFC

Generally speaking fuel cells have failed in the recent years in respecting the previsions done for their rapid commercialization (11), (13), (14). In the SOFC field in particular it is clear at this point of the history that various challenges have to still to be faced, despite some companies worldwide are already opening the ways towards SOFC commercialization.

The worldwide research in the field is focused in various directions: temperature reduction, degradation/long term stability, balance of plant, RedOx stability, mechanical properties and cost reduction.

Concerning the working temperature, efforts have been done in the past to reduce the operative condition from 1000°C to the actual 700-800°C (15), (16), and some research is being actually conducted in order to further reduce the operative conditions, by considering different electrolyte and electrode materials, such as ceria, lanthanum gallate or scandia-doped zirconia for increasing the electrolyte conductivity at lower temperatures (17), (18). Nevertheless, reducing the operative condition to lower temperature is not only an advantage, but may even be counterproductive for co-generation. The actual service temperature (700-800°C), already

allows the use of relatively inexpensive materials as interconnectors, such as ferritic stainless steel.

From the material side, yttria stabilized zirconia (YSZ) for the electrolyte and the Ni/YSZ cermet for the anode have been proven to provide sufficient performances with very low degradation rates even in the long term. Moreover, such materials possess good thermal expansion matching with the ferritic stainless steel used as interconnectors for intermediate temperature applications (3), (19), (20), (21). SOFC have been reaching a sufficient power output, which is ranging from 0.2 to 2 W/cm^2, depending upon materials, temperature, design, fuel, testing conditions etc. Any further increase in the specific power density is welcome, but the actual power densities are being judged sufficient for the commercialization of the technology, and there is no sign of a breakthrough in this direction.

SOFC science and technology is a widely multidisciplinary one in nature. It requires knowledge of chemistry, electrochemistry, material science, mechanical engineering, fuel processing, system engineering, manufacturing science and technology. The cell is only the core of the fuel cell power generator, the other components of the system being the SOFC stack (series of cells connected by an interconnector), the fuel reformation system (when not operated on pure hydrogen), the waste energy recovery system, the thermal management system, the process air supply system, control system, and power electronics and energy storage system. Whereas such technologies are already existing for other applications and could be inherited from SOFC, a significant and non trivial development has to be conducted in those areas in order to meet the requirements of a new technological application.

However, the main developments that may really help the SOFC technology to be widely applicable are the development of a reduction/oxidation tolerant anode (22), the increase of the mechanical reliability and the cost abatement. Both cost reduction and reliability can be achieved by developing a deeper knowledge in processing science and technology. As far as the cost is concerned, it is believed that cheap microelectronic fabrication techniques need to be adopted for ceramic fuel cells so that the cost can be decreased (6). It is generally agreed that, among other challenges, the development of suitable low cost materials and the low-cost fabrication of ceramic structures are presently the key technical challenges facing SOFCs (7).

2.1.4 SOFC materials

a) Electrolyte

The basic requirements for a material to be selected as a candidate for a SOFC electrolyte are: (5)

1. High ionic conductivity and low electronic conductivity;
2. Stability in reducing and oxidizing environment;
3. Ability to be processed as a thin gas tight film;
4. Acceptable cost and availability.

Up to now, yttria stabilized zirconia possessing the fluorite structure has been the preferred choice, and it seems that, despite the intense research

efforts towards alternative material, the next generation of SOFC will be based on such electrolyte. Figure 3 shows the specific conductivity as a function of reciprocal temperature for selected solid-oxide electrolytes. It is clear that 8YSZ is not the best ionic conductor at any temperature. As an example, $Bi_2V_{0.9}Cu_{0.1}O_5$ shows the highest conductivity, but is not stable in reducing atmosphere (23), (24). Such data can be used to determine the minimum operative temperature of a cell with a given electrolyte material, or the film thickness which is giving a sufficient conductivity. Steele and Heinzel (23) set a value of 0.15 Ω cm^2 as the target value for the area specific resistivity (ASR) of the electrolyte, to ensure that the total internal resistance of the SOFC is sufficiently small. They assumed that films of oxide electrolytes can be processed with cheap conventional ceramic technologies down to approximately 15 µm. Therefore, the specific conductivity of a 15 µm thick electrolyte must be at minimum 10^{-2} S cm^{-1}. A $Ce_{0.9}Gd_{0.1}O_{1.95}$ electrolyte reaches such conductivity already at 500°C, while a 15 µm thick $(ZrO_2)_{0.9}(Y_2O_3)_{0.1}$ electrolyte needs at least 700°C for working effectively. A 150 µm self supporting $(ZrO_2)_{0.9}(Y_2O_3)_{0.1}$ electrolyte would need 1000°C for having an acceptable conductivity. The electrolyte material and its thickness are thus decisive in choosing the correct working temperature, which in turn is also influencing the choice for the interconnector material. While high temperature cells (around 1000°C) necessitate of expansive ceramic interconnectors (such as $La(Ca)CrO_3$), the interconnector for intermediate temperature cells (650°C – 750°C) can be ferritic stainless steel.

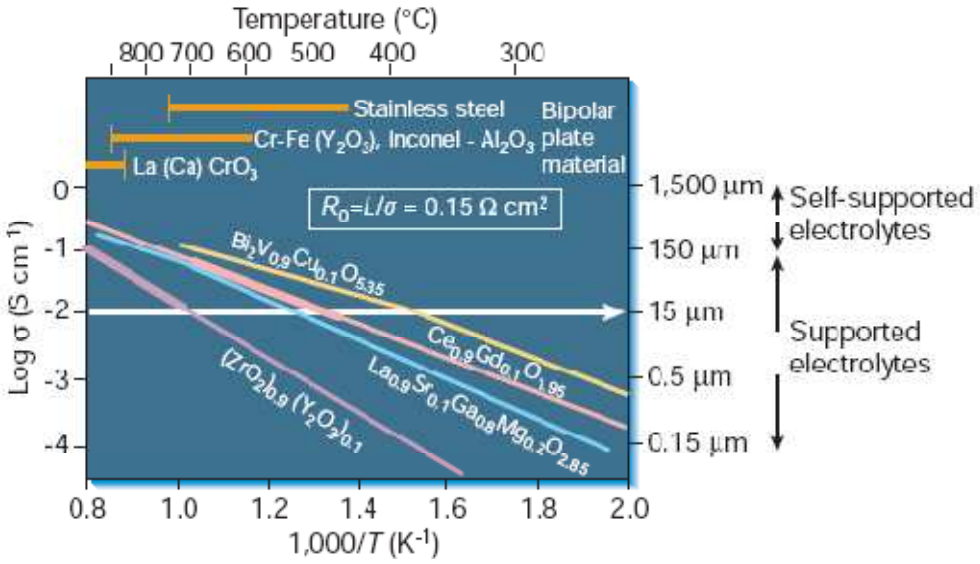

Fig. 3. Specific conductivity as a function of reciprocal temperature for selected solid-oxide electrolytes. (23)

Alternative electrolyte materials can be divided into two major structures: the fluorite structure (face centered cubic cations with anions occupying all the tetrahedral sites) or the perowskyte structure.

The most studied oxide possessing the fluorite structure is the M_xO_y stabilized cubic zirconium oxide (Sc^{3+} is the most effective dopant among Ca^{2+}, Y^{3+}, Sm^{3+}, whereas Mg^{2+} is the least efficient in providing an open pathway for conduction) (25). Pure zirconia exists in three different structure. At room temperature it is monoclinic. At 1170°C the monoclinic – tetragonal phase transformation takes place. The cubic fluorite structure is stable above 2370°C. The cubic structure of zirconia can be stabilized at lower temperature by the addition of aliovalent cations (*e. g.* Y or Ca). The other well studied system is the Cerium oxide.

Oxide ion conduction is governed by defects, specifically oxygen ion vacancies and interstitial oxide ions. In the case of pure CeO_2 or ZrO_2, the ionic conductivity is low because the concentration of defects is low. To maintain charge neutrality, the addition of an aliovalent ion is compensated by an increase in the concentration of a ionic defect. As a consequence the conductivity is increased (5). The conductivity of doped zirconia or ceria with a given element shows a maximum at a certain concentration. Figure 4 shows the conductivity of the ZrO_2-M_2O_3 system with some selected metals.

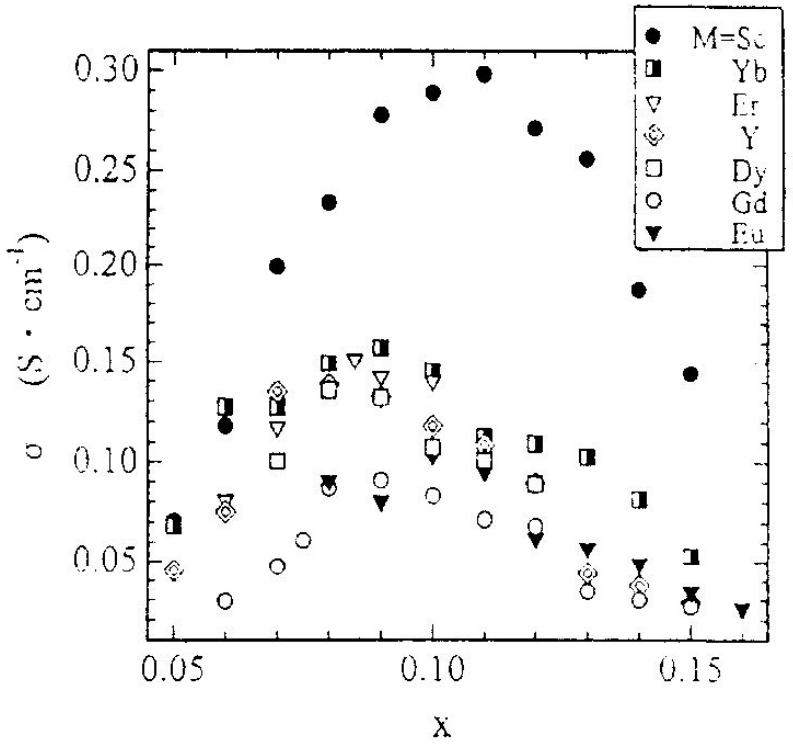

Fig. 4. Electrical conductivity at 1000°C of cubic zirconia with different dopants. (26)

The most employed doping element for zirconia is yttrium, although YSZ is not the most conductive doped zirconia. Scandia stabilized zirconia (SSZ) is an attractive electrolyte for intermediate temperature SOFC though it has been observed to degrade upon long term exposure at high temperatures (1000h at 1000°C). However the main limitation in the use of SSZ at lower temperature is the high cost of scandia (5). Long term degradation at high temperature has been observed with zirconia doped with other elements as well (Yb_2O_3 or 3mol% Y_2O_3).

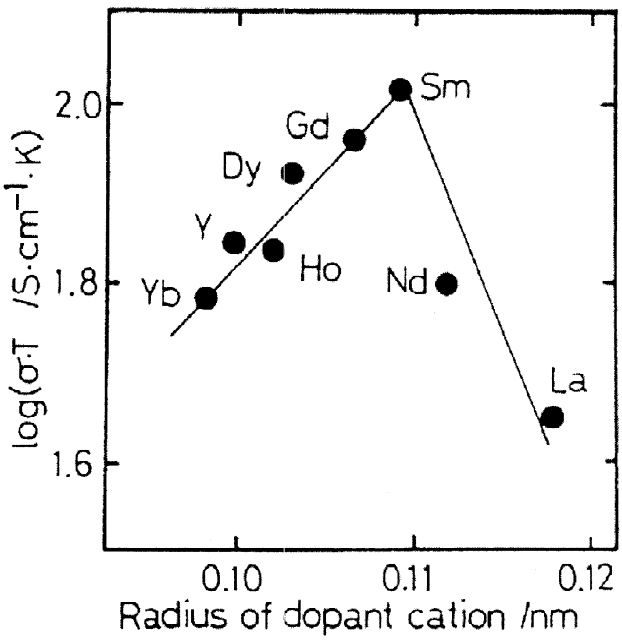

Fig. 5. Ionic conductivity of $(CeO_2)_{0.8}(LnO_{1.5})_{0.2}$ at 800°C on the radius of dopant cation (27).

The other candidate as oxygen ion conductor for SOFC (especially for low temperature applications) is doped ceria (27), which shares the same fluorite

structure of YSZ. The conductivity depends upon the type and amount of doping element. The conductivity of ceria at 800°C doped with different lanthanides is given in Fig. 5. Gadolinium or samarium doped ceria show high ionic conductivity already at 500°C, and have been extensively studied for low temperature SOFC. However, one of the disadvantages of ceria-based ion conductors is their low stability in reducing atmosphere. While such materials are purely ion conductors at high oxygen partial pressures, at lower partial pressures they become partially reduced, leading to an increase in the electronic conduction. One way to overcome the electronic conduction issue is to protect the ceria electrolyte with a thin YSZ coating on the anode side.

Oxides with perovskyte structure based on the formula ABO_3 have been studied as alternative electrolyte materials. $LaGaO_3$ doped with Ca, Sr or Mg, $LaAlO_3$, $La_{1-x}Al_xO_3$, $LaScO_3$, $CaTiO_3$. $La_{0.8}Sr_{0.2}Ga_{0.85}Mg_{0.15}O_3$ (LSGM) appear to be promising candidate for low temperature SOFC operating at 450°C. Also oxides with other structures such as brownmillerites (*e.g.* $Ba_2In_2O_6$), or hexagonal apatites like $La_{10}Si_6O_{27}$ or $Nd_{10}Si_6O_{27}$, have been considered as alternative electrolyte materials, as well as proton conducting oxides (5).

Despite the extensive research on electrolytes, zirconia based compositions are still the best for intermediate temperature SOFC, due to their good stability in both oxidizing and reducing environment, low electronic conductivity and acceptable cost and ionic conductivity. The optimal YSZ thickness at 800°C is 10 µm. At temperature around 700°C, SSZ could be preferred to YSZ, but, as already said, the cost of scandia represents a critical issue. Ceria based electrolytes or perovskites such as $LaGaO_3$ doped with Sr or Mg are interesting option for very low temperature cells (below

550°C). The main disadvantages associated with the non-zirconia based electrolytes are the electronic conductivity and the chemical stability (5).

b) Anode

The anode is the electrode where the fuel is oxidized. Its main role is to provide sites for fuel oxidation, and to facilitate the charge neutralization by electronic conduction. In anode supported cells it is acting as the cell mechanical support. The main requirements for a SOFC anode are (5), (28):

1. Electrical conduction;
2. High electrocatalytic activity;
3. Porous but mechanical resistance;
4. Thermal expansion coefficient close to neighboring components;
5. Low cost, especially when used as a mechanical support;
6. Stability at high temperatures in reducing atmosphere and to RedOx cycles;
7. Capability to avoid coke deposition and, tolerance to sulfur in fuels.

The anode material has to be produced with an interconnected porosity which is retained during the fabrication of the fuel cell and its operation, without limiting the mechanical properties. An intimate contact between anode and electrolyte is essential. In order to extend the triple phase boundaries into a volumetric region within the anode, and not limiting them to the contact area between anode and electrolyte, the anode has to be both

electronically and ionically conductive. Two ways have been followed to reach this goal: (i) the use of a porous composite of a metal catalyst and oxide ion conductor, such as the traditional Ni-YSZ cermet, or (ii) the use of a single-phase electrode with mixed conductivity, providing both oxide ion and electron mobility.

The Ni-YSZ cermet is the most employed anode for SOFC. The first patent regarding such cermet was published in 1970 (28), (29). The mixing of nickel with the electrolyte material has at least three benefits: (i) it reduces the thermal expansion coefficient mismatch between anode and electrolyte, (ii) it reduces the nickel aggregation during fabrication and service and (iii) it increases the depth of the triple phase boundary region into the anode.

Ni-YSZ anodes can be fabricated by conventional ceramic powder technologies (tape casting, tape calendering, slip casting or screen printing) starting either from NiO powders, or from Ni powders and mixing them with YSZ. The anode production with NiO powders is usually the preferred route for at least two reasons: first, it is probably cheaper, because sintering can occur in air and, second, it is easier to get fine oxide powders with a controlled granulometry with respect to pure Ni powder. When the anode is produced by NiO powders, the oxide is reduced in situ the first time the cell operates. Upon reduction from NiO to Ni, a volume reduction of approximately 25% is obtained, and the anode porosity is increased.

A minimum Ni proportion in the cermet is necessary for continuity of electronic conduction (also called the percolation threshold), whereas the zirconia particles may be non-continuous. This value depends on the anode microstructure, porosity, particle distribution and orientation. A value of about 30 vol% Ni has been reported to be the lower limit. An increase of the Ni amount much above 40 vol% does not produce significant benefits (30),

(31), (32), (33). The conductivity of the cermet for a given Ni content can change of order of magnitudes, depending upon the processing route. Figures 6 and 7 report the measured electrical conductivity at 1000°C of Ni/YSZ cermets produced with different processing routes as a function of nickel content.

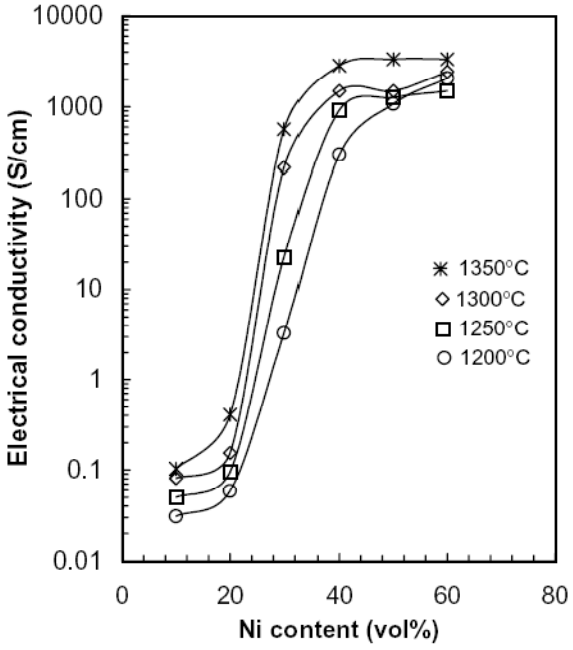

Fig. 6. Variation of electrical conductivity at 1000°C as a function of nickel concentration of Ni/YSZ cermet fired at different temperatures. (32).

Ni-YSZ cermets are good current collectors and possess high catalytic activity. The Ni content is > 30 vol% (usually 40-50%), and the porosity range is about 20-40%. The basic properties of the nickel–zirconia cermets have been widely studied and they are actually the best anode materials for intermediate temperature cells working with hydrogen; for these materials

the requirement is to optimize their properties through the control of microstructure and minor additives.

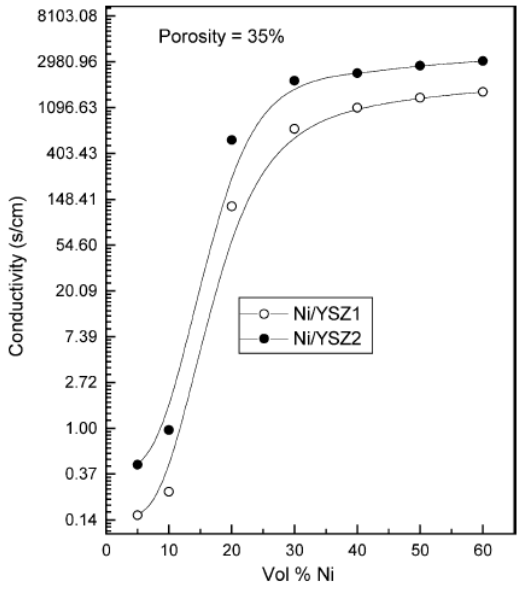

Fig. 7. Electrical conductivity of Ni/YSZ cermet at 1000°C as a function of nickel content. YSZ powder has different size: YSZ1 (d_{50} = 0.40 µm), YSZ2 (d_{50} = 0.85 µm). *(33).*

One of the major disadvantage of the nickel-cermet electrode is that impurities in the fuel, particularly sulphur containing odorants (which are added in the natural gas for security reasons), are poisoning the Ni based anode. The other major limitation arises from the rapid deposition of carbon in the direct oxidation of methane or higher molecular weight hydrocarbons. When natural gas has to be used as fuel, it needs to be externally or internally reformed with steam. Alternative materials have been studied in order to prevent hydrocarbon cracking under dry conditions. Interest has focused on ceria replacing zirconia and copper replacing or partially

substituting nickel. Copper has been added to nickel to reduce its catalytic activity for hydrocarbon cracking (28). Precious element addition such as Au (34) or Ag (35) also increase the carbon tolerance to the Ni surface. However, although anodes based on different materials that allow for the operation of SOFCs directly on hydrocarbons have been developed, the performance of such anodes are still lower than the state-of-the-art SOFCs with Ni/YSZ anodes operating with hydrogen (28).

c) Cathode

The cathode/electrolyte interface is the place where the oxygen is reduced to O^{2-}. The basic requirements for a cathode are therefore: (36), (37):

1. High electronic and ionic conductivity;
2. High electrocatalytic activity for the cathode oxygen reduction;
3. Chemical stability in oxidizing atmosphere;
4. Similar expansion coefficient and good adherence to the solid electrolyte;
5. Porous structure that permits rapid mass transport of reactants and product gases;
6. Low cost.

In a well designed anode supported SOFC, it is generally recognized that the overall losses of the cell are generally dominated by the polarization losses for the O_2 reduction on the cathode (38). The choice of the cathode material

and the engineering of its microstructure are therefore decisive for the fuel cell electrical performances.

Because of the high operating temperature, only noble metals or electronic conducting oxide can be used as cathode materials. The firsts are unsuitable for commercial applications because of their high cost and insufficient long term stability. In addition, they would annihilate one of the main advantages of SOFC towards lower temperature fuel cells, which is the possibility to work without any precious catalyst. The choice of the cathode material depends on the chosen electrolyte material, the desired operating temperature, the cell design, and the specific ceramic fabrication methods (39).

Perovskite-type lanthanum strontium manganite, $LaSrMnO_3$ (LSM) and lanthanum calcium manganite, $LaCaMnO_3$ (LCM) possess acceptable thermal expansion coefficient in comparison with zirconia electrolytes and good performances at operating temperatures of 800°C and above. A recent review article (12) is resuming the developments in lanthanum strontium manganite perovskite cathodes materials for SOFC. For applications requiring lower temperature operation (600–800°C), other perovskite-structured ceramic electrode materials have been considered. These include: (39)

- Lanthanum strontium ferrite (LSF), $(LaSr)(Fe)O_3$
- Lanthanum strontium cobaltite (LSC), $(LaSr)CoO_3$
- Lanthanum strontium cobaltite ferrite (LSCF), $(LaSr)(CoFe)O_3$
- Lanthanum strontium manganite ferrite (LSMF), $(LaSr)(MnFe)O_3$
- Samarium strontium cobaltite (SSC), $(SmSr)CoO_3$
- Lanthanum calcium cobaltite ferrite (LCCF), $(LaCa)(CoFe)O_3$

- Praseodymium strontium manganite (PSM), $(PrSr)MnO_3$
- Praseodymium strontium manganite ferrite (PSMF), $(PrSr)(MnFe)O_3$

In order to increase the performances by increasing the triple phase boundaries, the conductive perovskite material is often mixed with a ionic conductor, such as YSZ, SDC or GDC, thus creating a composite cathode. The incorporation of the electrolyte material into the cathode has been shown to improve the electrode performance at lower temperatures by increasing the volume of active sites available for electrochemical reactions (37).

2.1.5 Basic SOFC designs

Two basic SOFC designs have been studied since the 1960s: the planar and the tubular design, each one existing in a number of variations. For instance, the planar SOFC has been developed in circular or rectangular shape, with internal holes for gas feeding, or with external manifolds. Examples of typical planar stack configuration are reported in Fig. 8.

The tubular SOFC may be of a large diameter (> 15 mm), or of much smaller diameter (< 5 mm) or even < 1 mm, in the so-called microtubular design. The macro-tubular design was originally developed by the Westinghouse Electric Corporation. The tubes may be flat and joined together to give higher power density with easily printable surfaces for depositing the electrode layers. Fig. 9 illustrates the Siemens-Westinghouse tubular design.

The biggest developers of the tubular design in USA are (40) the Siemens Westinghouse Power Corporation (cathode supported 1.8 m tubes with an outer diameter of 22 mm or flattened tubes design) and Acumentrics (anode supported 45 cm long tubes with an outer diameter of 15 mm). In Japan there are Kyocera (flattened tubes design), TOTO (0.5 m tubes with an outer diameter of 16 mm), and Mitsubishi Heavy Industries.

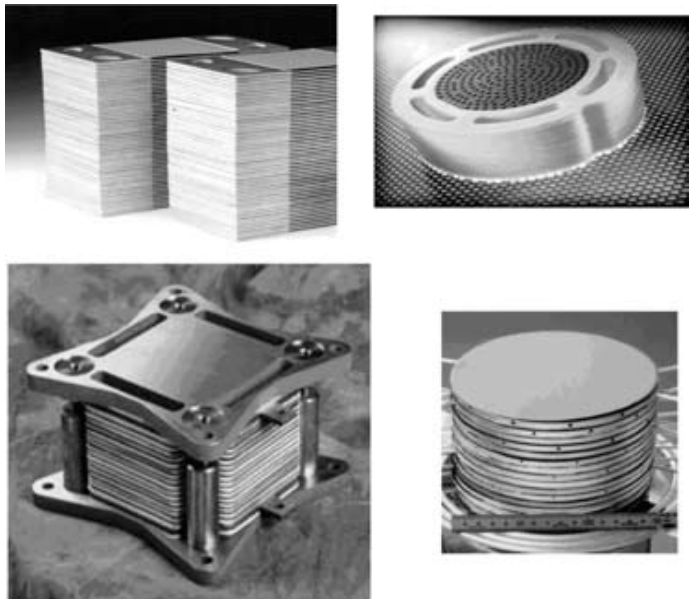

Fig. 8. Illustration of different planar stack assemblies. (11).

The major industrial developers of the planar design are Mitsubishi Heavy Industries and Tokyo Gas (Japan), Ceramic Fuel Cells Ltd. (Australia), Haldor Topsoe (Denmark), H.C. Starck (The Netherlands), Ceres Power and Rolls Royce (UK), VTT (Finland), BMW, HC Stark and Webasto (Germany), Sulzer (Switzerland), HTCeramix/SOFCpower (Italy), SOFCo, Delphi Automotive Systems, GE, ZTek (USA) and Global Thermoelectric (Canada).

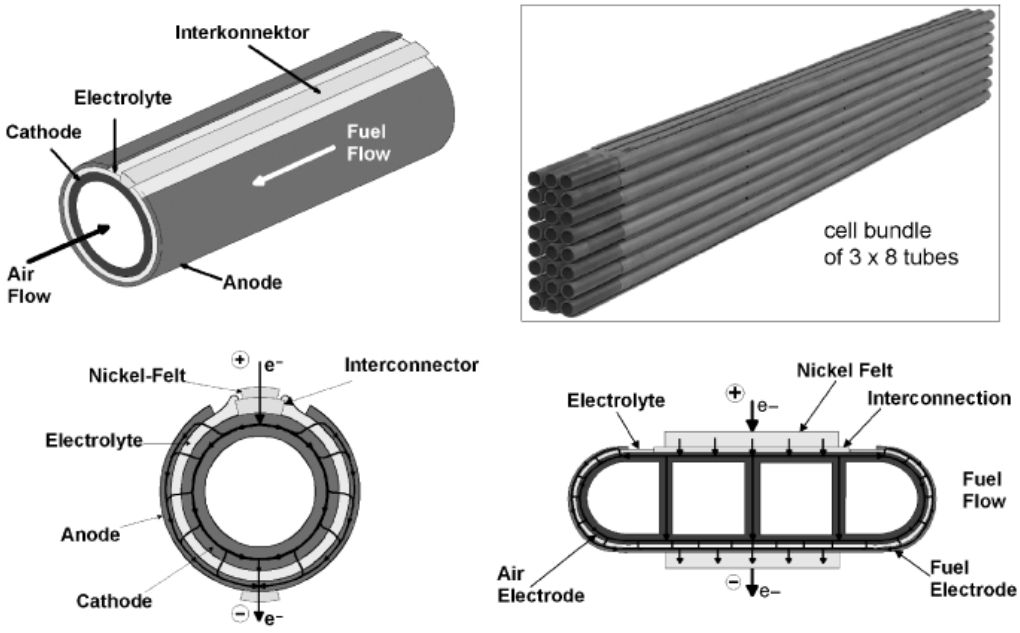

Fig. 9. Siemens Westinghouse Power Corporation—tube design, cell bundle and flattened tube. (40)

In 2005 a total number of 1500 employee was estimated to work in the SOFC field worldwide (40), but this number is rapidly increasing. Many private and public research institutes and universities are involved in basic and applied research as well.

In the basic planar design, a single fuel cell is assembled into a stack in order to increase the power output. An interconnect is separating the cells in the stack. This interconnect has the function of gas separator, gas diffusion layer and electrical contact between the anode and cathode of the cells (1). The three basic configuration and their features are summarized in Fig. 10.

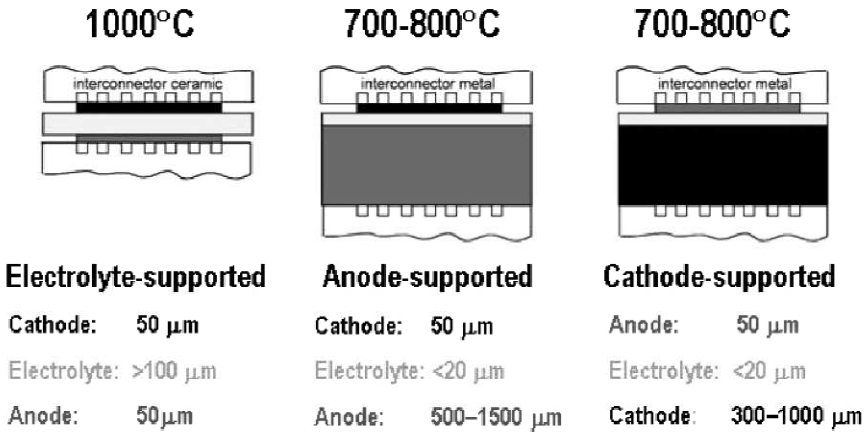

Fig. 10. Basic configuration of planar SOFC and their temperature range. (6).

The first developed planar cell was the electrolyte supported cell. The high thickness of the electrolyte makes it hardly conductive at low temperatures. Such cell, when based on YSZ electrolytes, requires high operating temperature, in the range of 1000°C. Such very high temperature put stringent limits to the stack components, in particular to the interconnect, which can not be ferritic stainless steel. Efforts have been done in the recent years to reduce the electrolyte thickness to around 10 μm, in order to make the electrolyte sufficiently conductive at 700-800°C. Such low thickness makes the electrolyte not mechanically resistant and the cell has to be supported either by the anode or by the cathode. Although many advantages are associated with the electrode supported SOFC, some drawbacks are arising from the fact that more stringent requirements are set to the electrode, being it the element providing mechanical integrity to the cell. In particular in Ni-YSZ anode supported cells the possible oxidation of the Ni phase leads to a volume increase and to stresses which can cause the failure

of the whole cell. In electrolyte supported cell this issue is less problematic, being the anode thickness much lower.

Alternative metallic supports based on stainless steel have been considered in the last years and look very promising, but still they need further research and development (41), (42), (43).

In planar cell stacks, a sealing has to be used to isolate air from fuel. The seal needs to have a thermal expansion coefficient matching the other fuel cell components, must be an electrical insulator, must be thermochemically stable under the operational conditions of the stack, stable under both the high temperature oxidizing and reducing operational conditions, should be able to withstand thermal cycling between the cell operation temperature and room temperature and have obviously a competitive cost (11). A variety of different sealing approaches have been developed: rigid seals (*e.g.* glass-ceramics, brazes, metallic seals), compliant seals (*e.g.* viscous glasses) and compressive seals (*e.g.* mica-based composites). Due to the enormous technological importance of sealing for SOFC, most of the development is carried out by private companies and the results are often jealously conserved as industrial secrets. Unfortunately this is slowing down the worldwide development and the launch of SOFC technology on the real market.

Engineering a proper sealing with high long-term stability is a real challenge for SOFC developers. One of the main advantages of tubular cell bundles in the Westinghouse design is that the air and the fuel are naturally isolated because the tubes are closed at one end. Therefore they do not require any high temperature seals to isolate oxygen from fuel. This has made the performance of the tubular cell stack very stable over long periods of times. Stacks based on such technology delivering hundreds of kilowatts for

several years without any significant degradation have been successfully demonstrated (44), (45). However, their surface power density is much lower (about 0.2 W/cm^2) compared to planar cells (up to 2 W/cm^2 for single cells and 0.5 W/cm2 for stacks) (11). The manufacturing costs are also higher, and this issue is limiting the commercialization of high diameter tubular cells. The volumetric power density is lower for macro-tubular cells than for planar cells.

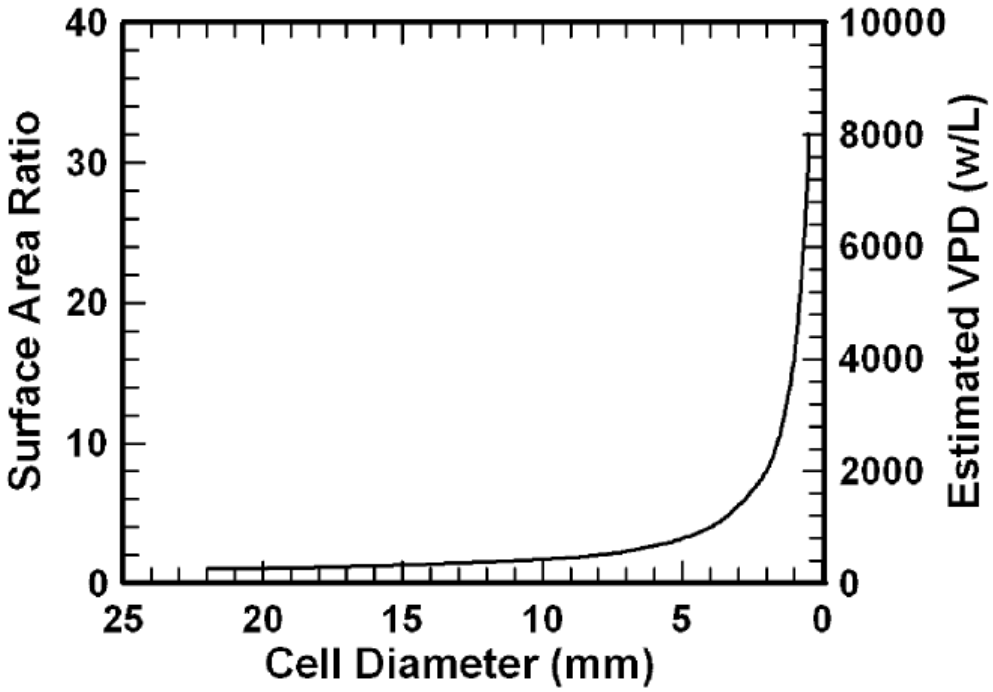

Fig. 11. Electrolyte ‘‘surface area ratio’’ and corresponding estimated volumetric power density (VPD) in ideal stack as a function of single-cell diameter (46).

On the other hand, in tubular SOFC, the electrolyte surface area to volume ratio can be enhanced by decreasing the single cell diameter. Under the

hypothesis of square configuration of the single-cells arrangement in a stack, one can estimate an electrolyte surface area of 0.1 m^2/l. If the tube diameter is reduced to 2 mm, the surface area becomes 0.8 m^2/l. Under the hypothesis of a constant surface-specific power density of 0.250 W/cm^2, a stack containing 2 mm diameter tubes will produce 2000 W/l power (Fig. 11) (46). Theoretically, the volumetric power density scales with the inverse of the cell diameter. Such calculation are however only hypothetical, since as the cells gets smaller, it is more difficult to built a stack with the same cell packing and other issues become important (*e.g.* gas diffusion issues in small tubes, wirings and current collections etc.), and it is not granted whether the area specific power density can be unchanged.

2.1.6 SOFC production methods

Thick films as support electrodes in the planar configuration can be fabricated by well known advanced ceramic fabrication methods (e.g. tape casting, screen printing, tape calendaring). However, one of the most challenging aspects in SOFC fabrication is the production of a thin and really gas tight ceramic film for the electrolyte in anode supported cells. There are a number of technologies, which allow the deposition of thin polycrystalline oxide films, though not all of them are suitable for all the SOFC configurations or materials or are economically viable.

Such techniques can be grouped in chemical deposition techniques, physical methods and ceramic powder processing methods. An extensive review of such methods applied to SOFC electrolyte fabrication is given in Ref. (16). Chemical deposition techniques are divided into chemical vapour deposition

techniques and liquid precursor route methods (sol-gel and spray pyrolysis). Only the firsts will be briefly discussed here due to their higher use in SOFC production.

There are two main chemical vapour deposition techniques: Chemical Vapour Deposition (CVD) and Electrochemical Vapour Deposition (EVD). CVD is a chemical process in which one or more gaseous precursors form a solid material by means of an activation process (16). The most used precursors for YSZ film fabrication are $ZrCl_4$ and YCl_3. The growth rates of the CVD film are in the range of 1–10 µm/h, depending on the evaporation rate and substrate.

Westinghouse Electric in 1977 developed an electrochemical vapour deposition (EVD) technique to fabricate gas-tight thin layers of doped zirconia on macro-tubular cells supported on cathode. This EVD process involves growing a dense oxide layer on a porous substrate at elevated temperatures and reduced pressures (5). EVD is a modified CVD process and consists in a two-step process. The first involves the pore closure by a normal CVD reaction between the reactant metal chloride and oxygen or water vapour. The film growth proceeds due to an electrical potential gradient across the deposited film (16). Growth rates are faster than in the CVD process, being in the order of of 3–52 µm/h.

Physical methods which have been employed for electrolyte fabrication are thermal spray, laser deposition techniques, and physical vapour deposition (PVD) (16). Thermal spray in its variants - flame spraying (FS), air plasma spraying (APS), low-pressure plasma spraying (LPPS), detonation flame spraying (DFS), electric arc spraying (EAS), and high-velocity oxyfuel (HVOF) spraying-, are more suitable for producing thick (in the order of hundred of µm) porous structures. The density of the deposited films has to

be further increased by a subsequent high temperature thermal treatment. SOFC supported on metal substrates produced entirely by vacuum plasma spray (VPS) techniques, with a 25 μm thick electrolyte has been reported (47), and more recently by atmospheric plasma spray with < 40 μm electrolyte layers (48).

Physical vapour deposition (PVD) is a generic term for a variety of sputtering techniques (16). Radio frequency (RF) sputtering has been widely used for thin films depositions, although its deposition rates are very low (0.25 μm/h). Reactive magnetron sputtering allows a deposition rate one order of magnitude higher (0.25 μm/h). Thin films may also be deposited by vacuum evaporation using an electron beam heating device with much higher deposition rates (around 60 μm/h).

Ceramic powder processing methods can also be employed for the production of thin electrolyte films, although they have been usually employed for the fabrication of thicker films. The most suitable seem to be screen printing, slurry coating, tape casting, slip casting, tape calendering, and electrophoretic deposition. Ceramic powder processing in general and tape casting in particular will be described in the following section. A few reports are exists on anode supported cells with thin zirconia electrolyte fabricated entirely via tape casting. In most of them solvent-base tape casting followed by lamination is employed (49). Fabrication of doped zirconia tapes by water-base tape casting with water soluble binders (PEG – PVA) is reported for thick films (50) or thin films (51), or with acrylic/styrene emulsion binders (52). Most of them involve the production of separate layers for the electrolyte and the electrodes, which are joined in a second step by applying pressures at relative high temperature. Typical parameters for this process (usually referred as lamination or warm

pressing) are temperature, ranging from 50 to 110°C, and pressure, varying from 20 to 200 MPa, depending upon the amount and the properties (mainly the T_g) of the polymers chosen as temporary binders (53), (54), (55), (56).

The main advantages of most of chemical and physical methods is that the deposited films do not have to be subjected to sintering step to reach the final density. As a consequence, dense films can be obtained even on non-shrinking substrates. Films produced by powder processing methods needs to be sintered to reach the desired density and shrinkage is usually associated with this process. When a film is sintered on a rigid constraining substrate, incompatibility stresses are arising, which are hindering the densification and may cause the coating to crack. The topic of co-sintering and constrained sintering will be threaded in detail in a separate section and were considered in detail in this thesis. On the other hand, the high cost of the chemical or physical processes and often the low quality (in terms of the residual porosity and thus gas tightness) of the deposited layer are the drawbacks which make such process less competitive towards ceramic powder processing routes.

Only in year 2000 (16), it was thought that CVD/EVD and spray pyrolysis would have become the key technologies for depositing thin electrolyte layers, while tape casting, and screen-printing were considered cost-effective and promising, but not applicable for large area cells (larger area than 100 cm^2). It was thought that the large shrinkage associated with the removal of polymeric binders and plasticizers in subsequent sintering steps would have reduced the quality of the cell, and that difficulties would have arisen in retaining adequate porosity within the supporting electrode structures during the co-firing stage for densification of the electrolytes. In 2005 it was recognized that some of the cited technologies were not as

promising as others when commercialization is considered. For example, electrochemical vapor deposition (EVD), magnitron sputtering (PVD), RF sputtering (PVD), sol–gel, transfer printing, and roll calendaring required either further development or were not viable (4). Nowadays it is generally believed that in order to develop a successful SOFC technology, the production costs have to be kept as low as possible, and the above mentioned process can not guarantee prices low enough for the final product.

In this thesis, only ceramic powder processing routes were followed. Thanks to the developments in the powder processing science and to the better understanding of co-sintering issues, large area cells (up to 200 x 150 cm^2) were successfully produced entirely by tape casting (anode and electrolyte) and screen printing (cathode).

2.2 Colloidal processing of ceramics for SOFC

Among all the fabrication methods for solid oxide fuel cells, it is generally recognized that colloidal processing is the most economical route for producing ceramics with good thermal and mechanical properties (57), (58). In this thesis special care was always addressed to the economical feasibility of the developed devices, and only powder based technologies were chosen as fabrication methods.

A number of books and reviews have covered the production of ceramics by colloidal processing, from suspension stabilization, to green forming and sintering (58), (59), (60), (61), (62). Special attention will be addresses here only to the tape casting technology and the problems associated with co-sintering of multilayers.

2.2.1 Powder consolidation by tape casting

Tape casting is considered a highly productive process allowing the fabrication of thin (from 5 μm) or relatively thick (over 1 mm) and flat ceramic substrates and multilayer structures mainly for the electronic industry. Tape casting belongs to the wet powder processing techniques for green forming (the main others being slip casting, filter pressing, gel casting, electrophoretic deposition). The basic principle of the process is amazingly simple and is outlined in Fig. 12. It involves the preparation of a slurry of the ceramic powder in a dispersing fluid, with addition of a whole

range of ceramic additives, the main being a dispersant, a binder and sometimes a plasticizer (63), (64). This slurry is then spread over a stationary or moving flat surface using a blade with a fixed gap also referred as *doctor-blade*. The wet cast tape enters then the drying chamber where the solvent is evaporated by means of heat end air circulation, and a flexible and strong tape is formed. This tape is then peeled off from the substrate, cut in the desired shape, de-bound and sintered. In the industrial practice the use of a moving polymeric carrier (such as PET, PE, PP) is generally preferred in a continuous process, due to the higher process productivity, while in the lab scale the slip is often cast on a fixed surface (e. g. a glass or metal plate with a moving doctor blade). The carrier is usually covered with a release agent in order to facilitate the peeling of the dried tape.

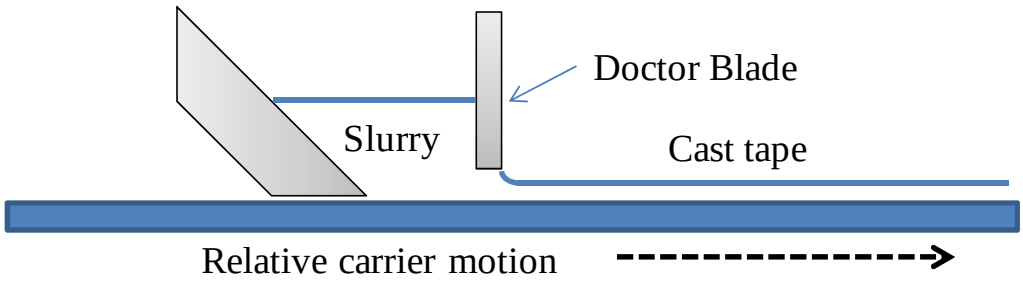

Fig. 12. Basic principle of tape casting process.

Most of the challenges and the know-how necessary to develop a reliable tape casting process lay in the creation of a suitable formulation to be cast.
The usual liquid carrier is usually non-aqueous, although recently water-base suspensions are attracting more and more interest. The most common solvents are ethanol, methanol, toluene, methyl ethyl ketone, and xylenes.

(64); sometimes a combination of two or more solvents is employed. The slurry is prepared by mixing the components by ball milling or ultra-sonicating. In this process, the soft agglomerates are broken down and the dispersant covers the powder surface and keeps them dispersed. The dispersant can work by electrostatic repulsion, steric hindrance or a combination of both (Fig. 13). Some of the most commonly reported dispersant are linoleic acid, stearic acid, menhaden fish oil, salt of polyacrilic or methacrylic acids, sodium silicate, polyethylene glycol, as well as pH adjustments and a whole range of proprietary chemicals (64). The most commonly employed ways to optimize the dispersant content for a given powder/solvent system are sedimentation tests (64) or viscosity analysis.

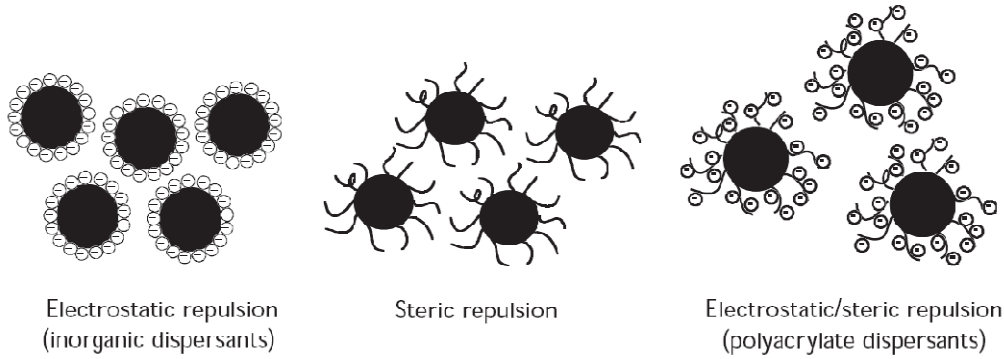

Fig. 13. Schematic illustration of the mechanism of powder dispersion for different kind of dispersants. (65).

The binder is an organic polymer which gives flexibility and strength to the green state. Once the tape is dried, the binder should become a continuous matrix entrapping and binding the ceramic particles. Usually a plasticizer is added to modify its mechanical properties and allow the relaxation of the drying stresses. Some of the most commonly employed binders are: vinyl

binders (PVA, PVB), acrylic (PEMA, PMMA, acrylic emulsions), polyolefin and cellulose based (64). The binder is added usually after the first stage of the milling process, because the high impact force of the milling media can degrade its polymeric chains, and because it is more effective when it covers well dispersed particles rather than agglomerated particles.

A variety of other additives are sometimes added to the slips to get the desired properties. They include antifoaming agents, rheology modifiers, surfactants, and others. The thickness of the dry layer results from a combination of several parameters. In general the tape thickness increases by increasing the blade gap, the slurry level in the reservoir, the solid loading of the suspension, while it decreases by increasing the casting speed and the slurry viscosity. Some equation have been proposed to relate the final tape thickness to such parameters (59). Nevertheless the determination of the tape thickness a priori by the means of such equations is often unsuccessful and perhaps not even useful. In the practice the correlation between the dry thickness and the processing parameters (mainly blade gap and casting speed) is derived empirically for each slip system. The dry tape thickness lays often in a range between one third to two thirds of the blade gap. In order to get constant thickness, it is preferred if the slurry shows a pseudoplastic behaviour. Moreover, for sake of reproducibility, the slip viscosity should be fairly constant in the neighborhood of the working shear rate. The shear rate as a function of the casting speed and the blade gap is given in Fig. 14 (66). A high casting speed is usually helpful in getting more reproducible results, since at high shear rates the slip viscosity is less variable. Unfortunately a higher casting speed is not always applicable, especially for thick films with long drying times, since the permanence in

the drying chamber will be reduced and the tape could exit wet from the drying chamber.

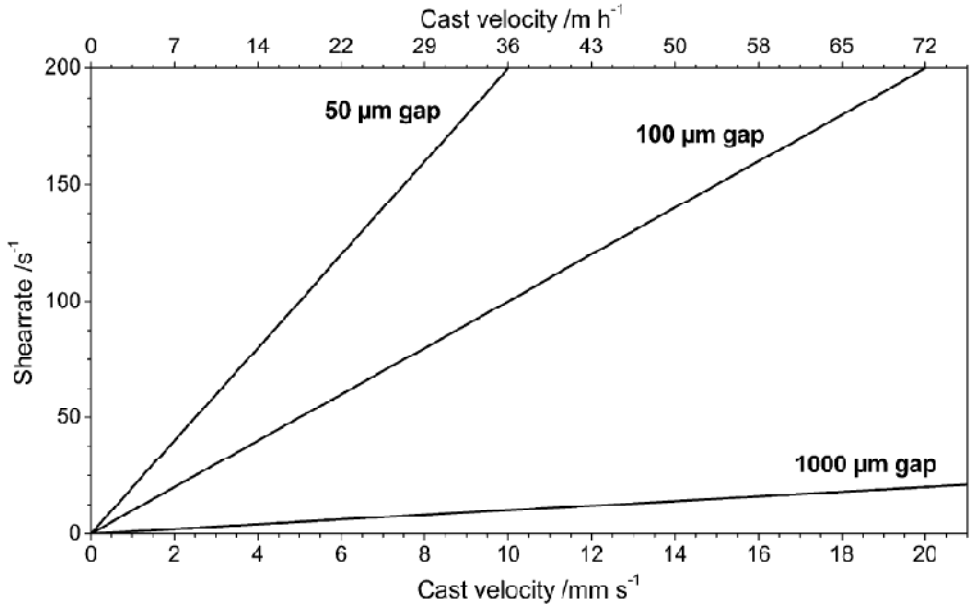

Fig. 14. Dependency of cast velocity, blade height and shear rate. (66).

Typical defects which can affect the dried tape quality are large voids caused by air bubbles entrapment or by rapid evaporation, which can be reduced by controlling the de-airing condition, selecting a proper anti-foaming agent, or controlling the drying conditions. Other defects are the presence of agglomerates or impurities. Agglomerates can be reduced by improving the milling and the filtering conditions or optimizing the dispersant concentration, while impurities have to be reduced by controlling the casting environment. For some applications (*e.g*. thin tape for electronics or for SOFC electrolytes) the casting process is conducted in a clean room.

Any punctual defect is detrimental for the mechanical resistance of the sintered product. In drying stage, cracks due to the stresses induced by the drying of the solvent can nucleate from those points (Fig. 1). Punctual defects have to be controlled, but cannot be totally eliminated. The drying stress defects can be eliminated by selecting a binder and plasticizer system which is able to relax the stresses and by tailoring their concentration.

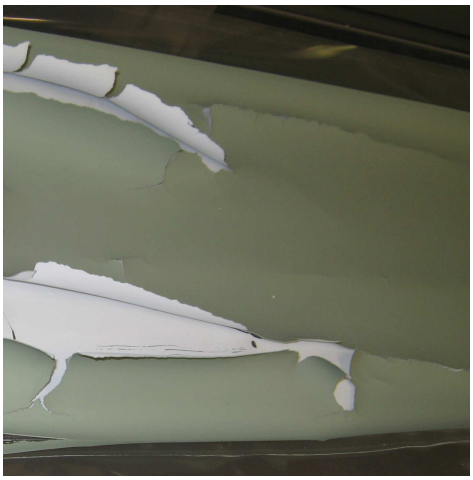

Fig. 15. Typical drying cracks observed an anode/electrolyte tape in the preliminary experiments performed in this work.

Segregation of particles with different sizes and densities can be a problem for thick tapes. It can be reduced by increasing the colloidal stability of the slurry, the viscosity or the Bingham yield stress. Segregation of binder to the surface of the tape has to be avoided as well, since it can induce differential green densities. As a result the tape can bend or crack during sintering. The flow under the doctor blade can produce alignment in elongated particles, producing anisotropy during sintering. Whereas this effect can be sometimes used to produce aligned structures, (e.g. for

orienting silicon nitride whiskers in a silicon nitride slurry (67), or in a mullite matrix (68)), it has to be avoided in most of the applications.

2.2.2 Water based compared to solvent based approach

In this work, when it was considered feasible, water based processes were developed, being them preferred to organic solvent based technologies, for the lower environmental impact and the lower cost compared to organic solvents, in terms of purchasing, handling, recycling, disposing and protecting the working environment. Development of water based processes (e.g. tape casting) is more challenging, and sometimes these have been considered not feasible. The complications of using water as solvent derive from the fact that water can alter the stability of the suspensions, since it may dissolve (leach) ions out of the ceramic powder, dissociate into acidic and basic species (OH^- and H^+). For instance, it was found that aqueous suspensions of $La_{0.6}Sr_{0.4}CoO_3$ were not stable over time, because Sr ions leached from LSCO powder affecting flow properties of the slurry, reducing the zeta potential of the powders and leading to agglomeration (69). Another challenging aspect is that water has higher surface tension compared to the most traditional solvents for tape casting (ethanol, methyl ethyl ketone, acetone or toluene)(64).

Nevertheless the enormous potential advantages in terms of cost, safety and environmental compatibility that derive from water based process compared to organic solvent based process, fully justify the more intensive effort which has to be put in research and development.

Two of the challenges which arise from the high surface tension of water are the high drying stresses for thick films and the dewetting phenomena, which are more critical in thin films.

The drying stresses have been shown to be proportional to the surface tension of the liquid phase and inversely proportional to the powder size (70). For thick films produced by water based dispersion of sub-micron sized powders, the drying stresses can be very high. Cracks due to drying were in fact observed in the preliminary experiments performed in the present work. The drying cracks were successfully avoided with the appropriate amount of binder with T_g lower than room temperature (which can relax the internal stresses) and the elimination of possible defects which act as crack initiators (agglomerates, air bubbles, impurities such as dust, etc.).

The high surface tension of water can be a problem in casting thin film (below 10 µm dry thickness) and spreading it uniformly on the carrier support (e.g. silicone coated PET), due to wettability issues. This problem can be sometimes solved by increasing the viscosity of the slurry, by introducing a surface tension modifier or by choosing the appropriate carrier. The choice of the appropriate carrier is not always trivial and a balance between its wettability with the water-base slurry and the "release grade" (a standard measure of the force which is needed to peel off a tape from a standardized carrier area) has to be taken into account. For research purposes some more prosaic issues play a major role in the carrier choice, such as the lack of availability of the suitable carrier in low quantities (minimum orders for tape casting carrier suppliers is usually a few tons).

It is sometimes questioned whether water-based slips are of industrial interest for tape casting process, since it is thought that the drying associated

with the higher boiling point of water makes the process less productive. However, against the common beliefs, it has been recognized that, (64) the freedom offered by water emulsion binder (such as those mostly employed in this work) to dry quickly in the first stage is a great benefit, which can result in shorter drying times than even organic tapes can provide, depending upon specific slip system and tape thickness.

2.2.3 De-binding and sintering

After the consolidation step, a firing operation is required. Green compacts have to be thermal treated to consolidate and produce the desired microstructure. Upon heating, the green ceramic shrinks, reducing the porosity and increasing the mechanical properties. The first stage of the thermal treatment is usually the de-binding step. The organic binder is eliminated by slowly heating the green piece (generally up to 400 - 600°C). The second step is the sintering of the ceramic powder. A number of books are covering the complex aspects of powder sintering (59), (60), (61). In the following section it is given just a brief overview of the sintering process, without the intention of being exhaustive, and of the special issue of constrained sintering of multilayers.

a) Driving force

For the occurrence of sintering the free energy of the system must decrease. The driving forces for sintering have been traditionally indentified as: (60)

1. Curvature of the particle surface;
2. Externally applied pressure;
3. Chemical reaction.

In absence of chemical reactions and of external pressure, the decrease in surface free energy E_s of a system composed of particles with radius *a*, molar volume V_m and specific surface energy γ_{sv}, is given by: (60)

$$E_s = \frac{3\gamma_{sv}V_m}{a} \qquad Eq.\ 2\text{-}6$$

The decrease in surface energy is therefore inversely proportional to the particle radius. If γ_{sv} = 1 J/m^2, a = 1 µm and V_m = 25 x 10^{-6}, E_s is equal to 75 J/mol of material. If the particle radius is 0.1 µm, then the decrease in surface energy becomes 750 J/mol of material.

b) Matter transport

The driving force for sintering gives a motivation for sintering, but the actual occurrence of sintering requires matter transport. In crystalline solids matter transport is a diffusive process which involves atoms, ions or molecules (60). The presence of defects in the crystal lattice allows the mass transport to take place. Traditionally three classes of defects are identified in the crystal lattice: (i) point defects (vacancies, interstitial atoms, substitutional atoms), (ii) line defects (dislocations) and (iii) planar defects

(free surfaces, grain boundaries, stacking faults, crystallographic shear planes). The point defect concentration (which governs the rate of matter transport through the crystal lattice) can be controlled by varying three variables: temperature, oxygen partial pressure (in oxide systems) and dopants concentration. Solutes (or dopants) have a significant influence on sintering, also in very small concentrations. However, the control of the sintering kinetics by the manipulation of the defect concentration is not always simple and applicable in real systems, especially when more elements are present and more mechanism operate during sintering. Other factors, such as particle packing, green homogeneity, particle size, have a major influence on sintering, and may overcome the effects produced by changing the defect concentration.

c) Mechanism of sintering

Sintering of crystalline materials occurs by diffusion of matter along different paths which define the mechanism of sintering. The matter is transported from region of higher chemical potential to region of lower chemical potential (60).

Six mechanisms of solid state sintering for polycrystalline materials have been identified (Fig. 16). They are:

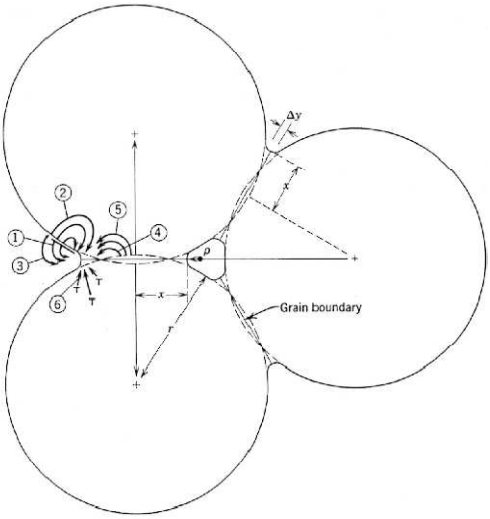

Fig. 16. Mechanisms of transport in solid state sintering. (71).

1. Surface diffusion
2. Lattice diffusion (from the surface)
3. Vapour transport (from surface)
4. Grain boundary diffusion (from the grain boundary)
5. Lattice diffusion (from the grain boundary)
6. Plastic flow (from dislocations)

All mechanisms are responsible for neck growth between the particles and strength increase during sintering. However, only the last three lead to shrinkage and densification. They are usually referred as densifying mechanisms (volume mechanism), while the first three are called non-densifying mechanism (surface mechanism). For ceramic polycrystals only grain boundary and lattice diffusion are governing the shrinkage of the powder compacts.

2.2.4 Constrained sintering

a) Elastic-Viscous Analogy

Sintering can be seen as the response of a green body to the sintering pressure. The sintering pressure can range from a hundred kPa in glasses or glass ceramic materials (72), from a few hundred kPa to a few MPa for submicron polycrystalline oxides like Al_2O_3 or TiO_2 (73), (74), up to 100 MPa for nanocrystalline oxides such as ZrO_2 (75), (76). When a region of a ceramic body is shrinking at a different rate with respect to nearby regions (as it is the case of a rigid inclusion in a matrix, region of agglomerated powders, green ceramic multilayer or coating on a rigid substrate), transient stresses are generated. Viscous flow will try to relieve such stresses. A calculation of the stresses requires a time-dependent viscoelastic model. The response of the material to an applied stress consists on an almost instantaneous elastic strain and a time dependent strain due to the viscous flow. The stresses associated with sintering are usually very low, and the resulting elastic strain is much smaller than the strain observed during sintering. Since the observed deformation results virtually only from viscous flow, it is possible to consider only the viscous response (60). For those reasons Bordia and Sherer (77), (78), (79), (80), suggested that a constitutive equation based on linear viscous deformation would be more appropriate, and experimental measurements support those conclusions (73), (81).

For an isotropic linear viscous material, the elastic-viscous analogy can be applied. This approach consists in solving the equations for the elastic case and replacing the Young's modulus E with the uniaxial viscosity η, the Poisson ratio ν with the viscous Poisson ratio ν_p and the strain ε with the strain rate dε/dt (82).

The Newton's law for the principal stresses (σ_1, σ_2, σ_3) and principal strain rates ($d\varepsilon_1/dt$, $d\varepsilon_2/dt$, $d\varepsilon_3/dt$), can be written as:

$$\dot{\varepsilon}_1 = \dot{\varepsilon}_{f1} + \frac{1}{\eta}[\sigma_1 - \nu_p(\sigma_2 + \sigma_3)] \qquad \textit{Eq. 2-7}$$

$$\dot{\varepsilon}_2 = \dot{\varepsilon}_{f2} + \frac{1}{\eta}[\sigma_2 - \nu_p(\sigma_1 + \sigma_3)] \qquad \textit{Eq. 2-8}$$

$$\dot{\varepsilon}_3 = \dot{\varepsilon}_{f3} + \frac{1}{\eta}[\sigma_3 - \nu_p(\sigma_1 + \sigma_2)] \qquad \textit{Eq. 2-9}$$

These equations are the analogous to Hooke's law for isotropic, linear viscous materials. The subscript f refers to the free sintering case. Therefore $d\varepsilon_f/dt$ is the strain rate that would be observed in case of unconstrained sintering ($\sigma_1 = \sigma_2 = \sigma_3 = 0$). In the special case of $\sigma_2 = \sigma_2 = 0$, one obtains:

$$\dot{\varepsilon}_1 = \dot{\varepsilon}_{f1} + \frac{1}{\eta}\sigma_1 \qquad \textit{Eq. 2-10}$$

Most of the techniques available for measuring the sintering viscosity rely on Eq. 2-10.

b) Viscous parameters measurement

Viscous parameters can be measured on bulk specimens or derived from theoretical models. Nevertheless, the theoretical prediction of the viscosity and Poisson's ratio of a material during sintering has always posed serious challenges to the ceramic scientists, and most of the developed models predict different dependency of the viscosity on the relative densities, as well as negative viscous Poisson ratio, in contradiction with the experimental data (78), (79). Also the experimental determination of such parameters is not an easy task and poses both theoretical and experimental challenges. The mechanical parameters for sintering are obtained by measuring strain rates at a fixed applied stress. For a specific material they vary with density, grain size and temperature. Various technique exist for measuring the mechanical parameters upon sintering. An excellent review can be found in Ref. (73).

One of the first experimental technique which was successfully employed is sinter forging. In this technique a compressive uniaxial load is applied to a specimen and the strain rate is measured. Equipment with high accuracy are nowadays available (*e. g.* 2 µm for a cylinder of 20 mm height and 12 mm diameter) (83). In order to obtain reliable data with a minimum effect on microstructure, uniaxial load should be applied long enough to get a signal above the background noise, but short enough to avoid anisotropy in the microstructure (84), (85). The stress amplitude is in the range of the sintering stresses (73). Since hot forging can induce microstructural

anisotropy, other techniques have been developed: cyclic loading dialtometry (82), (86), (87), (88), and discontinuous hot forging (72), (89), (90). The first allows the determination of many data points, since it is using only short loading cycles to reduce anisotropy; the latter uses the application of a load until unacceptable anisotropy is developed, thus obtaining only few but robust values for single specimen. Two or three load application may be feasible during one sintering run (73). A more recent approach suggested the use of bending creep test and video-imaging to measure the viscosity of porous materials during sintering (91), (92).

c) Special cases in constrained sintering

Once the mechanical constants are known, the geometry of the sintering structure which is undergoing differential densification must be taken into account. Four special cases are of utmost importance in powder science and technology and have been addressed in the literature: (i) composite materials where porous matrix densifies around rigid inclusions (or an agglomerate which densifies at a different rate), (ii) thin film densifying on a rigid substrate, (iii) multilayered structures where different materials shrink with different rates and (iv) green body with density variation (73). Such special cases are illustrated in Fig. 17.

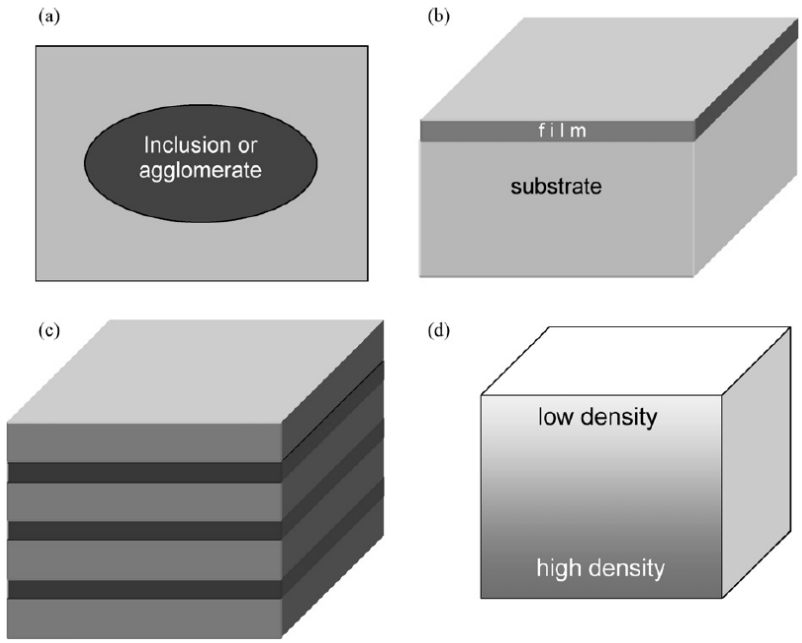

Fig. 17. Schematic illustrations of structures that undergo differential densification: (a) Composite materials where porous matrix densifies around rigid inclusions or agglomerate, (b) thin film densifying on non-densifying substrate, (c) layered structures of two or more types of materials that densify at different rates (d) porous material with density gradient (73).

Due to its great importance in SOFC manufacturing and performances, only the layered structures case will be discussed in the following description and has been faced in the present work.

d) Co-firing of multilayers

Many technologies use thin or thick layers of dissimilar materials in order to achieve functional requirements (93). In most of the cases the ceramic layers

are produced from powder processing technologies (e. g. tape casting, screen printing, spray coating, etc.), lamination and sintering. Conventionally, a multilayer ceramic membrane can be obtained by multiple repetition of the coating and heat treatment procedure. However the co-sintering technique has attracted much attention, due to its reduced cost. Some of the most important application of the co-sintering technique include: electronic packaging such as low temperature co-fired ceramics (LTCC), (94), (95), multilayer ceramic capacitors (MLCC), piezoelectric actuators (96), microfiltration membranes (97), coatings used for either thermal protection (TBC) (98), (99), or for abrasion, oxidation and corrosion resistance, as well as SOFC (100), (101).

The most straightforward and successful analysis which are found in the literature dealing with the stresses arising upon co-sintering of joint structures, are based on the solution of the elastic equations and the application of the elastic viscous analogy. The stress solutions in the case of layered structures derive from the fact that the integral of the stresses and bending moments along the thickness direction should be equal to zero. For a symmetric laminate consisting in alternating layers of two sintering materials, it was shown that the biaxial stress arising in the layers is:

$$\sigma_1 = \frac{1}{1+mn}\eta_1^{'}\Delta\varepsilon \qquad \textit{Eq. 2-11}$$

$m = t_1/t_2$ being the layer thickness ratio, with t_1 and t_2 layers thickness, $n = \eta_1(1-\nu_2)/[\eta_2(1-\nu_1)]$ the viscosity ratio, with η the uniaxial viscosity and ν the viscous Poisson's ratio. It can be seen that if layer 1 is shrinking faster than layer 2, it will be subjected to a biaxial tension, while layer 2 will be in

biaxial compression. It has been shown that even by considering the visco-elastic solution, the stresses generated are the same of a purely viscous solution, after a small transient increase in stress (102).

If a laminate is asymmetric, the structure can bend as a response to the stresses which arise upon sintering. The layer which is densifying faster will be in tension, but the stresses will be partially relaxed by bending the structure. The simple case of an alumina/zirconia bi-layer was first examined in references (81) and (82). The normalized curvature rate $\dot{k}$ is given by:

$$\dot{k} = \frac{t_1+t_2}{r} = \frac{6(m+1)^2 mn}{m^4n^2 + 2mn(2m^2+3m+2)+1}\,\Delta\dot{\varepsilon} \qquad \textit{Eq. 2-12}$$

where r is the radius of curvature. Therefore, the curvature rate has the same sign of the strain rate difference, *i.e.* the layer, which tends to shrink faster, tends to curve the bi-layer towards its side. The maximum tensile stress in the fastest shrinking layer is given by:

$$\sigma^{max} = \frac{m^2 n(4m+3)+1}{m^4n^2 + 2mn(2m^2+3m+2)+1}\,\eta\Delta\dot{\varepsilon} \qquad \textit{Eq. 2-13}$$

Conversely, the maximum tensile developed on the outer surface of the slower shrinking layer is:

$$\sigma^{max} = \frac{m^4 n - m(3m+2)}{m^4 n^2 + 2mn(2m^2+3m+2)+1}\,\eta\Delta\dot{\varepsilon} \qquad \textit{Eq. 2-14}$$

This interpretation of constrained sintering of multi-layers includes the evolution of sintering viscosity during densification and grain growth as well as the evolution of sintering stress and it is interaction with compatibility stresses from the different layers. One of the mayor limitation of this approach is that it is based on the assumption that the compatibility stresses are not affecting the density, grain growth, sintering stress and viscosity of the sintering layers. In the reality, if a stress is applied continuously to a sintering material (as is the case of a sintering multilayer, where compatibility stresses are acting), it develops an anisotropic microstructure. The resulting sintering potential and viscosity can therefore be affected. Nevertheless, if the stress is very low or is applied for a short time, this effect can be neglected. Despite the model limitation and approximations, calculation which were carried out following such approach were found to predict very well the trends in the sintering mismatch stresses and in bi-layer curvature (82). In the present work the same assumption have been often made.

3. Experimental procedure and results

3.1 General experimental methods

In this paragraph we report the experimental procedure that were used for all the following analyses. Each of the following sections will have its own “materials and methods section”, which will address in detail the specific materials and used procedure.

3.1.1 Tape casting procedure

Water based slurries were prepared by adding the ceramic powders to a solution of deionized water and ammonium polyacrylate dispersant (Darvan 821A, R.T. Vanderbilt Inc., USA), mixed overnight with yttria stabilized zirconia balls, filtered to 100 µm and de-aired by a low vacuum Venturi pump. A mixture of two commercial acrylic emulsion binders was then added (Duramax B-1014, Tg = 19°C and Duramax B-1000, Tg = -26°C, Rohm and Haas, France) and the suspension was slowly stirred for 2 h. Ratio between high to low Tg binder was tailored in preliminary experiments in order to obtain the desired green strength and flexibility necessary for handling and cutting the green cast tapes.

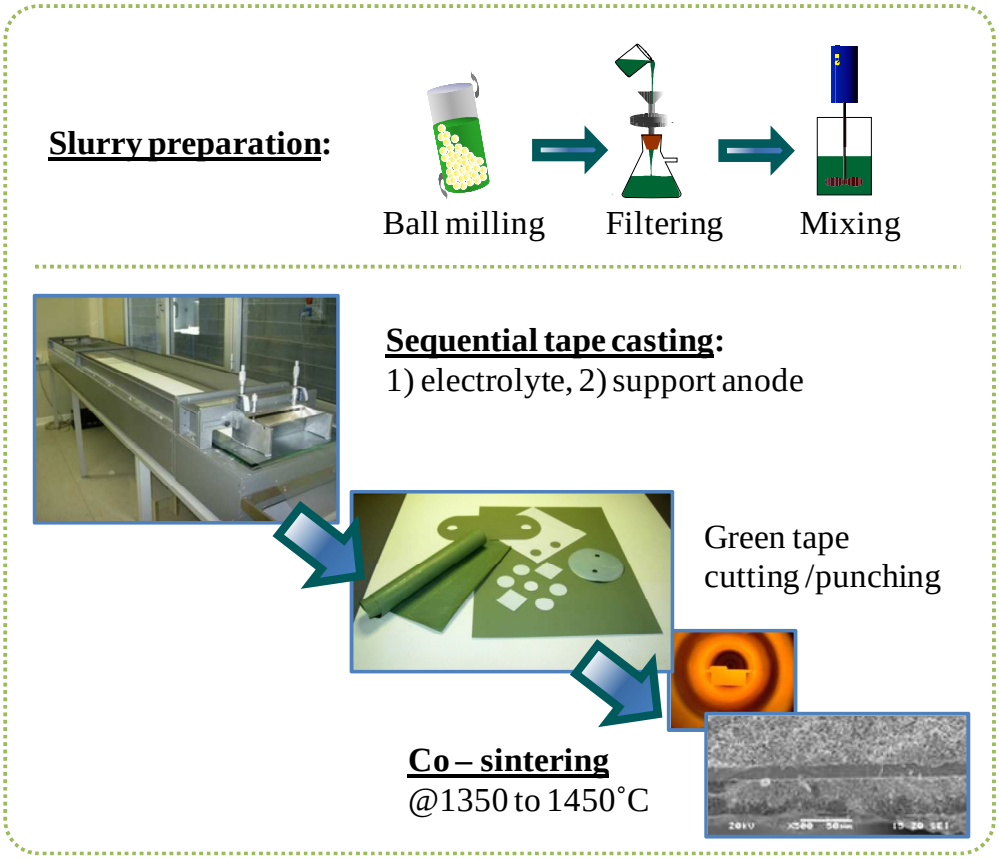

Fig. 18. Schematic process flowchart for the planar half-cells produced in this work.

The slips were cast on a silicone coated PET film by a laboratory scale tape caster, with a double blade apparatus (Richard E. Mistler, Inc., USA). Thanks to the low water solubility of acrylic binders, it was possible to cast one suspension on top of the previous dried one without layer mixing, thus achieving at the same time a good interfacial joining. Anode supported half cells were therefore obtained by first casting a thin electrolyte (usually from 8 to 20 µm dry thickness) and then the anode (from 200 to 500 µm) on the

top of the dried electrolyte tape. Electrolyte and anode suspensions were also cast alone to produce samples useful for sintering shrinkage determination. Because of the difficulties in handling a 10 µm thick electrolyte green tape, the blade gap was adjusted to obtain a standalone 100 µm thick green tape. The green bi-layers were cut in rectangular bars for the curvature observation, or in the desired shape for the electrochemical tests (usually 3 cm^2). An overview of the process for half-cell production is given in Fig. 18.

3.1.2 Thermal treatment

a) Thermal de-binding

The first thermo-gravimetric analysis (TG, STA 409, Netzsch GmbH, DE), was performed on tape cast samples with a heating rate of 1°C/min up to 700°C. The weight loss and the weight loss rate of a sample with organic loading of 13 wt% is shown in Fig. 19. The whole weight loss occurs below 400°C, with a peak in weight loss rate at 315°C. Following this result, a de-binding ramp of 1°C/min to 550°C or 600°C was chosen. The de-binding step is one of the critical steps in the firing process, since stresses are developing in the ceramic compact as the organic polymers are burning out, and a slow heating ramp is generally advised. When the de-binding step is out of control, the stresses may lead to green cracking and to warping.

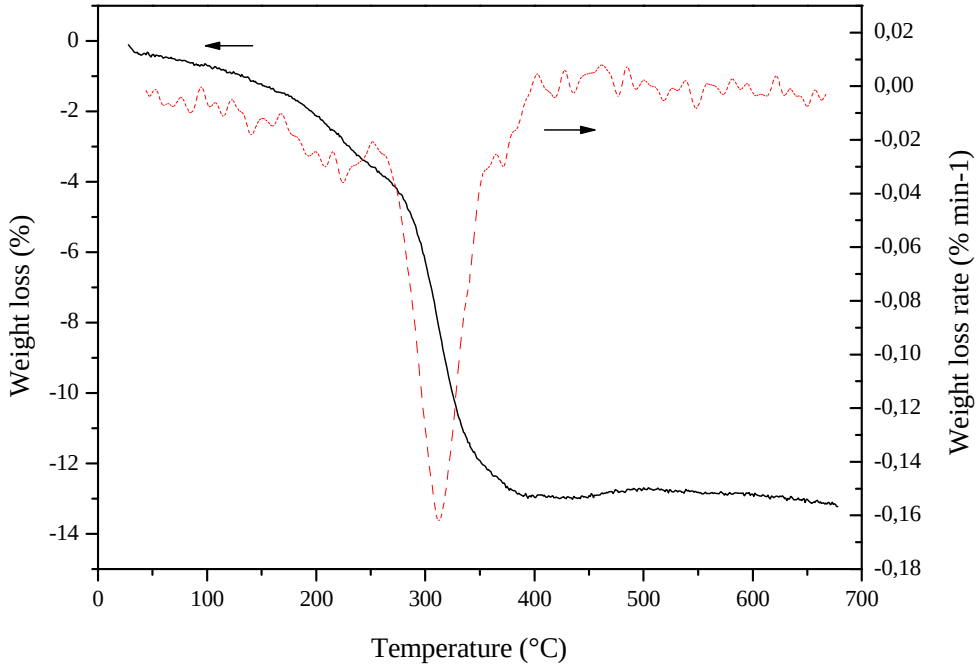

Fig. 19. Thermo-gravimetric analysis of a tape cast sample containing 13 wt% organics.

b) Sintering: curvature and shrinkage determination

Sintering experiments were conducted both with push-rod dilatometer (DIL 402E, Netzsch GmbH, DE) as well as by an appositely built optical dilatometer (103), (104). In situ high-temperature optical microscopy is a powerful characterization technique in broad areas of materials science and engineering, and in the case of multilayers it can be used to determine the distortions and stresses that arise during co-firing. Optical dilatometry allows the direct measurement of the sintering characteristic of thin

ceramics without the application of any load, which could alter the sintering kinetics. With optical dilatometry a thin tape cast sample can be analyzed as it is, without the need of further processing which may change its density and therefore its sintering characteristics (105). It has been shown that the same samples showed a higher final density with a higher sintering rate when sintered in a push rod dilatometer (106). Optical dilatometry was therefore generally preferred to the push rod dilatometry.

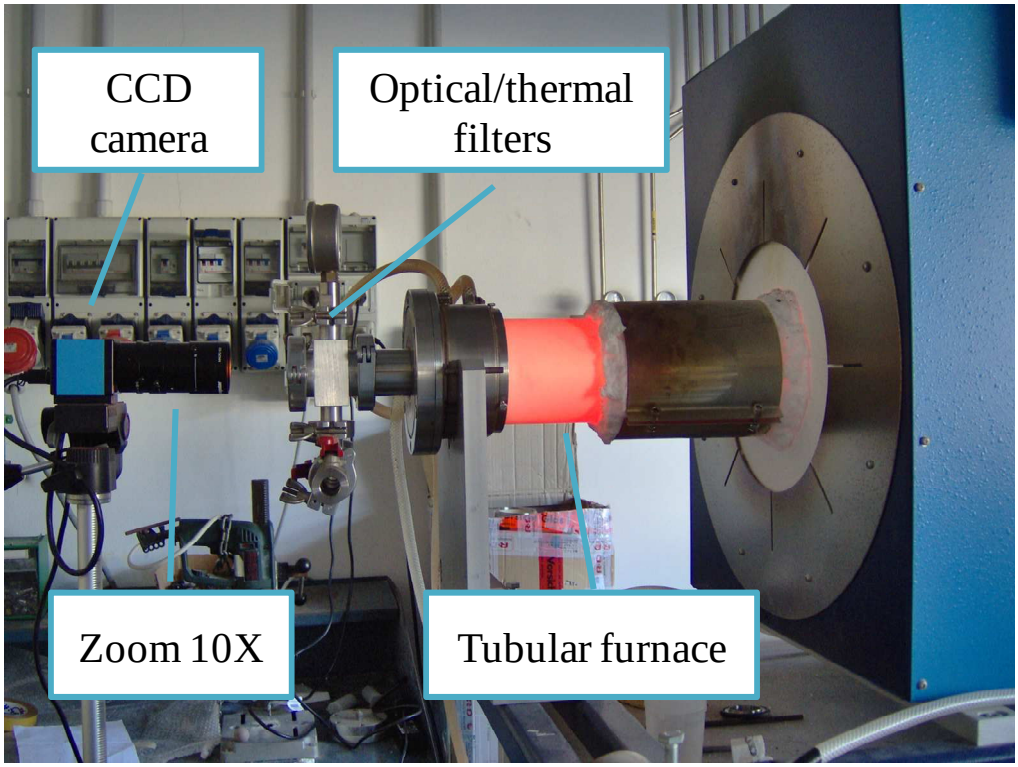

Fig. 20. Set-up for optical observation of sintering.

Monolithic tapes and bi-layers were sintered in a tubular furnace (HTRH 100-300/18, GERO Hochtemperaturöfen GmbH, Germany, Fig. 20) using the following sintering schedule: 1°C/min to 600°C, 5°C/min to 1100°C,

1°C/min or 5°C/min to 1450°C, 4h isotherm, free cooling. The furnace was specifically adapted for in-situ observations of the samples upon sintering: a silica glass window and a heat absorbing filter were sealed at one end of the alumina tube and pictures were recorded at 60 s intervals by a CCD camera equipped with a 10X macro zoom. A sketch of the apparatus is reported in Fig. 21.

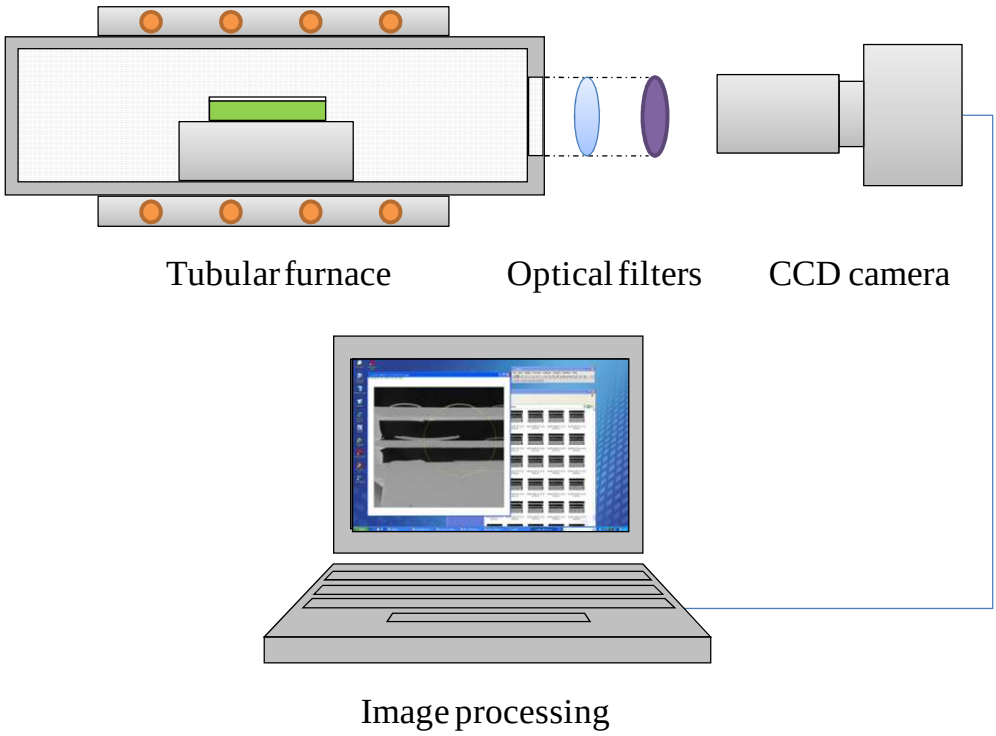

Fig. 21. Sketch of the set-up for sintering shrinkage and curvature optical observation.

The length of the single layers and the curvature developed upon sintering were measured directly from the photographs with an image processing software (ImageJ 1.38J). The bi-layers were positioned within the furnace

with the anode in contact to the bottom support; according to the convention chosen here, in the following description a positive curvature refers to a cell with the anode on the concave side, while a negative curvature refers to the anode on the convex side. At least two experiments for each condition were conducted in order to confirm the reproducibility of the data. The results obtained from the pictures were interpolated and analyzed using standard functions from a commercial data analysis software (Origin 7.0, OriginLab Corporation).

3.1.3 Cathode screen printing and cell testing

The cathode was applied on the sintered half-cells by screen printing. Screen printing technology and electrochemical tests were developed and performed by SOFCpower Srl, and are described more in detail elsewhere (35), (107), (108). Only a brief description of the testing apparatus will be given here.

Tests were performed using test benches developed by SOFCpower for single cells configuration (Fig. 22). The cell was sealed to an alumina tube with a high temperature sealant. A Pt wire was welded to metallic meshes (Au at cathode side and Ni at anode side) as current collectors. The cell mounted on the alumina tube was then inserted in a tubular furnace and heated up to 800°C with a rate of 1°C/min. The anode was then reduced in-situ under a forming gas flow and the cell was tested under flowing air at the cathode and humidified hydrogen flow at the anode. Labview software was used to control the data acquisition process.

I-V curves were collected from OCV condition up to maximum current density by increasing current by steps of 50 mA/cm^2. Electrochemical measurements of the cells were performed between 700 and 800°C flowing to the anode a 97% H_2-3% H_2O gas mixture at 150 Nml/min and to the cathode air at 300 Nml/min.

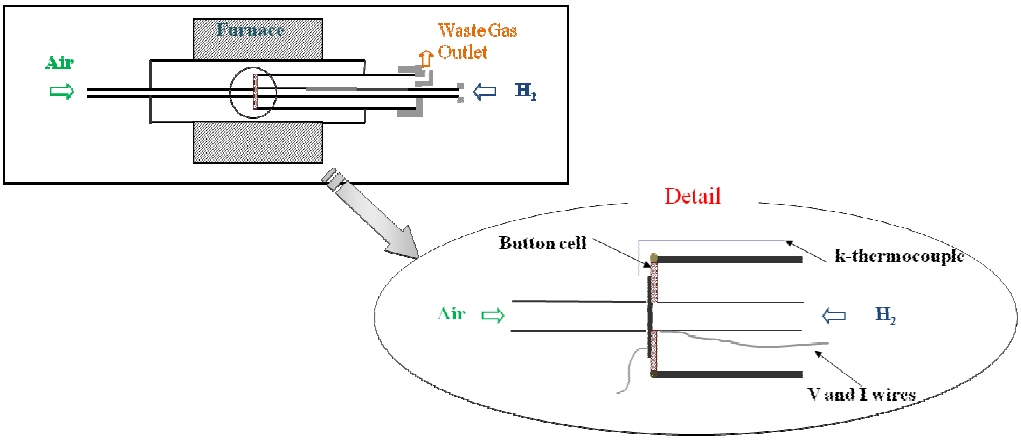

Fig. 22. Sketch of the testing apparatus (not scaled).

3.1.4 Other analyses

Different well known analyses were used in the experimental section. The viscosity of the suspensions was measured with a Brookfield DC-II pro viscosimeter, equipped with a sc4-16 spindle. Specific surface area (SSA) was determined by Nitrogen Adsorption (BET) method (ASAP 2010, Micromeritics, USA). The starting powders and the developed microstructures were characterized by scanning electron microscopy (SEM) using a Jeol JSM 5500 microscope (Jeol, Tokyo, Japan).

3.2 Optimization of suspension dispersion

3.2.1 Introduction

The viscosity of a slurry is one of the most important parameters in ceramic processing. Rheological measurements can be used both as an analysis methods, as well as a quality control technique to minimize batch to batch variation prior to consolidation (60). Rheological measurements can be used also as a direct processing variable. In the tape casting process, the solid loading of the suspension is usually desired as high as possible (with the exception of some very particular cases). A too concentrated suspension is however not desirable since it does not flow easily under the casting box blade. Rheological measurements are very useful in optimizing those requirements (60), (64).

In a colloidal suspension interparticle forces have a significant effect on its rheological behavior and its stability. The determination of the viscosity with different dispersant/powder ratio can provide fundamental information on the dispersion of the particles. The viscosity is decreasing as the concentration of the dispersant is increased. At a critical dispersant concentration, corresponding to the amount required to form a complete monolayer on particle surface, the viscosity reaches a plateau region. When the dispersant is used in excess, the viscosity is increasing again because of the excess polymer present in the suspension (109).

In this work the powder/dispersant ratio was optimized both with sedimentation tests (64), as well as with viscosity measurements. The results of the two analysis methods were consistent, but the latter method was found to be by far more practical and quicker. We report here only the results of the viscosity analysis.

The approach reported here for the production of stable colloidal suspensions suitable for tape casting is the following: first the optimal dispersant/powder ratio is found for each powder used by viscosity analysis on highly diluted suspensions. Then a suspension with the highest solid loading, which still gives to the suspension self-leveling properties is found by adding water dropwise to the powders, respecting the optimized dispersant/powder ratio. Once water and dispersant ratio are found, milling time, milling speed and the weight and shape of milling media are found for each specific optimized recipe via viscosimetry. The last step is to add binders and, if needed, other additives (surfactant, anti-foaming, thickener etc.) and to cast the slurry. The binder amount is chosen usually by trial and error methods, as the minimum quantity required to produce a green layer that does not develop cracks during drying, possesses enough strength and flexibility to be manipulated, peeled off from the support and cut in the desired shape. For the same powder, the needed binder amount is not always the same, but depends on the desired thickness, being the drying stresses depending among other factors (powder size, solvent type etc.), also upon tape thickness. As an example when a thin electrolyte (say 10 µm) is desired, low binder amount can be tolerated, but when the same powders have to be cast to form a thicker layer (say 200 µm), the same slurry formulation will not be suitable, and binder amount will have to be significantly increased. Usually for each recipe a critical thickness above

which drying cracks are developed can be defined. Under some special circumstances, binder/powder ratio amount can be tailored, in order to control green density of tape cast layers, and therefore the sintering properties.

The optimization of a ceramic slurry is a time consuming task, although when stable and well dispersed suspension are used, great benefits are gained from the final sintered products in terms of engineering properties (*e.g.* average strength, Weibull modulus, and in the case of SOFC electrochemical performances). Nevertheless, every single ceramic powder has to be optimized singularly, and there is not a single recipe, which can work with powders from different suppliers, although with the same chemical composition. For research and development purposes, when the starting ceramic powders have to be often varied, there is not always the time and even the need to fully optimize a recipe, but a compromise between an optimal slurry and a slurry which "works" has to be found. In the following chapters, the ceramic powders in the slurries formulation were always varied. Not always a fully optimized recipe could be developed. When the optimal recipe was not available, the dispersant/powder ratio was estimated from the acquired experience and the knowledge of the powder surface area, and was usually purposely overestimated. Binder and water fractions were also chosen by following the same principle.

In the following description we report the optimization procedure we used for an electrolyte and for an anode. This procedure is generally valid to develop new stable suspensions with different powders, solvents or dispersants.

3.2.2 Materials and methods

a) Electrolyte

100 g of 8 mol% YSZ powders (Unitech FTY 13.0-002H) were dispersed in 31 g of water, in a 250 ml jar half filled with zirconia grinding media. Darvan 821A was used as dispersant. Eight suspension were prepared with the following dispersant/powder ratio: 0.0 / 0.2 / 0.5 / 0.7 / 0.9 / 1.2 / 2.0 / 3.8 $g_{dispersant}/100g_{powder}$. The jars were rotated for 20 h by a roll mill.

b) Anode

58 g of NiO (J.T. Baker) and 42 g of YSZ (Tosoh TZ8YS) were dispersed in 31 g of water, in a 250 ml jar half filled with zirconia grinding media. Nine suspension were prepared with the following dispersant/powder ratio: 0.2 / 0.5 / 0.7 / 0.9 / 1.2 / 2.0 / 3.2 / 6.7 / 10.5 $g_{dispersant}/100g_{powder}$. The jars were rotated for 20 h by a roll mill.

c) Viscosity measurements

Apparent viscosity was measured with a Brookfield DC-II pro viscosimeter, equipped with a sc4-16 spindle. Suspensions temperature was controlled at

25.0 ± 0.2°C. Data were registered at 1, 10, 20, 50, 100, 200 rpm (corresponding to shear rate of 0.29 2.9 5.8 14.5 29.0 and 58.0 s^{-1}, respectively).

3.2.3 Results and discussion

Viscosity as a function of the shear rate at constant dispersant/powder ratio for the YSZ suspensions is plotted in Fig. 23; the viscosity as a function of the dispersant/powder ratio at a shear rate of 0.29 s^{-1} is plotted in Fig. 24. The observable minimum appears with a dispersant/powder ratio of 0.5 $g_{dispersant}/100\ g_{powder}$. The minimum value would be the same even by considering the higher shear rates.

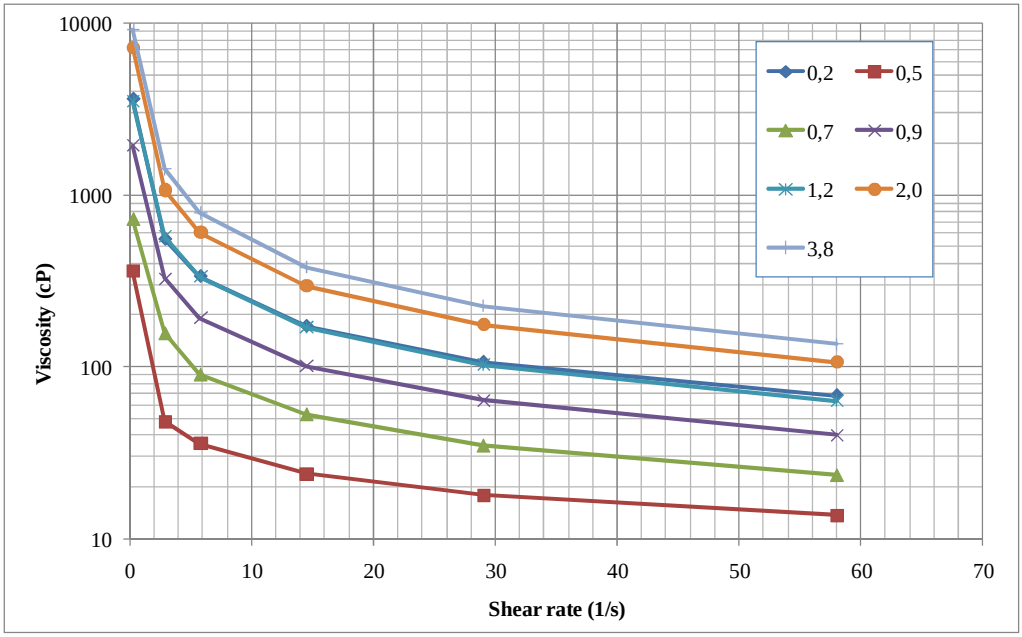

Fig. 23. Viscosity vs. shear rate at constant dispersant/powder ratio (YSZ).

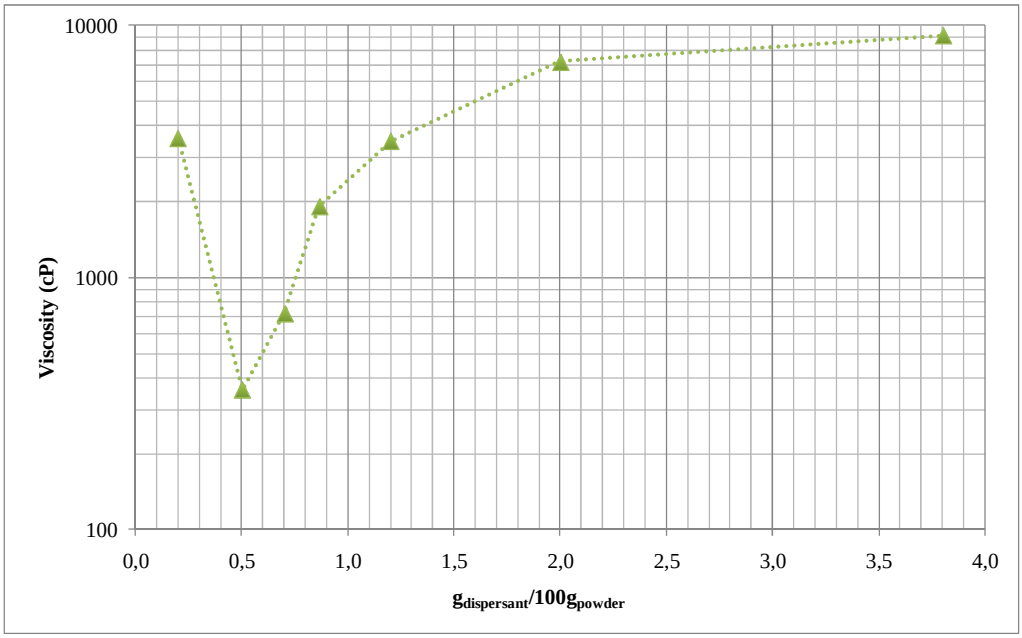

Fig. 24. Viscosity vs. dispersant/powder ratio at a shear rate of 0.29 s^{-1} (YSZ).

Viscosity as a function of the shear rate at constant dispersant/powder ratio for the NiO/YSZ mixture is plotted in Fig. 25; the viscosity as a function of the dispersant/powder ratio at a shear rate of 0.29 s^{-1} is plotted in Fig. 26. The viscosity shows a clear minimum at 0.5 $g_{dispersant}/100g_{powder}$.

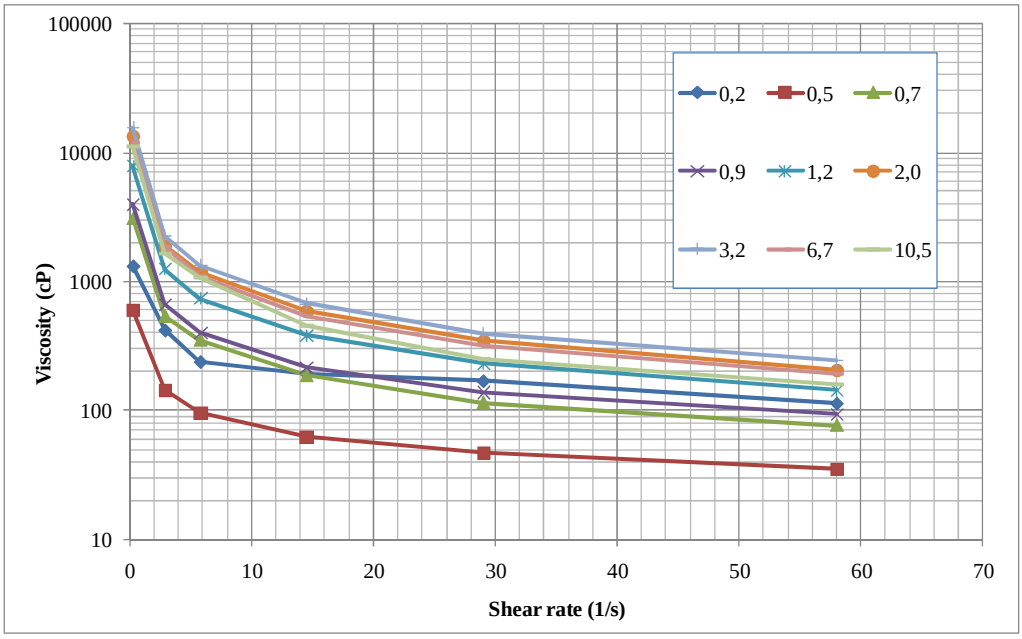

Fig. 25. Viscosity vs. shear rate at constant dispersant/powder ratio (NiO/YSZ mixture).

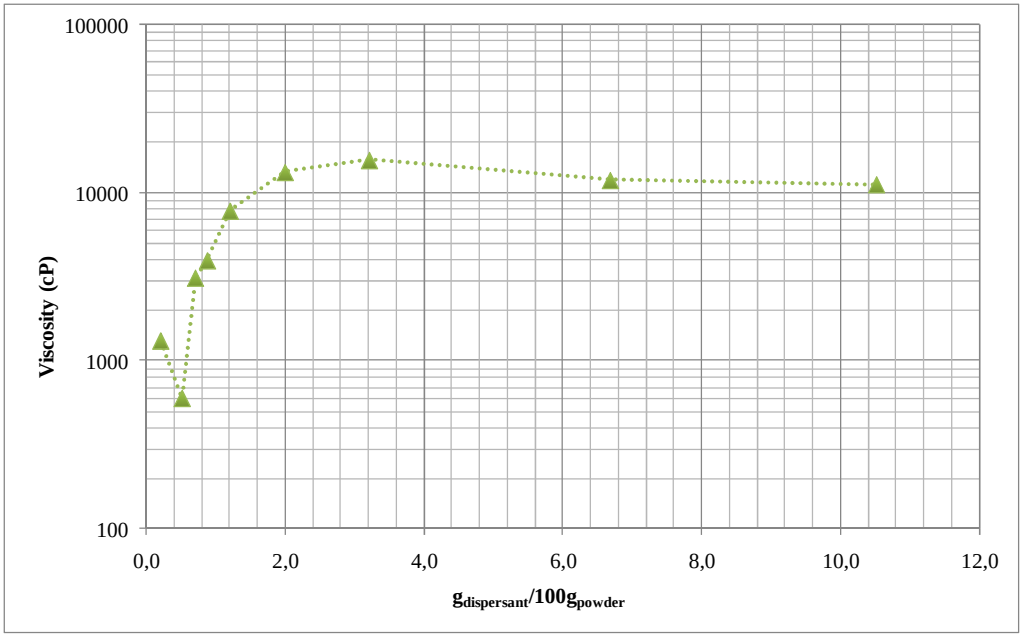

Fig. 26. Viscosity vs. dispersant/powder ratio at a shear rate of 0.29 s^{-1} (NiO/YSZ mixture).

As discussed in the introduction, the water in the optimized compositions was reduced in order to achieve the highest solid loading which allows the suspension to flow under the doctor blade. The such optimized suspensions consisted of 100g YSZ powder, 0.5 g dispersant and 19.2 g of water for the electrolyte, 100 g NiO/YSZ powder, 0.5 g dispersant and 18.8 g of water for the anode. The viscosity of this suspensions were measured as a function of the milling time, in order to find the optimal time. The results are plotted in Fig. 27.

Viscosity decreases for both suspensions with time, as the impact with the grinding media is breaking down the agglomerates and the dispersant is covering the powder surface. The viscosity of the YSZ suspension reaches an observable minimum after a milling time of 52 h, while the NiO/YSZ suspension reaches the minimum viscosity after 64 h. After this point the viscosity is increasing. A similar trend was observed by other researchers with different systems and was attributed to the degradation of the polymeric dispersant by the local heating effect caused by excessive ball milling (110). The optimal time for ball milling depends among other factors, upon the turning speed of the jar and the type and amount of milling media. As a general rule, the higher the impact energy of the milling media, the shorter will be the optimum time, but also the time for dispersant degradation.

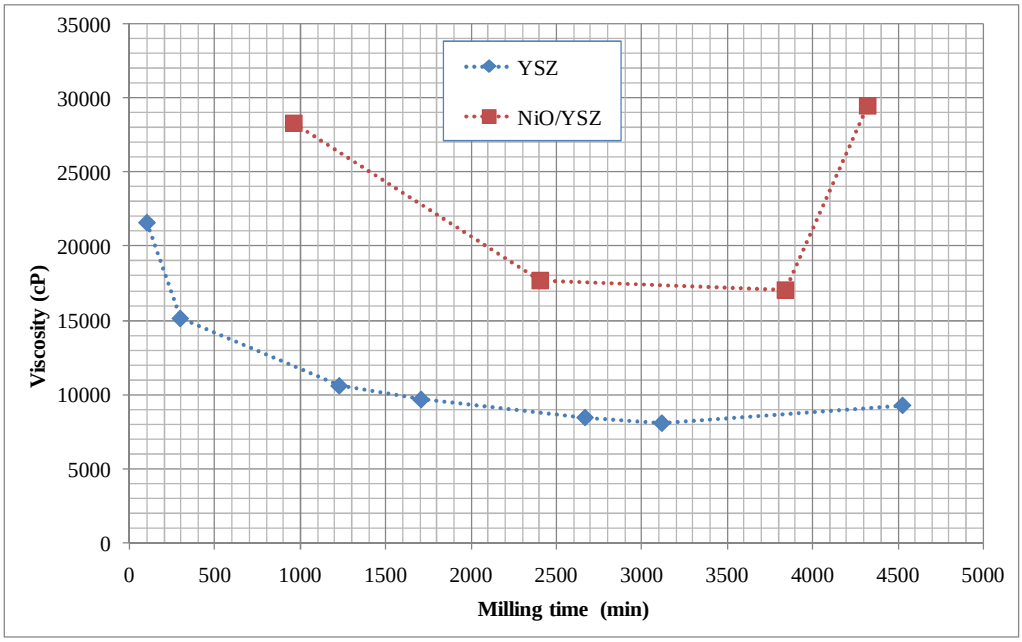

Fig. 27. Viscosity as a function of milling time at a shear rate of 0.29 s^{-1} (optimized YSZ and NiO/YSZ suspensions).

3.3 Controlling the sintering kinetics and the curvature in the co-firing of SOFC

3.3.1 Introduction

Planar anode supported solid oxide fuel cells are ceramic devices constituted of stacked layers of different materials each of them possessing different physical, chemical, mechanical and thermal properties, which are joined to form a multilayered structure (4), (38), (111). The fabrication of such devices typically requires the multi-step deposition and successive firing of the different layers. The cost of such high temperature treatments represents a significant fraction of the overall production expenses. In order to maintain the SOFC costs to an acceptable level, the production of the anode and electrolyte precursor layers by relatively cheap powder technologies, like tape casting or screen printing and subsequent one-step co-sintering, is the preferred route. ASC cells are typically obtained by stacking a thick anode (200 to 1000 µm) to a thin electrolyte (usually from 5 to 20 µm) and successive co-sintering; a thin cathode (10 to 50 micrometers) is then deposited on the electrolyte before final sintering. Among the different fabrication methods for planar solid oxide fuel cells, water-based tape casting represents an attractive production route due to its simplicity, high productivity and reduced environmental issues (4), (38), (64). Nevertheless, several technological challenges need to be analyzed in detail in order to define a reliable and efficient processing procedure. Among these, the

deformations and stresses arising upon co-firing of different materials with non-matching sintering behavior and different thermal and elastic properties is a crucial topic in the fabrication of a reliable device since they are responsible for degradation and failure of the fuel cell during the production process and upon service.

In the present work we report the production of anode supported electrolyte (ASE) solid oxide fuel cells with thin YSZ electrolyte and thick NiO/YSZ support anode by water base sequential tape casting and successive co-sintering, as a method for reducing the fabrication costs of SOFC, eliminating the needs for stacking and lamination steps.

Since the polymers used in this work as binders have low water solubility, it was possible to cast more than one layer on the top of the first one. This method allows the simple and inexpensive fabrication of multilayers with a potentially unlimited number of layers directly by tape casting without the need for further stacking and lamination process (5).

3.3.2 Challenges in co-sintering of anode supported SOFC

As it was discussed in the previous chapters, stresses are generated during co-sintering of multilayered ceramics due to the mismatch in thermal expansion coefficient and different sintering rate (73), (112). The stresses generated by dissimilar sintering rates are the primary cause of the deformation of the multilayers, specifically a curvature, which is developed upon co-firing; and if such stresses overcome the intrinsic strength of the layer, they can lead to flaws and defects formation (113), (114), (115), (116). In particular, sintering stresses mismatch is of the same order of

magnitude of the free sintering stresses, which in turn can be of the order of few megapascals. Such stresses are scaling inversely with grain size; nevertheless, in order to keep the sintering temperature to an acceptable level and to develop a sufficient fine electrode microstructure, SOFCs are generally fabricated starting from submicron sized powders and in some case from nano-sized powders. The elevated stresses which are developed upon co-sintering of fine powders compacts can reduce the effect of the sintering pressure and hinder densification, and in the worst cases can induce crack nucleation and propagation (75), (117), (118), (119), (120), (121), (122).

Co-sintering is a particularly delicate issue in SOFC processing: the anode needs to sinter in order to acquire enough mechanical strength to support the cell but needs to preserve sufficient porosity for fuel flow; conversely, the thin electrolyte acting as the gas separator between fuel and oxygen needs to densify at least to a point where it retains non interconnected porosity only. As a matter of fact, SOFC are not tolerant to the presence of defects and even a small crack in the electrolyte leads to leakage and hot spots associated to direct combustion that decreases electrochemical performances and accelerates degradation. Warping of the multilayer is also a limiting factor due to the tight tolerances typically required to pile-up cells in a stack. Moreover, any defect is detrimental for SOFC mechanical properties (123), which are of utmost importance in the real operation of a stack even for stationary applications, where the cells can be subjected to severe stresses deriving from external applied load or from thermal or RedOx cycles.

Various approaches have been used in order to solve the problem of the curvature developed upon sintering, *e.g.* firing under a dead-load in a one-stage process (124), (125), (126), (127), performing a second creep

flattening process after sintering (107), or using a loading plate sustained by ceramic arches which yield at high temperatures (128). Nevertheless, even if on a macroscopic scale such methods reduce the problem of curvature, on the microscopic scale they do not address the problem of crack growth and delamination, which can be caused by sintering rate mismatch. Moreover, they convey various disadvantages including contamination from the substrate and increased friction, which can lead to failure or increase in the sintering anisotropy (129).

The models discussed in previous chapters can steer the research towards the understanding of the co-sintering problems and solve them. From *Eq. 2-12*, one can appreciate that the developed curvature and stresses are dependent upon (i) geometrical parameters (thickness ratio), (ii) material properties (viscosity ratio) and (iii) difference in the free sintering rate of the two layers.

The directions to follow in order to reduce or control the stresses and the curvature seem thus to be essentially three. However the thickness ratio is usually fixed in the cell design. As far as the material viscosity is concerned, whereas in some ceramic multilayer technologies (*e. g.* LTCC), the material viscosity can be varied by tailoring the amount of glassy phase, in the SOFC this is not allowed. In fact glassy phases are generally undesired in SOFCs, and in particular SiO_2 is dramatically reducing YSZ conductivity, resulting in a loss of performances. It follows that only a careful matching of the shrinking kinetics of the layers constituting the cell seems to be the possible way. It is therefore crucial to reduce the anode and electrolyte sintering rate mismatch in order to reduce or eliminate the incompatibility stresses.

Many efforts are being currently done in order to reduce the curvature development and flaws generation, by varying the starting powder grain size

(130), (131), (132) through selective coarsening of NiO or YSZ powder (124), (133), or by optimising the electrodes sintering (134) or co-sintering temperature (135).

3.3.3 Approaches in co-firing SOFCs

a) Uniaxial sintering

Solid oxide fuel cell science and technology are relatively recent, and when it comes to develop the production of such devices there are a lot of unknowns. When a new technology is under development, it is useful to take a look to the closest technologies available and to learn from them. Ceramic or glass-ceramic multilayered devices are already being fabricated with a high productivity for a variety of industrial application. One of those applications are the low temperature co-fired ceramics (LTCC). Hot pressing is one of the techniques employed to produce flat and sintering defects free LTCC. In this technique, a uniaxial pressure is applied in the vertical direction during co-firing. This applied pressure increases the uniaxial shrinkage in the Z direction of laminates, whereas in plane shrinkage is reduced because of the presence of shear deformation caused by the uniaxial stress and friction with the pressing tools. The stress required in the Z direction to have zero strain rate in the X–Y directions of laminates is in usually in the range of 10–300 kPa for the LTCCs (86), (136), (137), (138).

It seems therefore natural to think that the uniaxial sintering method could be a applied to produce net shape and flat SOFCs. The application of a compressive load could enhances the effect of the sintering pressure in the direction of the applied load, while it could completely suppress the in-plane shrinkage, thus annihilating the stresses due to mismatch sintering rate of the different layers. Net shape and sintering defect free cells may be produced in this way. In order to maximize the load effect and avoid the cell failure, the load should be applied only at high temperatures, where the green ceramics possess a low viscosity, but before the complete densification, when the viscosity is increasing again (139). Nevertheless limited informations are found in the open literature on the application of such technology in the sintering of polycrystalline oxides and in particular in the SOFC field.

For this reason in the present work some experiments have been conducted in order to investigate the effect of the applied load on the cell densification. Green half-cells produced by tape casting were sintered free and under a constant load, which was applied from low temperature to the end of the sintering cycle. A higher load is required in order to obtain zero in-plane shrinkage in a SOFC compared to LTCC, since the viscosity of polycrystalline ceramics is higher than the glass – ceramic materials routinely employed in LTCC. The applied pressure was thus approximately 3 MPa. Cross section of pressureless and pressure assisted half-cells sintered for 2 h at 1380°C is reported in Fig. 28.

The green thickness was 345 µm. The thickness of the free sintered cell is 270 µm. The shrinkage is 22% and is almost isotropic in the three directions, and corresponds to a volumetric shrinkage of 52%. The electrolyte is still not completely dense, suggesting that either the

temperature or the dwell time were too low for pressureless sintering this sample. The thickness of the free sintered cell is 270 µm. The shrinkage is 22% and is almost isotropic in the three directions, and corresponds to a volumetric shrinkage of 52%. The electrolyte is still not completely dense, suggesting that either the temperature was too low or the dwell time too short for pressureless sintering this sample. The same sample sintered under a dead load resulted in a 155 µm thick cell (linear shrinkage 55%). The in plane shrinkage was negligible, thus the volumetric shrinkage was 55%. The electrolyte microstructure is denser in respect to the pressureless sintered sample. Uniaxial sintering under an external pressure could therefore be an effective way for reducing the sintering temperature as well.

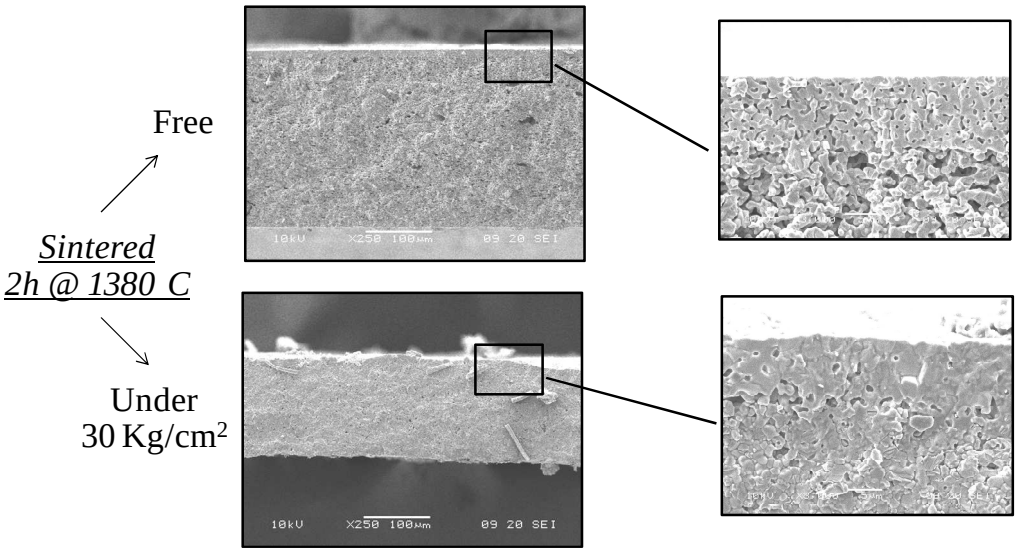

Fig. 28 Fracture surfaces of a green half-cell sintered for 2 h at 1480°C pressureless (top), under a dead load of 30 Kg/cm^2 (bottom). Green thickness 345 µm.

Nevertheless, this method conveys some disadvantages which complicate its application both in the lab scale as well in the industrial scale. In the lab scale, the application of a load implies the use of especially designed machines, such as high temperature press, and the use of pressing tools which do not stick to the cell. Technological issues arise from the necessity of distributing the pressure at high temperatures evenly on the whole surface of large area and thin samples. The diffusion of the highly mobile NiO from the anode substrate into the plates used for pressing is also a limiting factor, because it implies both a conductivity loss in the anode, as well as tools deterioration. Solid state reactions may take place as well. Its industrial application is also limited by the higher cost of the equipment and the technological issues associated with sintering with pressure, in respect to the pressureless co-sintering. It is worth to keep always in mind if we want to give a chance to the SOFC technology to compete with the more established ones in the field of electricity production, we need to make it become a relatively poor technology.
Therefore we concentrated our attention on pressureless co-firing.

b) Pressure-less sintering

In this work we varied the sintering kinetics of the green ceramics produced by water base tape casting following different approaches. While doing it was always kept in mind that the final microstructure had to be dense for the electrolyte and porous for the support anode. The shrinkage and shrinkage rate of the produced green layers were analyzed by optical dilatometry.

Green half-cells (anode and electrolyte) where produced with the most promising compositions by sequential tape casting. The same optical dilatometer was employed to follow the curvature developed upon sintering. This is in fact a direct experimental method which is giving much insight in the co-sintering process. The cells produced were electrochemically tested in order to evaluate the gas tightness of the electrolyte performance of the cell were

The general aim of this study was to study the effect of different factors on the sintering behaviour of the resulting green tapes and, therefore, on the curvature developed upon co-sintering of solid oxide half cells, with the final goal of minimizing the sintering stresses mismatch in order to obtain defect free and flat cells, eventually without the need of an external load.

More in detail, this chapter is divided into three sections: in the first section we studied the effect of the heating rate on the shrinkage and curvature rate. In the second section the effect of doping elements (Al and Ce) was discussed, and in the third section the effect of powder size and powder pre-conditioning was investigated.

3.4 Heating rate effect[1]

3.4.1 Aim of the analysis

The heating rate in the sintering of green ceramic oxides compacts is an important parameter. In the industrial practice in the field of traditional ceramics, generally a very slow heating rate is used in the sintering of massive ceramic pieces, in order to minimize the thermal gradients and the macroscopic deformation of the products. In case of technical ceramics, and more in specific in the SOFC field, the thin ceramic pieces possess generally a low thermal mass, and could withstand higher heating rates.

It is sometimes argued that a rapid heating to high temperatures is beneficial because it minimizes surface diffusion, while enhances bulk diffusion leading to greater densification. Rapid heating with low isothermal time at the maximum temperature can lead to fully dense microstructures with low grain growth (59), (106). Rapidly heating to high temperature could thus be an advantage for SOFCs, where the electrolyte microstructure has to be fully dense, or at least present only non interconnected porosity. Moreover, higher heating rate results in a faster production cycle, which in turn results in a cheaper final product. On the other side, in the case of a multilayer, a fast heating could increase the linear shrinking rate of the ceramic compacts, and therefore the difference in the rate of the single components, and intensify the developed mismatch stresses.

[1] *Adapted from: Cologna M., Bertoldi M., Sglavo V. M., "Water-Based Tape Casting and Co-Sintering of Bi-layers for SOFC Applications", 2nd International Conference on Ceramics, Verona, 29 June – 4 July 2008.*

For those reason the effect on the heating rate on the curvature, the curvature rate and on the developed microstructure was studied. Half cells were produced by tape casting and subjected to a slow (1°C/min) and a fast (5°C/min) heating ramp.

3.4.2 Materials and methods

Slurries preparation and tape casting procedure are the same as described in the general experimental section.

Two different 8 mol% Yttria Stabilised Zirconia (YSZ) powders were chosen for the electrolyte layer in order to determine the influence of the starting powders on the curvature rate of the half-cell with the same anode composition: the coarser powder (FYT13-002H, Unitec, UK) was used for the tape composition hereafter called E1, while the finer one (TZ8-YS, Tosoh, Japan) was used for the composition E2.

The ceramic powder for the anode cermet is a mixture of 58 wt% NiO (J.T. Baker Inc., USA) and 42 TZ8-YS. Slurry composition for anode and electrolyte are reported in Table 2.

Green tapes thickness was around 10 µm for the electrolyte and 265 µm for the anode. The bi-layers (total thickness 275 µm) were cut in rectangular cards with length of 10 mm and width of 1 mm for the curvature observation. After a slow de-binding step up to 600°C, the samples were subjected to the following sintering schedules: 1°C/min to 1450°C and 4 h isotherm, or 5°C/min to 1450°C and 4 h isotherm.

LSM/YSZ cathode was screen printed by SOFCpower Srl on button cells (active area 2cm^2), and the electrochemical test was performed as described in the general experimental section.

Table 2. Slurries composition (wt%).

Component	**Electrolytes**	**Anode**
Ceramic Powder	68,9	61,6
Solvent (Water)	23,8	24,5
Dispersant	1,1	1,9
Low T_g binder	3,1	9,0
High T_g binder	3,1	3,0

3.4.3 Results and discussion

The microstructure of the starting green electrolyte compacts is shown in Fig. 29 where the different grain size of the powders used here is clear.
The true free strains as calculated from the formula $\varepsilon = \ln (l(t)/l_0)$, with $l(t)$ the instantaneous length as a function of time (t) and l_0 the initial length, under two different heating rates, are reported in Fig. 30. Only the temperature range above 1100°C is reported in the graphs since no shrinkage due to de-binding was observed at lower temperatures.

As it is expected from the microstructure of the starting green compacts, the onset of observable shrinkage for the finer YSZ powders appears at lower temperatures; the shrinkage rate is also higher.

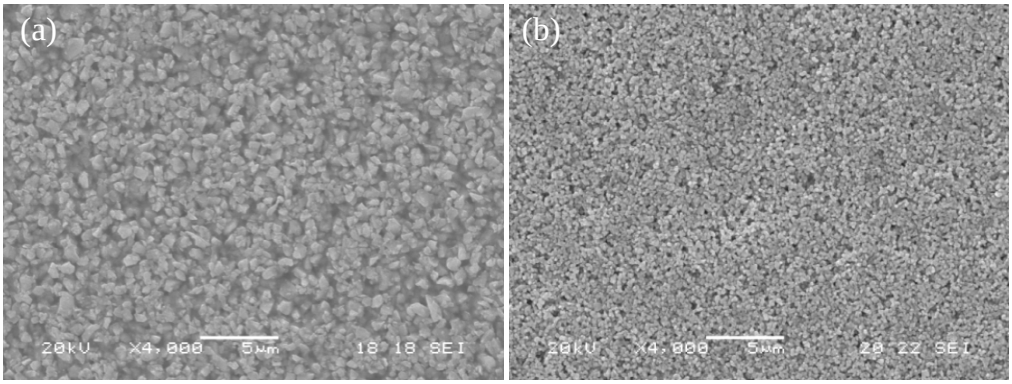

Fig. 29. SEM micrograph of the green tape E1 (a) and E2 (b).

The anode composition considered here shows an onset similar to the finer electrolyte composition, though the sintering rate in the first stages of sintering is lower. Similarly to previous observation this is not surprising since the anode considered here is composed of a mixture of fine YSZ powders and a coarser NiO powder, which slows down the densification rate.

The onset of densification and the shrinkage reached at the end of the dynamic heating step for all compositions depend strongly on the heating rate, the onset of observable densification appearing at lower temperatures for the 1°C/min heating schedule in comparison to the 5°C/min schedule. The absolute value of the final shrinkage is also higher when the slow heating ramp is used, probably because the whole sintering cycle is longer and the samples are subjected for longer times to high temperatures.

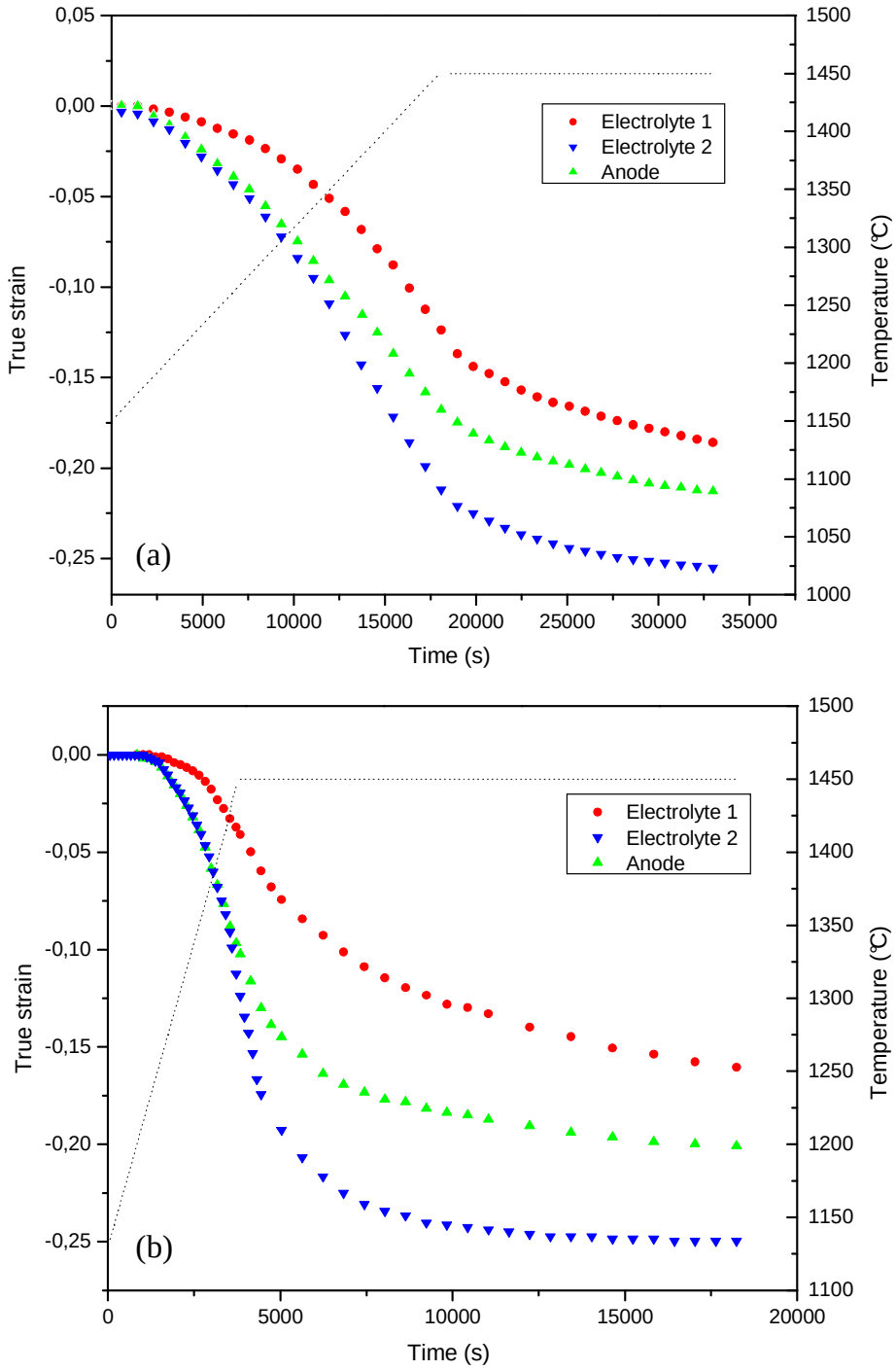

Fig. 30. Anode and electrolytes true strain. Heating rate 1°C/min (a), 5°C/min (b).

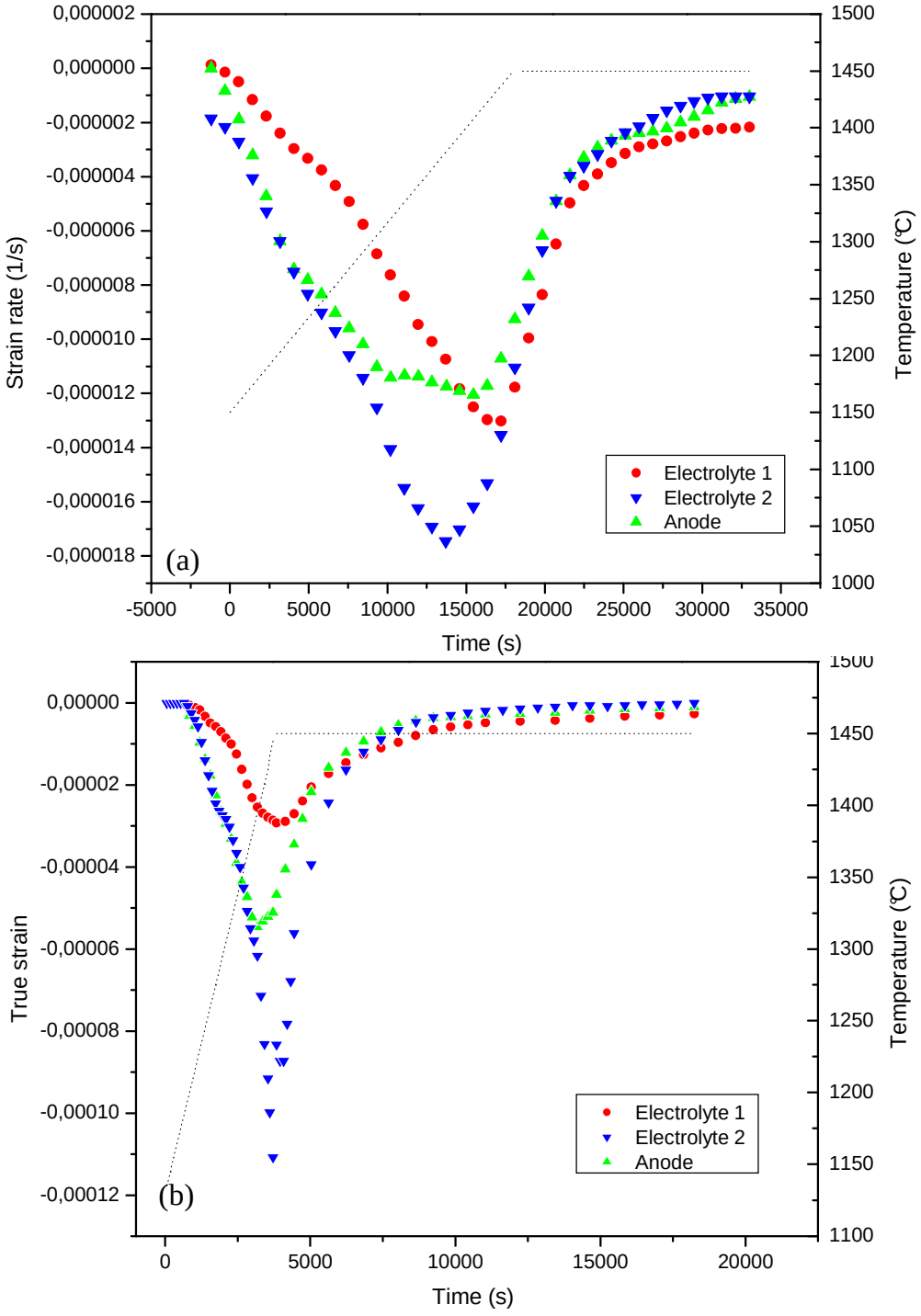

Fig. 31. Anode and electrolytes strain rates. Heating rate 1°C/min (a), 5°C/min (b).

By comparing the shrinkage rates (dε/dt) at 1°C/min or 5°C/min heating rates (Fig. 31), the absolute value for the peak shrinkage rate is always higher in case of fast heating and it is shifted towards higher temperatures.

The curvature (1/r, where r is the radius of curvature) and the curvature rate (d(1/r)/dt) of the bi-layers as measured directly from the pictures are reported in Fig. 32 and Fig. 33, respectively. All bi-layers were placed in the furnace with the electrolyte on the top and the anode in contact with the bottom support; according to the convention chosen here, in the following description a positive curvature refers to a cell with the anode on the concave side, while a negative curvature refers to the anode on the convex side.

The curvature rate for bi-layer E1/A (Fig. 33a) is first positive, then moves to negative values, and in the last stages of sintering becomes positive again. At the end of the heat treatment the cell is therefore curved towards the anode, having reached a state of minimum curvature in the intermediate stages of sintering. The curvature rate for bi-layer E2/A (Fig. 33b) is first negative, reaches a minimum and then inverts its tendency and becomes positive. Consequently, at the end of the heat treatment this cell is almost flat, even if in the intermediate stage of sintering it has reached an absolute curvature value higher than in E1/A. The curvature rate and the maximum curvature are always lower in case of samples sintered at lower rate, suggesting the benefit of a slow heating schedule in the co-sintering of multilayers. For each condition considered here, especially in the early stages of sintering, the curvature rates show the same trend of the difference in the free sintering rates of the single bi-layer components, this being in agreement with previous results (82), (103), (131), (140).

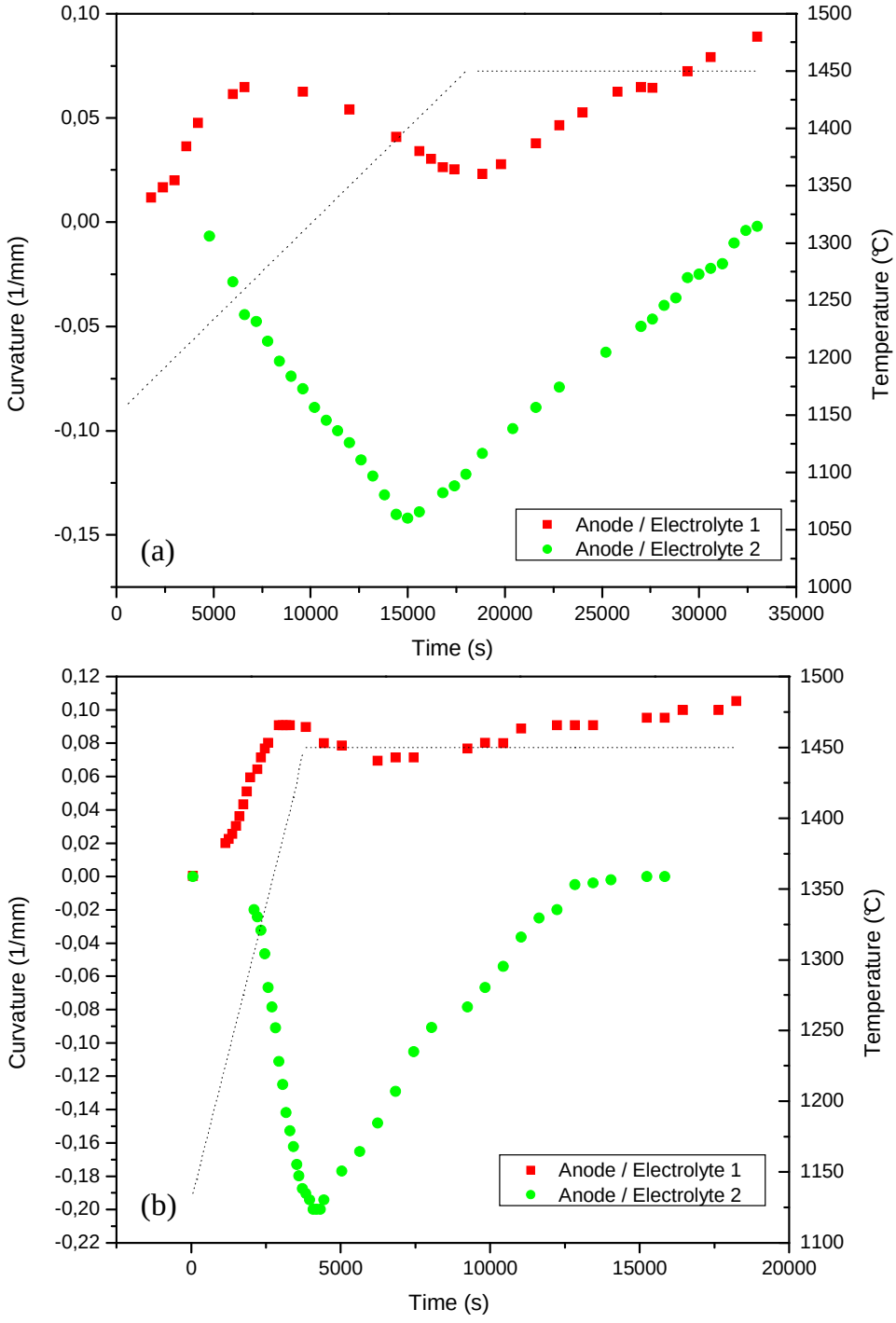

Fig. 32. Bi-layers measured curvatures. Heating rate 1°C/min (a) and 5°C/min (b).

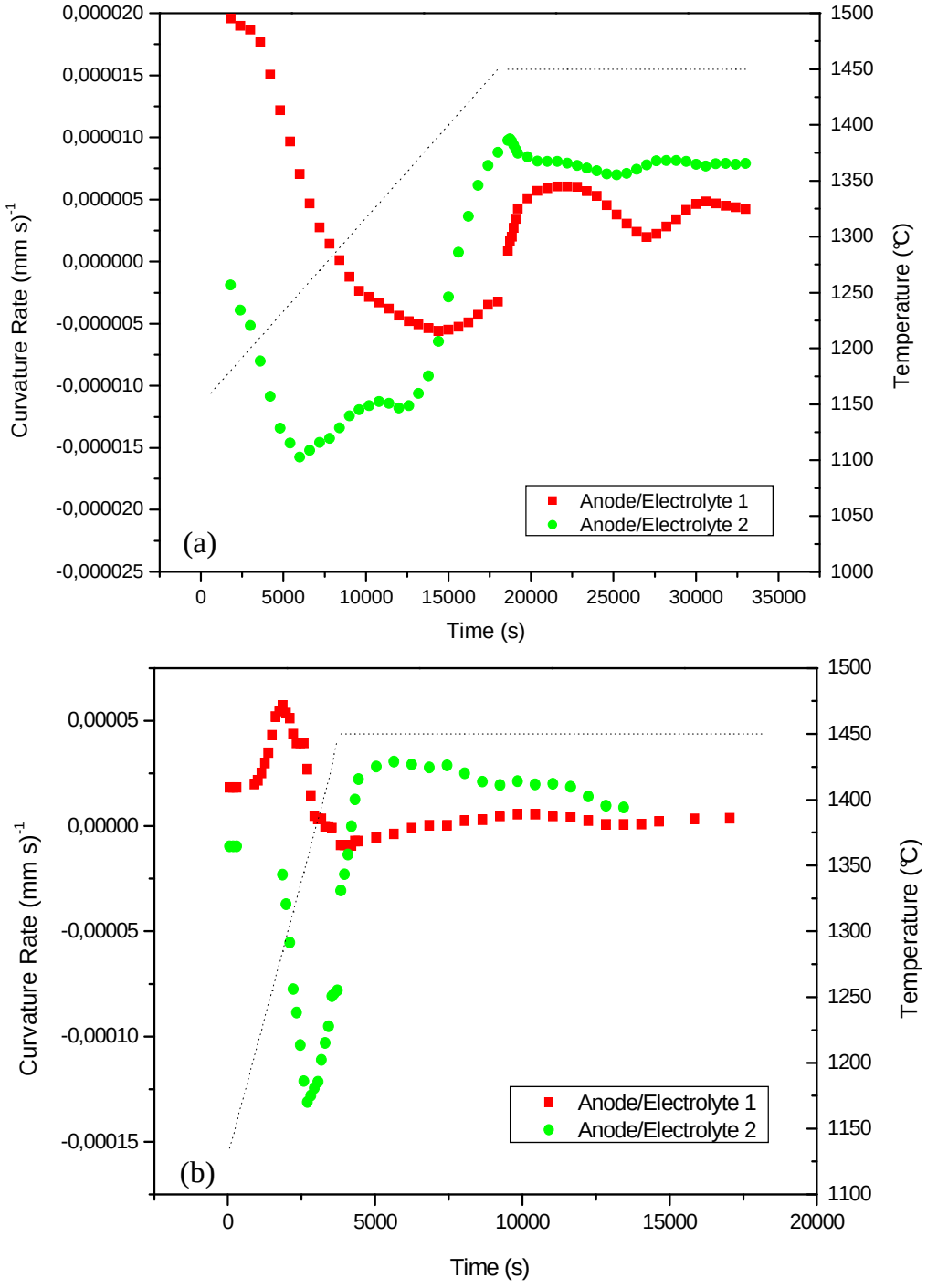

Fig. 33. Bi-layers curvature rates. Heating rate 1°C/min (a) and 5°C/min (b).

The developed microstructure of the sample sintered at 1°C/min is shown in Fig. 34. In both samples (E1/A and E2/A) the electrolyte appears gas tight and shows only closed porosity, the electrolyte with TZ8-YS powders looking slightly denser, while the anode porosity seems interconnected even before the reduction from NiO to Ni. No sign of delamination was found at the anode – electrolyte interface by examining the cross section of the cell; nevertheless, we observed a few cracks in the case of the sample E2/A by examining the electrolyte surface (Fig. 35). Such cracks are attributed to the stresses induced by the mismatch in sintering rate and are present only in the bi-layer with the higher curvature. Similar flaws were found by other researchers in case of co-sintering or sintering under tensile stresses (122), (132).

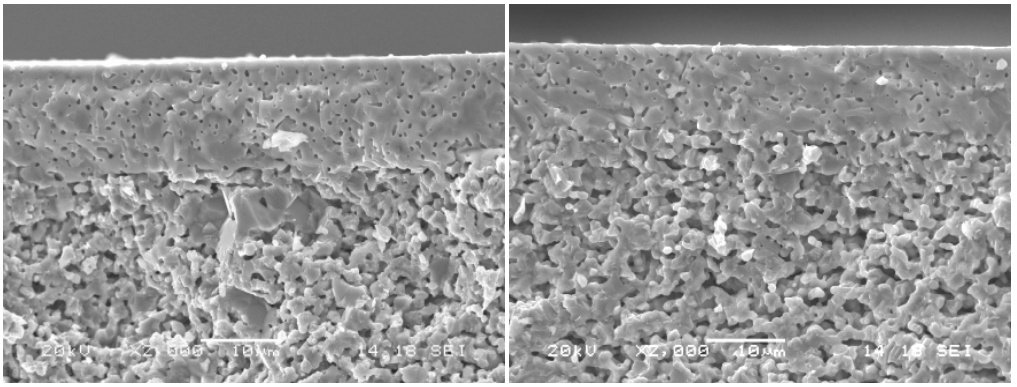

Fig. 34. Cross section of bi-layer E1/A (a) and E2/A (b) (sintering rate 1°C/min).

Because of the cracks observed in samples E2/A, only the bi-later E1/A was therefore electrochemically tested and the results are shown in Fig. 36. The open circuit voltage at 800°C was 1077 mV and the power density at 0.7 V was 556 mW/cm^2 with an LSM/YSZ cathode, suggesting gas tightness and absence of cracks in the electrolyte.

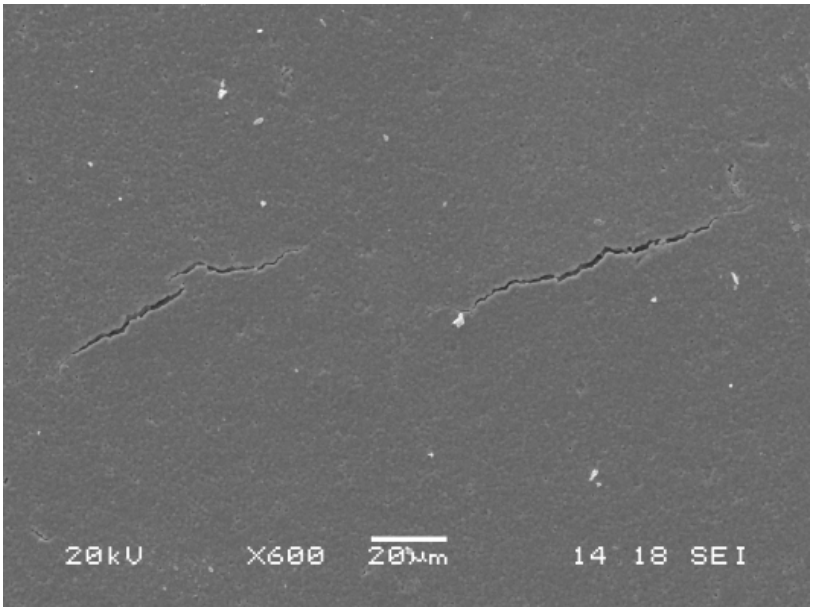

Fig. 35. Top view of sample E2/A, pointing out cracks developed in the electrolyte during sintering.

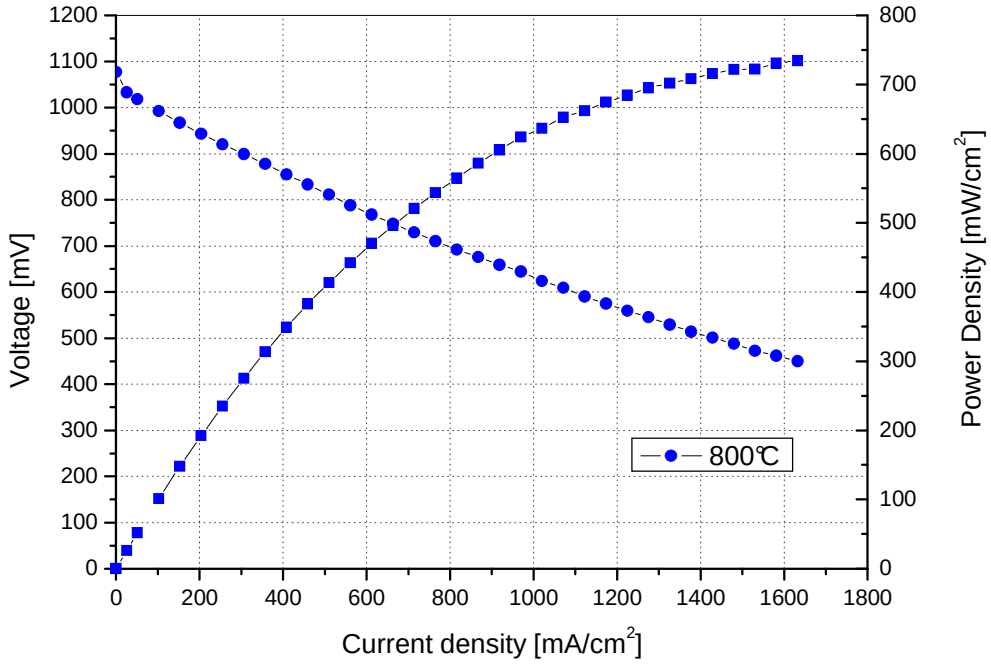

Fig. 36. Voltage/current density measurements performed at 800°C.

3.4.4 Summary

The possibility to follow the curvature developed upon sintering allowed the experimental demonstration that a slow heating rate was beneficial for limiting the developed curvature and that the sole observation of the final curvature after the complete firing cycle is not sufficient in determining the stresses developed during co-sintering and the quality of the electrolyte layer. Cracks arising from the mismatch sintering rate were found in the half-cell which was almost flat after sintering, while no flaws were found in the half cell that appeared more curled after sintering.

The electrochemical test of the cell demonstrated the very good quality of the obtained bi-layer.

3.5 Doping element addition[2]

3.5.1 Aim of the analysis

Yttria (8 mol%) stabilised zirconia (YSZ) for the electrolyte and a mixture of YSZ and Ni are by far the most studied and employed compositions in SOFC production (4), (31), (38), (133). Although such well known materials are the mayor constituents of anode supported half cells, a variety of doping elements are usually added in small quantities in both the anode and the electrolyte in order to enhance mechanical properties, electrochemical performances, long-term stability and resistance to RedOx cycles. For example, the addition of small quantities of Al_2O_3 (in the order of 1%) to cubic YSZ has been reported to act as sintering aid (141), (142), which enhances hardness and fracture toughness, reduces grain growth in YSZ electrolyte (143), (144) and significantly increases flexural strength of NiO/YSZ anode (145). Oxides like Cr_2O_3, TiO_2, Al_2O_3, and Sc_2O_3 can improve anode RedOx stability (146). Addition of small quantities of Mo (147), precious metals like Ru and Pt (148) or CeO_2 (149) has been observed to reduce the carbon deposition on Ni/YSZ anode during methane reforming. The use of CeO_2 has also been shown to improve the electrochemical performance of Ni/YSZ anodes (150).

[2] Adapted from: Cologna M., Contino A., Montinaro D., Sglavo V. M., "Effect of Al and Ce doping on the deformation upon sintering in sequential tape cast layers for solid oxide fuel cells", Journal of Power Sources. 10.1016/j.jpowsour.2008.12.052.

Despite the importance and the widespread use of reactive elements and sintering aids and the delicate issue of co-firing for the successful production of reliable cells, no specific studies have been carried out addressing the effect of doping elements on the anode sintering rate and, consequently, on the transient stresses developed upon co-sintering with the electrolyte, which are the primary cause for cell curvature and defect formation.

The aim of the work presented in this chapter, is to study the effect of selected doping substances (like Al_2O_3 or CeO_2) on the anode sintering kinetics and, consequently, on the cell curvature and curvature rate; in addition it is aimed to determine whether the addition of doping elements can be successfully employed to reduce defects development upon sintering and residual curvature, with the ultimate goal of obtaining flat and higher quality cells.

3.5.2 Materials and methods

Due to their wide use as doping elements for typical SOFC anode, Al and Ce were selected in the present work. NiO powder with 1, 3 and 5 mol% Al or Ce doping agent was produced by adding $Al(NO_3)_3 \cdot 9H_2O$ (Riedel- De Haen, Germany) or $Ce(NO_3)_3 \cdot 6H_2O$ (Alfa Aesar, Germany) to starting NiO powder (J. T. Baker, USA) in a plastic jar containing ethanol and zirconia balls (Inframat Advanced Materials, USA); the mixture was milled for 18 h. The powders were then dried and calcined for 10 h at 900°C. Pure NiO powder was also calcined for 10 h at 900°C for comparison. Specific surface area (SSA) was determined by Nitrogen Adsorption (BET) method (ASAP

2010, Micromeritics, USA). Doped NiO powder was mixed with 8 mol% yttria stabilised zirconia (YSZ) powder (TZ-8YS, SSA 6 m^2/g, Tosoh, Japan) in a ratio 58 wt% NiO and 42 wt% YSZ; binder (B1000, Duramax, Rohm and Haas, France) and distilled water were then added and the blend was mixed for 5 h in a rotating plastic drum containing zirconia balls. The powders were then dried and manually ground in a mortar. A portion of the obtained powder was then pressed at 125 MPa for 120 s into 20 mm diameter / 1 mm thickness pellets that were used for preliminary sintering analyses.

Anode and electrolyte were prepared by water-based tape casting technology, as described in the general experimental section. YSZ powder was used for the electrolyte; a mixture of 58 wt% NiO and 42 wt% YSZ powder was selected for the anode. NiO powder was screened through a 100 μm sieve, mixed with YSZ powder, water and dispersant (Darvan 821A, R.T. Vanderbilt Inc., USA) in a plastic drum containing zirconia balls. The electrolyte suspension was milled for 3 h in a Turbula mixer (Bachofen, Switzerland); conversely, the anode was mixed for 18 h in a conventional rotator mill. After de-gassing, binders were added (B1000 and B1014) and the mixtures were mechanically stirred for 2 h. Slurries composition is reported in Table 3. Green half cells were produced by casting the anode slurry on the top of the previously cast and dried electrolyte. The green electrolyte and anode thickness was 22 ± 2 μm and 420 ± 10 μm, respectively. The green bi-layers were cut into rectangular bars of approximately 10 mm length and 1 mm width for curvature observation; conversely, monolithic tapes were cut into bars of approximately 20 mm length and 5 mm width for shrinkage measurement. The samples were then sintered in at 1450°C for 4 h using a heating rate of 1°C/min.

A thin cathode (50 μm thick) was deposited by screen printing an ink containing equal weight of lanthanum strontium manganite and YSZ powders ($La_{0.65}Sr_{0.35}MnO_3$ - SSA 9.3 m^2/g, YSZ - SSA 13 m^2/g, Nextech Materials, USA) on selected samples (active area = 1.9 cm^2). Electrochemical tests were performed using specifically developed test bench for single-cell configuration, as described in the general experimental section, in order to evaluate the cells performance. Measurements were performed at 800°C; 150 Nml/min of 97% H_2-3% H_2O gas mixture and 300 Nml/min of air were flown to the anode and the cathode, respectively.

*Table 3. Composition of electrolyte and anode slurry (vol.%).**

Components	Electrolyte	Anode
Powder	28.4	21.3
Dispersant	1.5	2.8
Water	58.2	53.0
Binder	11.9	22.9

*Binder and dispersant are reported on dry basis.

3.5.3 Results and discussion

A first evaluation of the effect of the dopant addition on sintering behaviour of NiO/YSZ based anodes was performed on the pellets produced by pressing and sintering. It is well known that differences in the starting density in otherwise identical powder compacts lead to different sintering rates (151); therefore, the initial bulk density of the pellets was evaluated. Values equal to 3.17 ± 0.05 g/cm^3 were obtained for both Al- and Ce-doped pellets, therefore confirming the constancy of the starting density for the different compositions.

The true strain $\varepsilon = \ln (l(t)/l_0)$, $l(t)$ being the instantaneous length as a function of time (t) and l_0 the initial length, determined upon sintering of the pellets is reported in Fig. 37. For all samples, when the dopant concentration increases from 1 to 5%, the curves shift to the right; this means that the higher the doping level, the slower is the sintering effect. This behaviour is more evident for the Ce-doped pellets, where the peak of the maximum sintering rate occurs at 1325°C, 1340°C and 1355°C for 1, 3 and 5% Ce-doped specimen, respectively. In addition, one can observe that the sintering curves of Al-doped pellets are shifted to the left if compared to the diagrams corresponding to Ce-doped samples at the same doping level.

Based on the above results, the two limit cases, corresponding to NiO doped with 1 mol% Al and 5 mol% Ce, were selected as starting anode precursor powders for further co-sintering analyses of the anode/electrolyte composite system.

Micrographs of the selected NiO powders are reported in Fig. 38. As received NiO powder looks coarser than doped one. The powders surface specific area (SSA) as measured by the nitrogen adsorption method is reported in Table 4. One can consider an experimental error in SSA measurement of the order of 1 m^2/g; on this basis, after Table 4, the heat treatment has the effect of coarsening pure NiO powder, thus decreasing SSA. Conversely, Al or Ce nitrate addition may have a twofold effect: first, it can limit NiO powder coarsening upon calcination; second, it may slightly increase the measured SSA since the oxides which are formed from the salts possess a very high specific surface area.

Table 4. Specific surface area (SSA) of selected NiO powders.

	As received NiO	Calcined NiO	1 mol% Al - NiO	5mol% Ce - NiO
SSA (m^2/g)	3.3	1.6	4.4	4.1

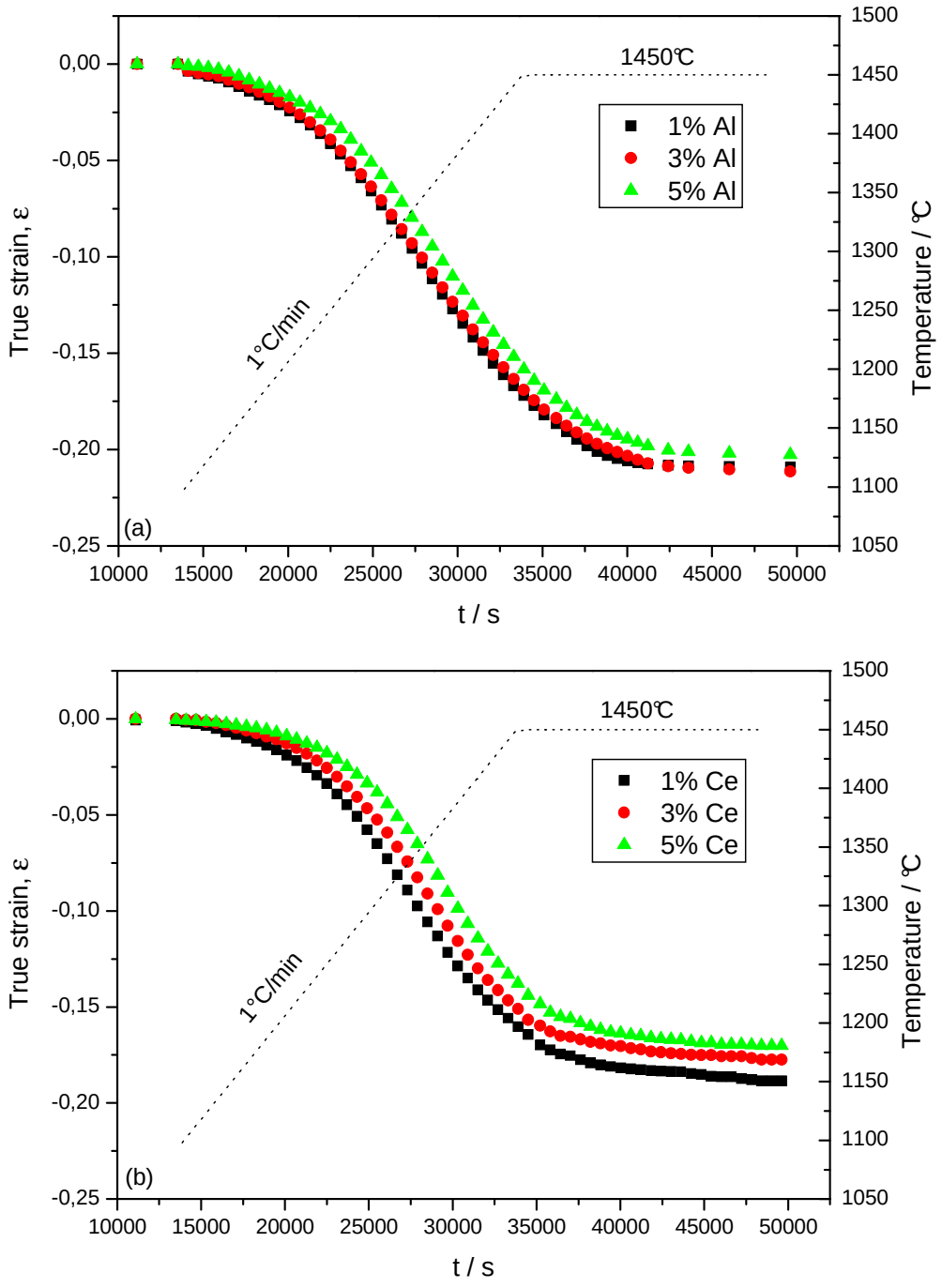

Fig. 37. True strain as a function of time for (a) Al- and (b) Ce-doped pressed pellets.

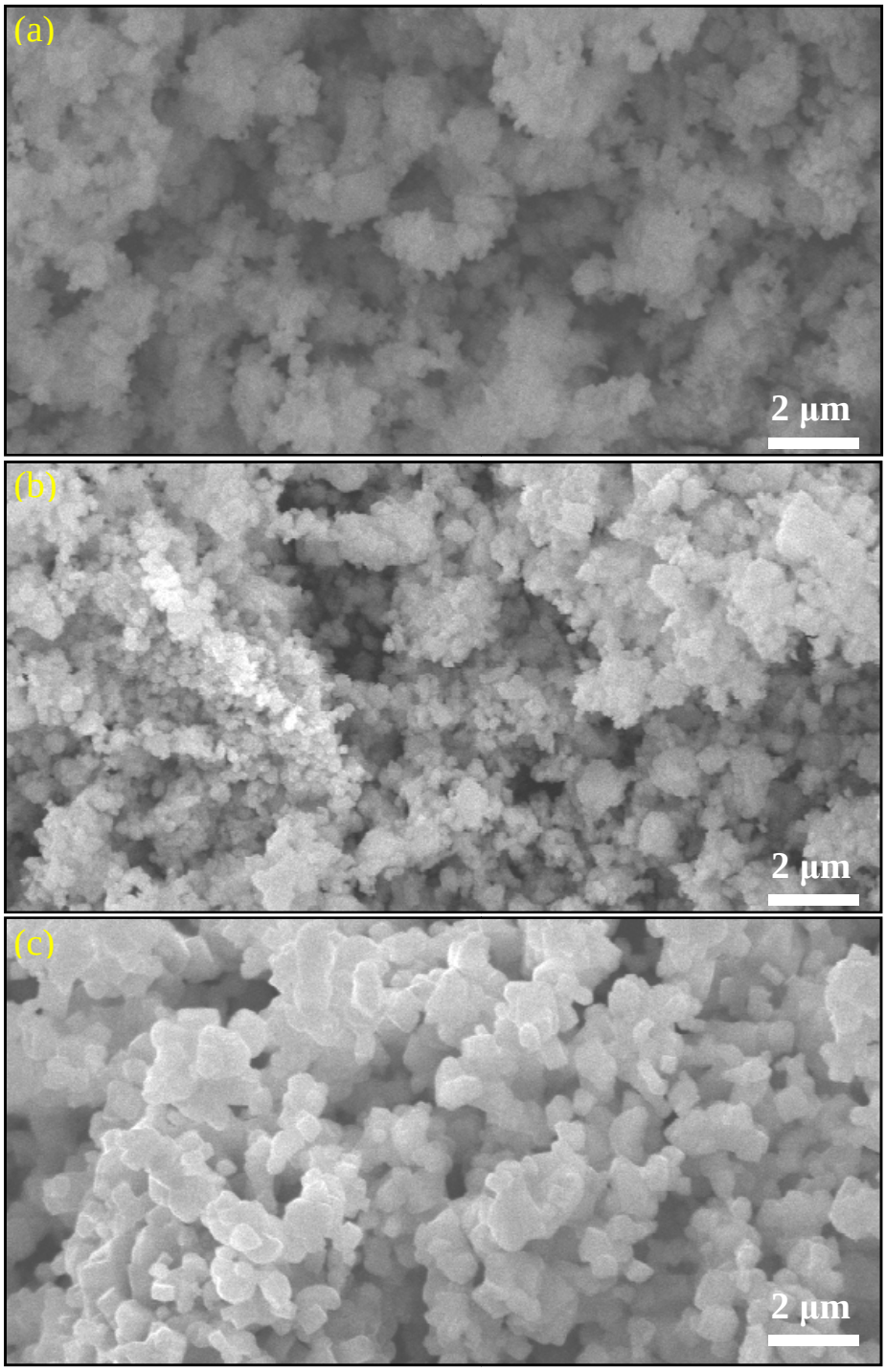

Fig. 38. Micrographs of the modified NiO powders. 1 mol% Al-doped (a), 5 mol% Ce-doped (b) and simply calcined (c).

Since the sintering behaviour depends also from the forming method (152), monolithic tapes were produced with the selected compositions in order to determine their sintering characteristics in the real condition. The anode green density was measured to be 2.48 ± 0.06 g/cm^3. The true strain and the shrinkage rate of the green tapes are reported in Fig. 39. The electrolyte is the fastest shrinking layer, with a maximum rate of $21.2 \cdot 10^{-6}$ s^{-1} (absolute value) at 1340°C. The Al-doped anode is the fastest sintering among the anodes, with a maximum rate of $13.7 \cdot 10^{-6}$ s^{-1} at 1340°C. A similar behaviour was observed both for Ce-doped and pure NiO anode. However, Ce-doped sample shows a slightly lower maximum rate at lower temperatures with respect to pure NiO anode ($10.3 \cdot 10^{-6}$ s^{-1} at 1375°C and $11.1 \cdot 10^{-6}$ s^{-1} at 1405°C for Ce-NiO and NiO, respectively). The largest mismatch in sintering rate between anode and electrolyte is $11.0 \cdot 10^{-6}$ s^{-1} at 1340°C for both Ce-doped and the undoped anode, while it is only $7 \cdot 10^{-6}$ s^{-1} at 1340°C for the Al doped anode. The curves for the tape cast doped anodes confirm the trend already shown by the pressed pellet sintering curves: i.e. Al is more effective in accelerating the anode sintering compared to Ce. Though no data can be found in literature addressing the influence of Al or Ce on a NiO/YSZ composite sintering rate, consistently with the results found here it has been reported that Al_2O_3 is acting as a sintering aid for 8 mol% YSZ (141), (142) while CeO_2 in concentration above 0.2% is decreasing the linear shrinkage rate in 3 mol% YSZ (153).

Three half cells were realised by casting the anode on a previously tape cast electrolyte and the curvature developed upon sintering was measured in situ. In order to minimise all possible errors, the three half cells were sintered in a single run; the developed normalised curvature $k = t/r$ (t being the layer thickness and r the radius of curvature) and the cell curvature rate are reported in Fig. 40.

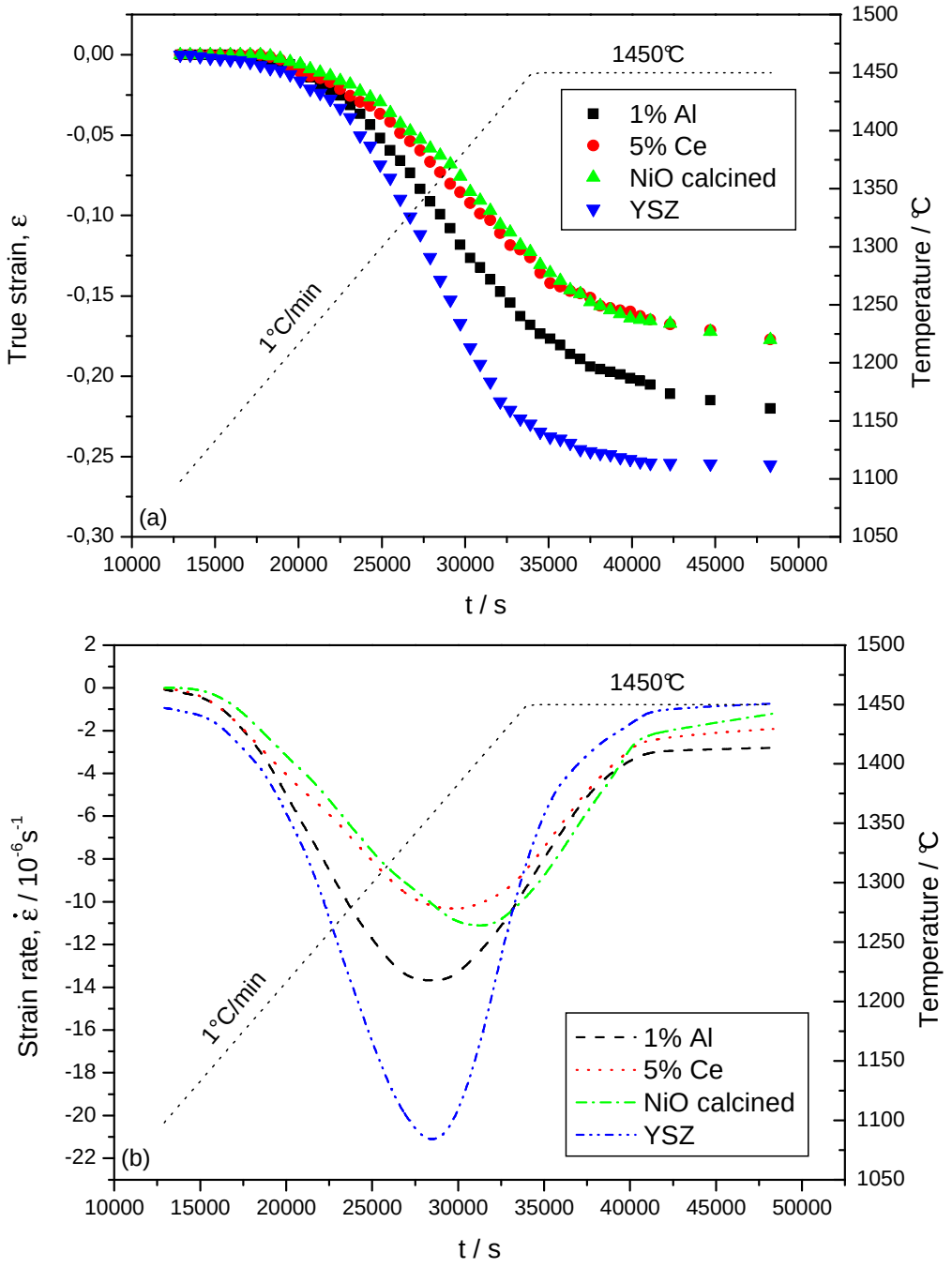

Fig. 39. True strain (a) and strain rate (b) as a function of time for tape cast layers.

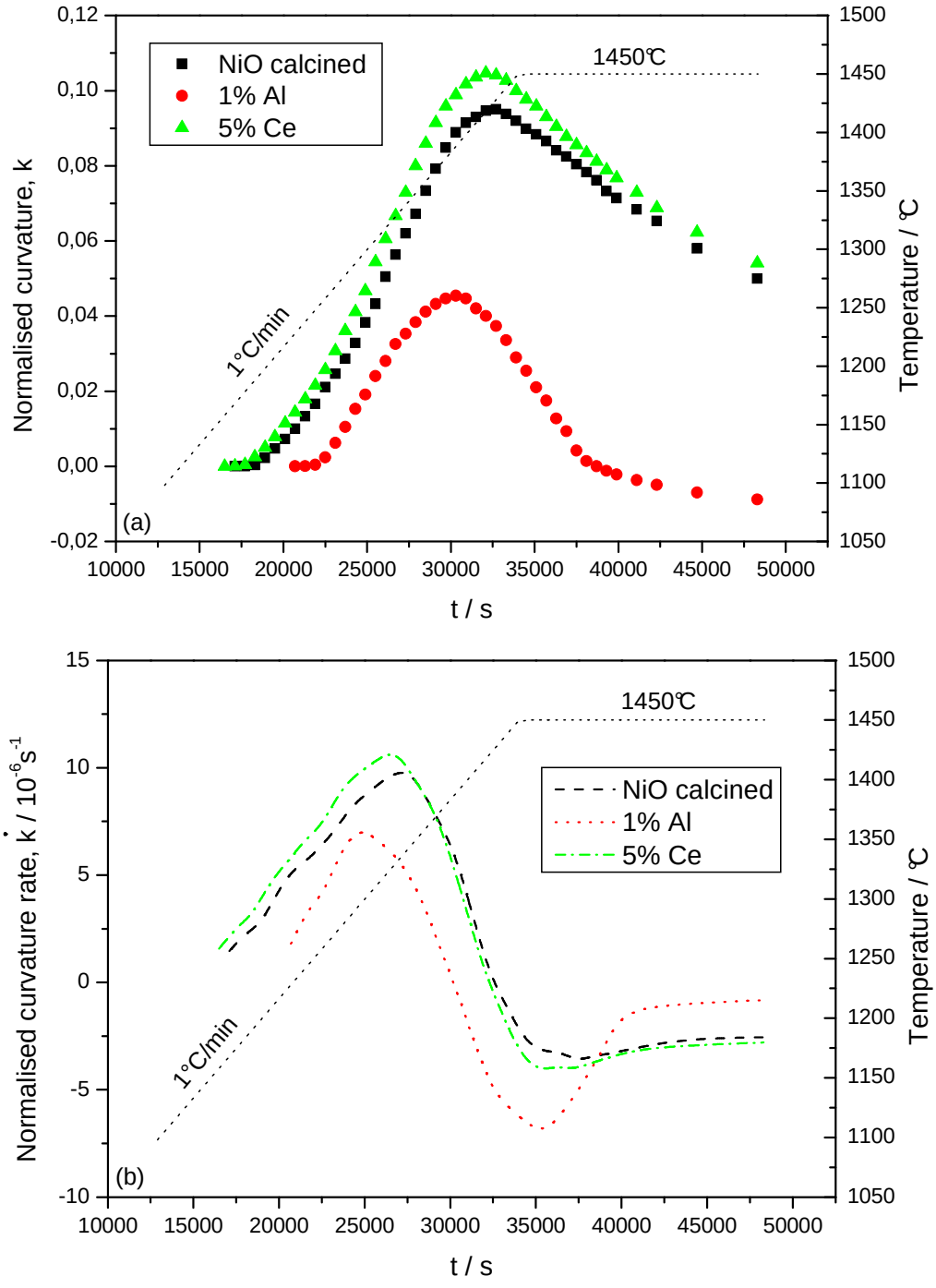

Fig. 40. Normalised curvature (a) and normalised curvature rate (b) of the half cells as a function of time.

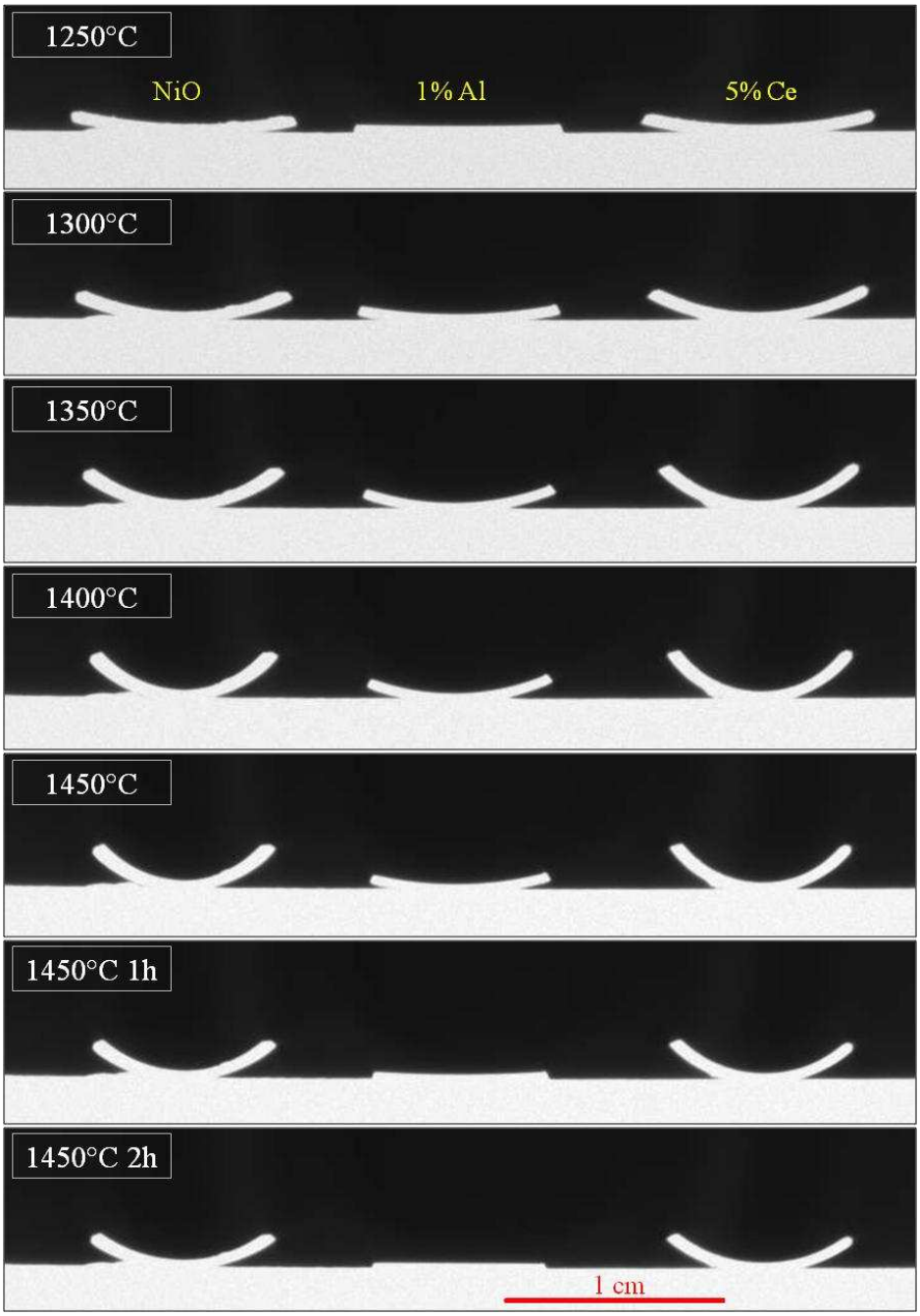

Fig. 41. Selected photographs of the half cells taken at different sintering times and temperatures. The samples are, from the left to the right: half cell produced with pure calcined NiO, 1 mol% Al-doped NiO and 5 mol% Ce-doped NiO. The electrolyte is the top layer.

Figure 41 shows a sequence of selected photographs of the three samples for clarifying the different behaviours. All cells are curving towards the electrolyte side in the firsts stages of sintering. Ce-doped and undoped cell start to curve around 1200°C; Al-doped cell show initial deformation around 1250°C. The normalised curvature continuously increases up to a maximum of 0.105 at 1420°C, 0.095 at 1430°C and 0.045 at 1390°C, for the Ce doped, the undoped and the Al doped respectively. After this peak, the curvature rate inverts its sign and the cells begin to curve towards the anode side. The maximum normalised curvature rate is $10.7 \cdot 10^{-6}$ s^{-1} at 1330°C, $9.8 \cdot 10^{-6}$ s^{-1} at 1340°C and $7.1 \cdot 10^{-6}$ s^{-1} at 1300°C, for Ce-doped, undoped and Al-doped respectively. It is worth noting that the only sample which totally recovers a flat configuration is the half cell with Al-doped anode, which is flat after an isotherm of 2 h at 1450°C.

The obtained results are in good agreement with sintering rates data collected on monolithic layers: according to Cai et al. (82) the curvature rate of a bi-layer is proportional to the free sintering rate of the two layers. The samples considered here are in fact curving towards the electrolyte when the electrolyte free sintering rate is higher than the anode one, and vice versa. The temperature of curvature rate inversion corresponds with good approximation to the point where the anode begins to shrink faster than the electrolyte. The samples which are subjected to higher curvature rate are those where the mismatch sintering rate between anode and electrolyte is higher (i.e. the Ce-doped and the undoped one), while the Al-doped sample shows a lower curvature rate, the dopant having the effect of promoting sintering and, therefore, matching better its sintering rate with the electrolyte one.

The developed microstructures after sintering are reported in Fig. 42.

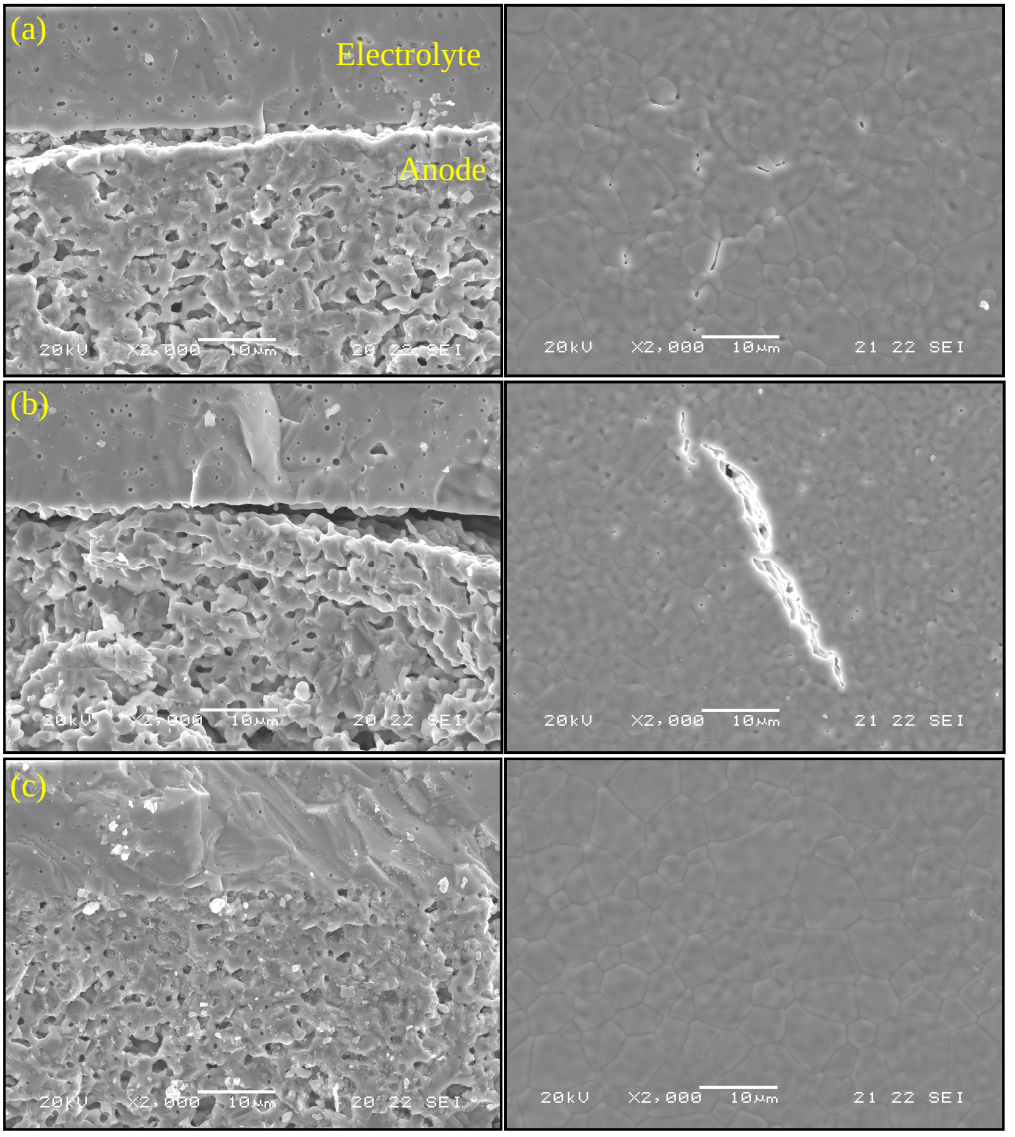

Fig. 42. Micrographs of the cross section (on the left) and electrolyte surface (on the right) of the sintered half cells. Calcined NiO (a), 5 mol% Ce-doped NiO(b) and 1 mol% Al-doped NiO (c).

By examining the electrolyte surface and cross section, one can notice that it is well densified in all samples and only closed porosity is present. The three anodes have retained enough porosity even before reduction to Ni.

Nevertheless, only the electrolyte stacked to Al-doped anode is defect free. Signs of clear delamination between anode and electrolyte can be detected by examining the cross section of Ce-doped and undoped sample and flaws are present on both electrolyte surfaces. The Ce-doped sample is the most severely damaged. It is worth to note that the defects could be detected only with careful SEM examinations, since all cells were not visibly cracked and the electrolyte appeared smooth and translucent at a first examination even with an optical microscope.

The cracks observed on Ce-doped and in undoped sample are interpretable in terms of the free sintering rates data of the monolithic layers and are in good agreement with the measured curvature rates. In fact it has been previously reported that the stresses generated in the sintering of multilayered ceramics are proportional to the curvature rate (or to the mismatch sintering rate) (82). The crack density on the electrolyte surface and their extension were found to be maximum in the cell that reaches the maximum curvature rate. Flaws or de-bonding defects similar to those reported here have been found in alumina/zirconia laminates (82) and in tape cast layers sintering under an applied load (122) and were thought to originate in the sintering stage, when the stresses (applied externally or originated internally) exceed the layer strength. Nevertheless, the determination of the exact moment for crack development is not straightforward: the developed stresses and the strength of the layers are continuously changing during sintering, being them dependent on other factors like temperature, density and grain size. It is however likely that such cracks initiate in the first and intermediate stages of sintering, when the layers strength is still low and the mismatch sintering rate is higher. Even if an exact quantification of the stresses and of the ceramic compact strength

requires the knowledge of the mechanical response of the ceramic sintering compact in every instant of densification, it can be foreseen that NiO/YSZ anode precursor layer possessing sintering rate curve between that shown by Al-doped anode and by the electrolyte, will be successfully co-fired with the electrolyte without cracks development.

Polarisation curves for cells produced with 1 mol% Al- and 5 mol% Ce-doped NiO and undoped NiO are reported in Fig. 43. The data are registered after the reduction and conditioning procedure used as a standard at SOFCpower labs and were recorded after a standard stabilisation time. All cells were compared under the same conditions. The aluminium containing cell shows an open circuit voltage (OCV) of 1054 mV and a power density at 0.7 V of 579 mW/cm^2 at 800°C. At the same temperature, the cerium containing cell possesses an OCV of 960 mV and a power density at 0.7 V of 368 mW/cm^2. The cell produced using pure NiO shows an OCV of 1055 mV and power density at 0.7 V of 241 mW/cm^2. The high OCV of the Al-doped NiO containing cell is a direct consequence of the gas tightness of the electrolyte in agreement with previous microstructural observations (Fig. 42c). The lower power densities measured for both Ce-doped and undoped NiO containing cells can probably be ascribed to the presence of defects mainly consisting of delaminating flaws which occur at the anode / electrolyte interface during the sintering process. The relatively limited OCV measured for the Ce-doped cell can be accounted for the presence of severe flaws within the electrolyte as shown in Fig. 42b. Conversely, the electrolyte of the cell made by pure NiO is less severely damaged, this being reflected by a still high OCV value.

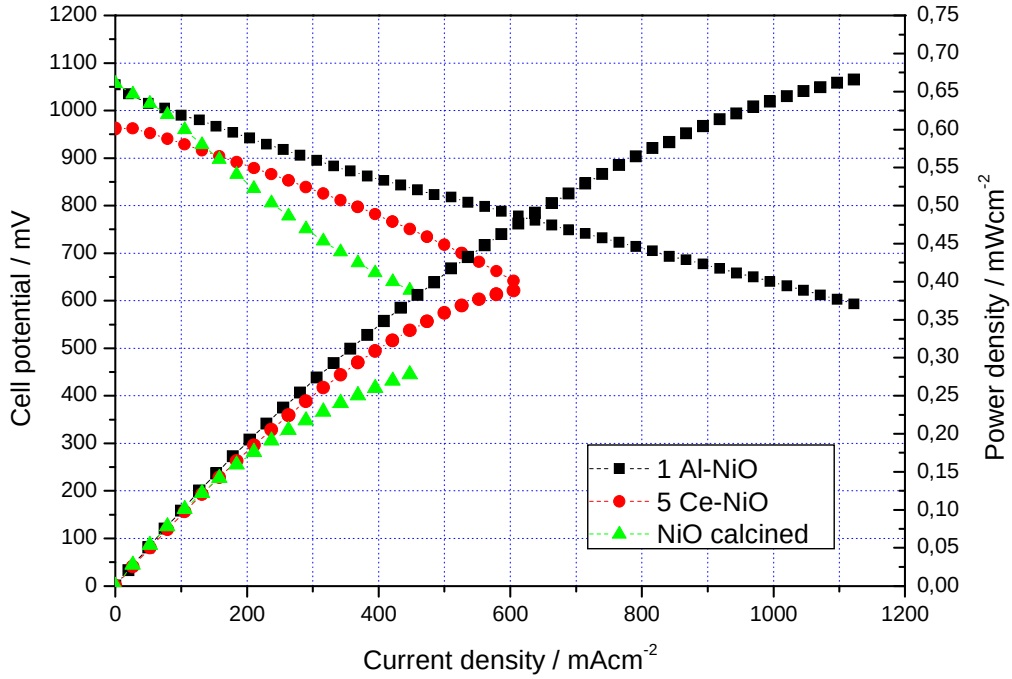

Fig. 43. Polarisation curves at 800°C for the cells produced with 1 mol% Al-, 5 mol% Ce-doped NiO and undoped NiO.

3.5.4 Summary

The influence of Al and Ce on sintering process of NiO/YSZ based anodes and on cell curvature developed upon co-firing was investigated.

The present work demonstrates how even a small addition of doping element can vary sensibly the sintering behaviour of SOFCs, thus being decisive in the successful production or failure of the device. In addition, the anode features cannot be simply modified by foreign element addition in the green state, because special care has to be addressed also to the effect this may have on the delicate issue of co-sintering with the electrolyte. Conversely, the use of reactive elements, if carefully controlled, can be

successfully employed to tailor the anode sintering curve, to reduce the mismatch sintering rate with the electrolyte and allow the attainment of flat and high quality cells.

More in detail, Al is shown to increase the anode sintering rate; the cell assembled with Al-doped NiO powders shows lower curvature rate and is perfectly flat at the end of the sintering cycle. The curvature rate and the number of defects are higher for the sample having larger mismatch sintering rate between anode and electrolyte.

High quality cells that show low curvature rates and are flat at the end of the sintering process can be obtained starting from 1 mol% Al-doped NiO powders. Microstructural observation confirm the absence of defects in the produced cells that result in high performances upon electrochemical tests.

3.6 Powder size effect[3]

3.6.1 Aim of the analysis

It was previously mentioned that one of the most important parameters in controlling the sintering rate of a ceramic compact is the powder size. It seems therefore natural to try to control the sintering rate of the anode and the electrolyte of the co-fired cells by tailoring the powder size of the ceramic.

However, when using this approach, we have to keep in mind that the choice of the row materials for cells production is subjected by some major limitations. In order to keep the sintering temperature and thus the firing cost to an acceptable level, the powder size has to be sufficiently small. Moreover the electrolyte in an anode supported has to be dense and its thickness has to be less than 20 µm (preferably 5 to 10 µm). Therefore the YSZ powder size for the electrolyte fabrication can range from the nanometer range up to a very few micrometers. Nanometric powders are not easily fully dispersed, and show high intrinsic sintering stresses which lead to very fast shrinking rates. Nanometric powders are usually more expensive as well. Therefore we steered our material selection to sub-micrometer and micrometer powders for the electrolyte production.

[3] *Adapted from: M. Cologna, M. Bertoldi, V. M. Sglavo "Sintering and Deformation of Solid Oxide Fuel Cells Produced by Sequential Tape Casting", International Journal of Applied Ceramic Technology, and M. Cologna, A. R. Contino, V. M. Sglavo, S. Modena, S. Ceschini, M. Bertoldi "Curvature evolution and control in anode supported solid oxide fuel cells" Ceramic Engineering and Science Proceeding 2009.*

As far as the anode is concerned, in our basic cell architecture the unique anode layer is acting both as the mechanical support, as well as the active layer close to the electrolyte where the electrochemical reactions take place. Whereas the mechanical support function could be maintained if the anode is produced by using coarse powders, the microstructure close to the electrolyte needs to be sufficiently fine in order not to suppress the catalytic activity. Therefore we selected only sub-micrometer and micrometer sized powders for anode production as well.

In the work described in this section, the starting microstructure of the green tapes was tailored in order to vary the sintering curves of the monolithic layers, with the aim of reducing the mismatch sintering stresses and, therefore, the curvature rate.

This was accomplished in two ways: in the first part of the present section different commercial powders and powder mixtures were selected and combined in both the anode and the electrolyte; in the second part of this section the commercial NiO powders were selectively subjected to a heat treatment in order to lower their sinter activity.

In this section it is demonstrated how the careful tailoring of the green microstructure can lead to the almost perfect superimposition of the sintering curves of the anode and the electrolyte, leading to a virtually uncostrained co-sintering, leading to cells which remain always flat during the whole process.

3.6.2 Effect of the selected commercial powder

a) Materials and methods

Three commercial ceramic powders were selected as starting materials: a) fine (d50 = 0.3 μm) 8 mol% yttria stabilised zirconia powder (TZ8-YS, Tosoh, Japan) – YSZf -, b) coarse (d50 = 0.7 μm) 8 mol% yttria stabilised zirconia powder (FYT13-002H, Unitec, UK) – YSZc - and c) nickel oxide powder (d50 < 1 μm, J.T. Baker Inc., USA)–NiO-. YSZc and YSZf powders were used to produce the electrolyte while mixtures of the three powders were used for the anode (Table 5). Water based slurries were prepared and cast as described in the general experimental section. The composition of the slurries used in the present study and tape casting parameters are reported in Table 5.

The electrolyte dry thickness was 12 ± 2 μm, the anode dry thickness was 270 ± 5 μm. The green bi-layers were cut in rectangular bars of approximately 10 mm length and 1 mm width for the curvature observation.

It was seen in another section of this chapter that a slow heating rate reduces the curvature rate in anode supported half cell. Therefore, in the present work a slow heating ramp from 1100°C to 1450°C was chosen. In detail, the following sintering schedule was always used: 1°C/min to 600°C, 5°C/min to 1100°C, 1°C/min to 1450°C, 4h isotherm, free cooling. The bi-layers were positioned within the furnace with the anode in contact to the bottom support; according to the convention chosen here, in the following description a positive curvature refers to a cell with the anode on the

concave side, while a negative curvature refers to the anode on the convex side. At least two experiments for each condition were conducted in order to confirm the reproducibility of the data.

A gadolinia-doped ceria (GDC) barrier layer and a lanthanum strontium cobalt ferrite (LSCF)/GDC (Nextech Materials Ltd., USA) cathode were screen printed on selected samples (active area 2 cm^2) and sintered and electrochemical tests were performed as described in the general experimental section.

Table 5. Slurry composition and tape casting parameters.

Raw materials and casting parameters	Electrolyte			Anode	
	E1	E2	E3	A1	A2
YSZf (g)	100	-	80	42	21
YSZc (g)	-	100	20	-	21
NiO (g)	-	-	-	58	58
Water (g)	23.0	23.0	23.0	18.5	18.5
Dispersant (g)	3.2	3.2	3.2	1.0	1.0
Binders (g)	43.2	21.5	21.5	39.2	39.2
Blade gap (µm)	30	30	30	500	500
Carrier speed (m/min)	1.8	1.8	1.8	0.6	0.6

b) Results and discussion

The microstructure of the as dried electrolyte and anode tapes is reported in Fig. 44. The dispersion of the powder is homogeneous for all the compositions and no defects can be found. As expected, tape E3 shows a microstructure in between E1 and E2, it being composed of mixture of fine and coarse zirconia powder. A2 has a coarser microstructure than A1 due to the presence of the YSZc.

The green powder densities were 2.79 ± 0.06 g/cm^3 for A1, 2.82 ± 0.05 g/cm^3 for A2, 2.51 ± 0.04 g/cm^3 for E1, 2.84 ± 0.04 g/cm^3 for E2, 2.78 ± 0.05 for E3.

True free strain, $\varepsilon = \ln (l(t)/l_0)$ and strain rate, $d\varepsilon/dt$, with $l(t)$ the instantaneous length as a function of time (t) and l_0 the initial length, are reported in Fig. 45 and Fig. 46, respectively. Only the temperature range above 1100°C is reported in the graphs since no shrinkage due to de-binding or sintering was observed at lower temperatures. The analysis of the curves in Fig. 45 and Fig. 46 allows the determination of some reference data (Table 6) that allows the comparison among different compositions. It is clear that the onset of sintering, sintering rates and their maximum are different for the various compositions studied here. For the electrolyte, due to the microstructure of the starting green compacts, the onset of observable shrinkage for the composition with finer YSZ powders occurs at lower temperatures, the shrinkage rate being also higher.

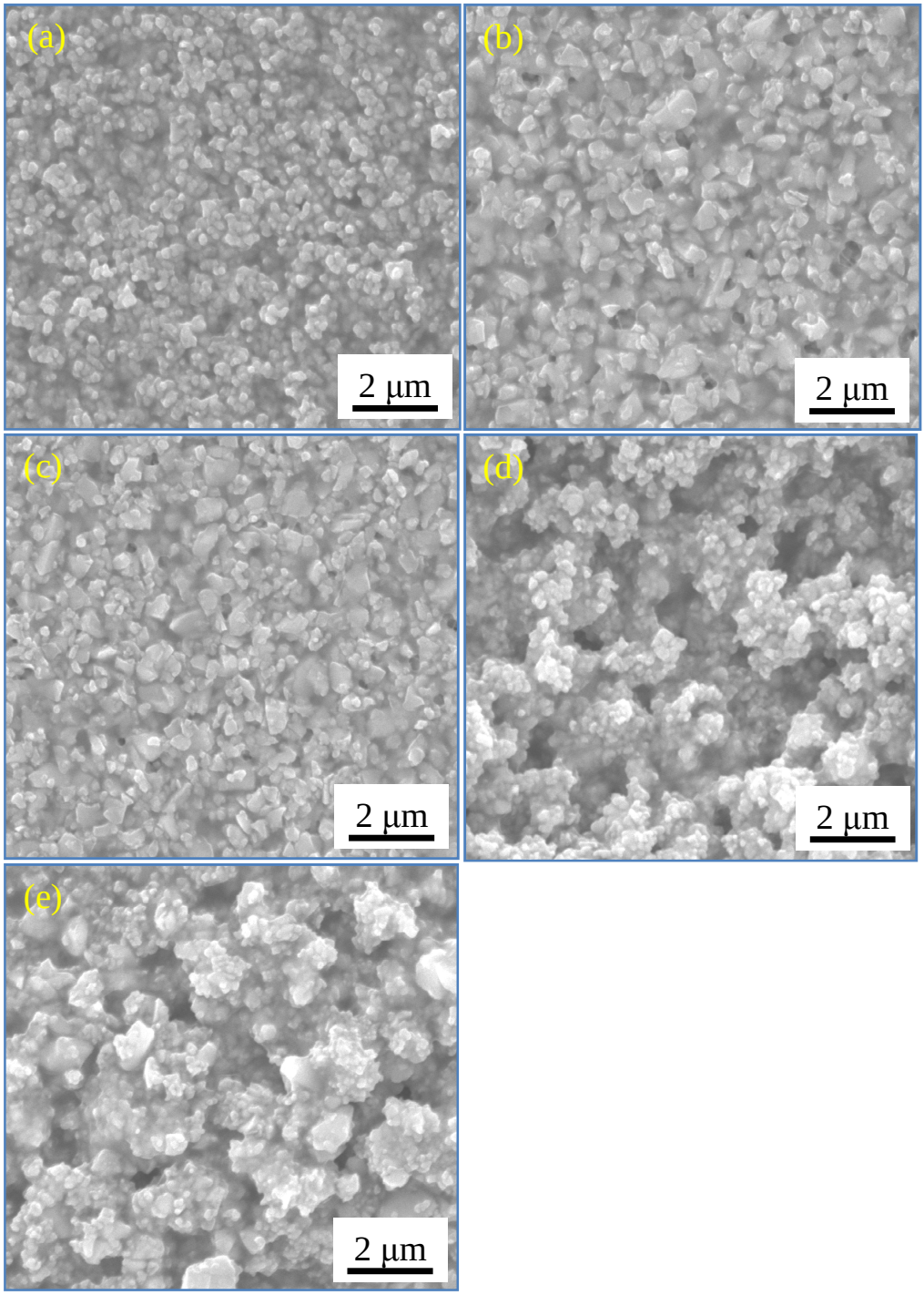

Fig. 44. SEM micrograph of the as dryed green tapes E1 (a), E2 (b), E3 (c), A1 (d), A2 (e).

The anode A1 shows an onset similar to the finer electrolyte composition, though the sintering rate in the first stages of sintering is lower. This is not surprising as A2 is composed of a mixture of fine YSZ powders and a coarser NiO powder, which slows down the densification rate. The presence of YSCc in anode A2 decreases densification rate. Conversely, by comparing E2 and E3, one can see how the presence of YSZf in the electrolyte E3 alters the sintering curve only slightly, shifting the peak of maximum shrinkage rate to lower temperatures (15°C less) with respect to E1.

It is known that not only powder size, but also green density has an effect on the sintering behaviour of powder compacts. The green densities of the anodes considered here are very close, while some difference appears among E1 and E2 (and E3). It is known that the higher the green density, the higher is the sintering rate (151). However, in this case, the powder size has a major effect over the sintering rate (in fact E1, which is the finer electrolyte, is shrinking faster compared to E2, despite E1 has a lower green density; if the green density was the same, the difference in the sintering rates would be even more pronounced). Moreover, it is not always possible by tape casting to produce samples using different powders but identical green densities, since every receipt has to be adapted to the used powder, which is affecting among other factors, also slip flow properties, green cracking and manipulability.

Table 6. True strain and strain rate data for the electrolyte and anode tapes.

	E1	E2	E3	A1	A2
Temperature at 1% ε [°C]	1195	1240	1240	1200	1230
ε at 1300°C	-0.07	-0.03	-0.03	-0.06	-0.03
ε at 1450°C (0h)	-0.22	-0.13	-0.13	-0.17	-0.11
ε at 1450°C (4h)	-0.26	-0.19	-0.18	-0.21	-0.18
$\lvert d\varepsilon/dt \rvert$ max [$10^{-6}s^{-1}$]	16.9	12.6	12.2	11.8	10.0
Temperature at $\lvert d\varepsilon/dt \rvert_{max}$[°C]	1390	1420	1405	1375	1435

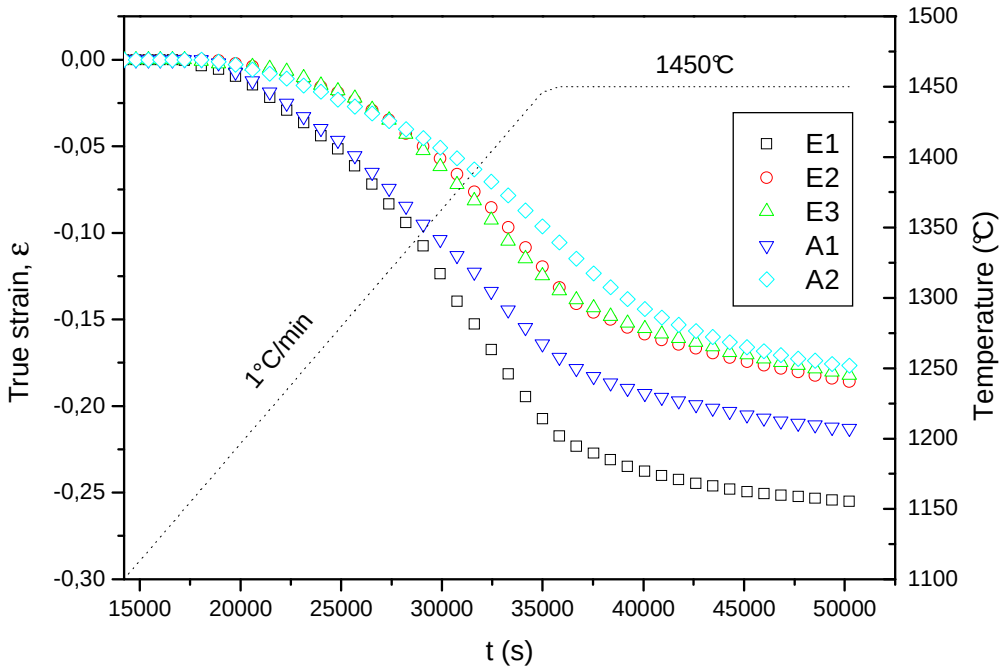

Fig. 45. True strains as function of time for tapes E1, E2, E3, A1 and A2.

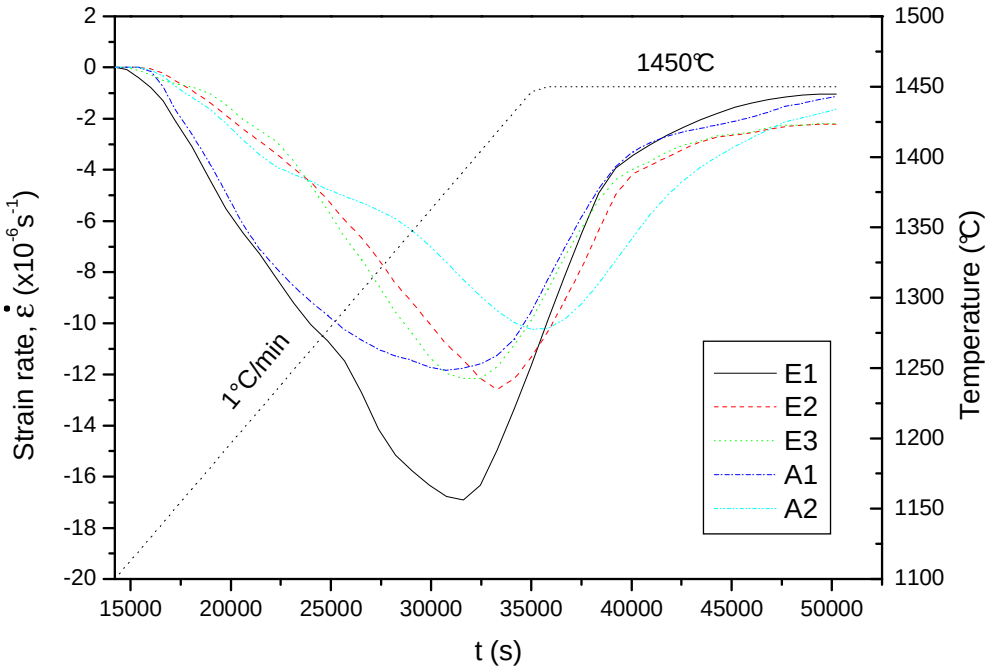

Fig. 46. Strain rates as function of time for tapes E1, E2, E3, A1 and A2.

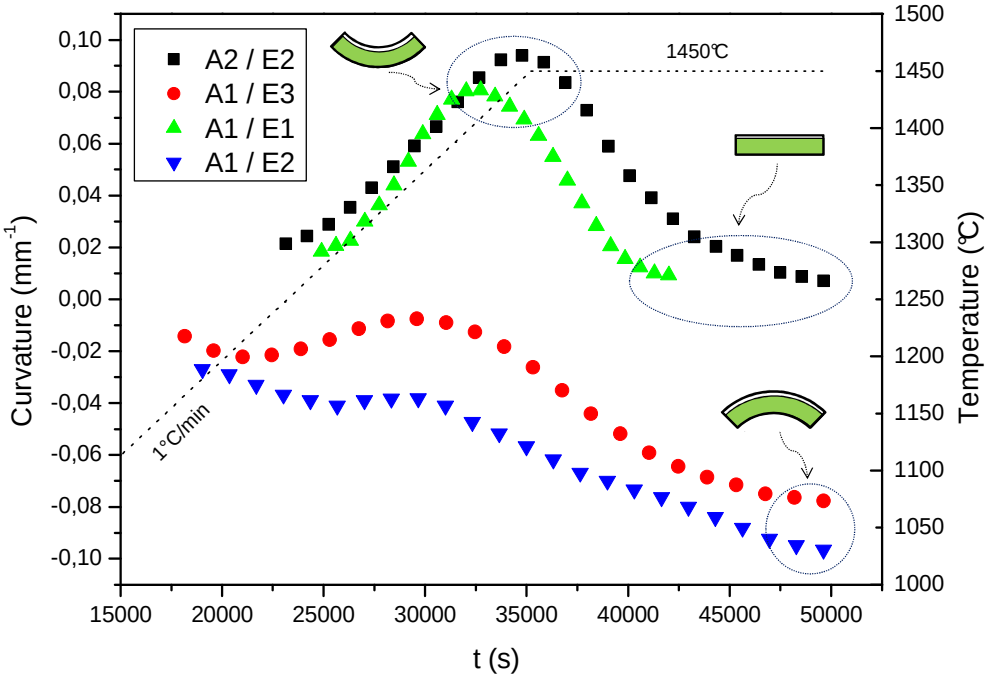

Fig. 47. Curvature of the selected half-cells as a function of sintering time.

A quantitative prediction of the mismatch sintering stresses and half cell curvature rate based would require to estimate some mechanical properties like viscosity and viscous Poisson's ratio of the two layers, which are not easily determinable being dependent upon density, grain size and temperature (73). Nevertheless, the reported equations allow some useful qualitative insight in the co-sintering stresses, these being strongly dependent on the mismatch sintering strain rate. In particular, the mismatch sintering stresses and the curvature rate are equal to zero when the two layers sinter at the same rate. It is therefore expected that a half cell with electrolyte E1 and anode A1 shows a positive curvature rate in the first stages of sintering, as the electrolyte tends to shrink faster than the anode; conversely, half cell produced with E2 and A1 should show a negative curvature rate. On the basis of such considerations, four different half cells were produced by sequential tape casting of electrolyte and anode, with the aim to reduce the differential sintering rates: A1 with E1, A1 with E2, A1 with E3, and E2 with A2.

Fig. 47 shows the curvature developed upon co-firing of the selected bi-layers and Fig. 48 and Fig. 49 show the corresponding curvature rates. A sequence of pictures of the samples A1/E1 and A1/E2 with the same anode but different electrolytes (fine and coarse powders, respectively) is reported in Fig. 50 to clarify the behavior upon sintering.

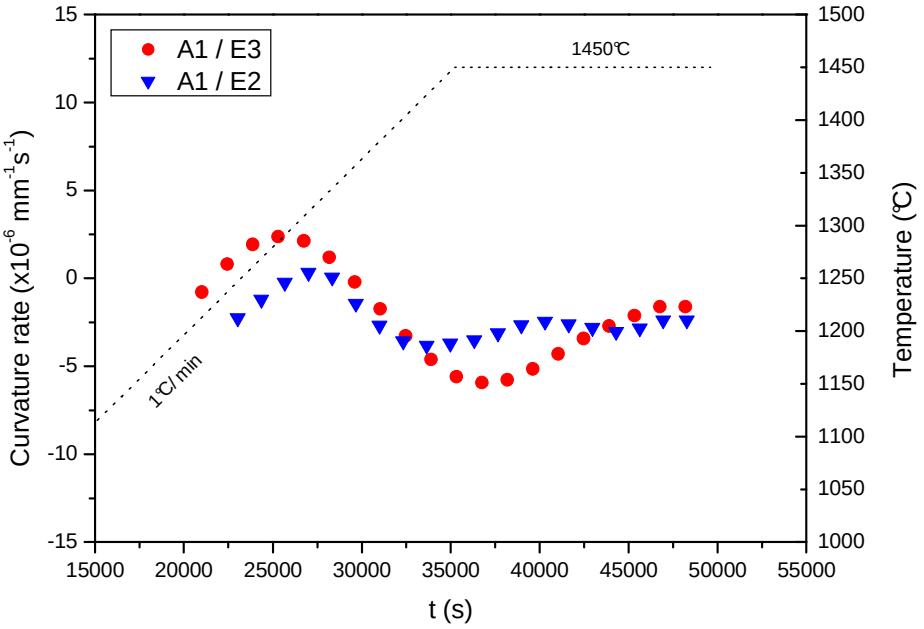

Fig. 48. Curvature rate of samples A1/E2 and A1/E3 as a function of sintering time.

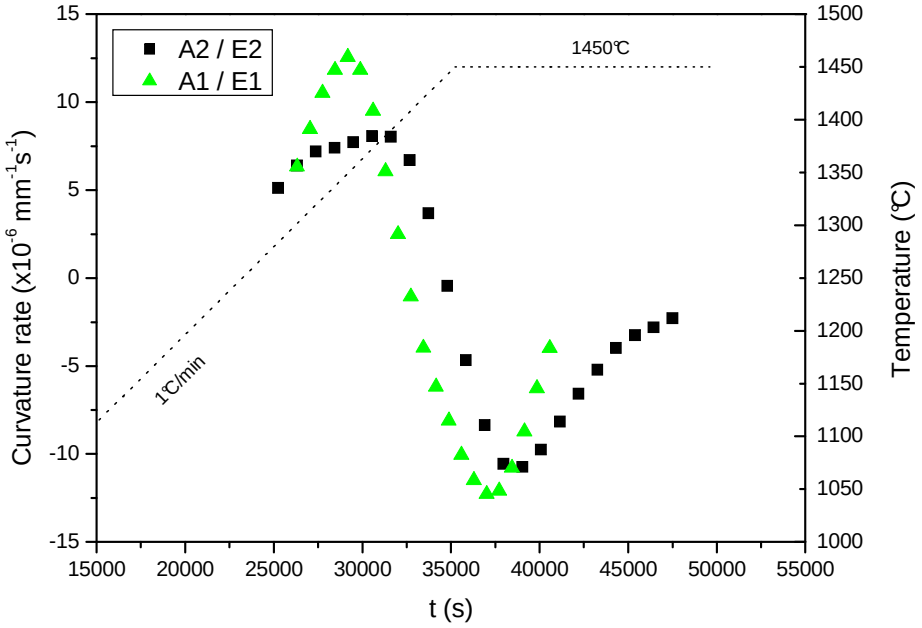

Fig. 49. Curvature rate of samples A1/E1 and A2/E2 as a function of sintering time.

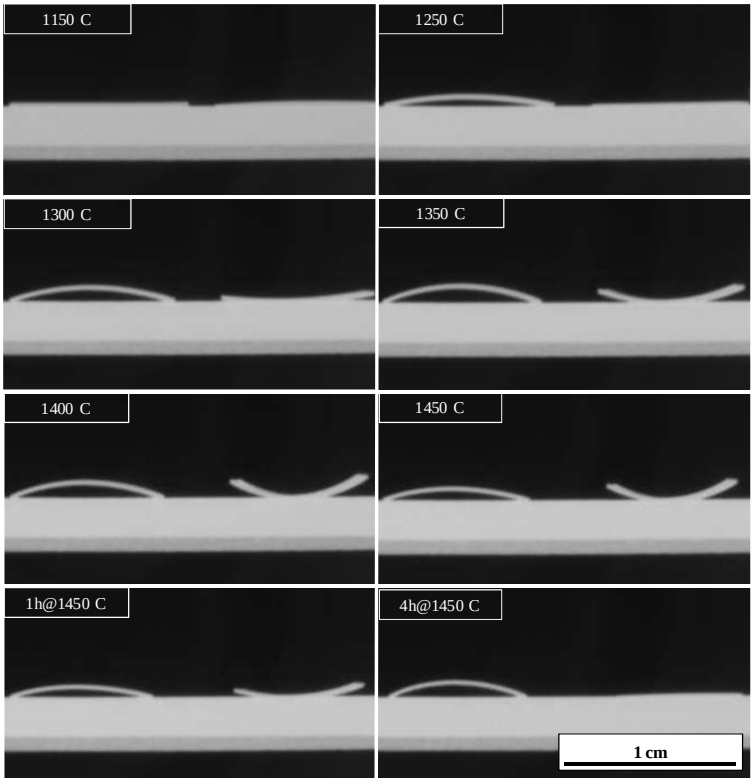

Fig. 50. Selected sequence showing the curvature developed upon co-firing of two half-cells with the same anode and different electrolyte (electrolyte is on the top). Sample A1/E2 (coarse electrolyte powder) left, A1/E1 (fine electrolyte powder) right. The sample on the right is flat at the end of the sintering cycle.

According to the shrinkage rates of the single layers, all samples begin to deform at temperatures above 1150°C; the curvature rate for half cell A1/E1 is positive in the first stage of sintering, while the curvature rate for A1/E2 is negative; the maximum curvature rate for bi-layer A1/E1 is $13 \cdot 10^{-6}$ $mm^{-1}s^{-1}$ and occurs around 1350°C. This sample reaches a maximum curvature of 0.08 mm^{-1}around 1400°C where it inverts the sign of the curvature rate,

being the anode sintering rate higher than the electrolyte one. After an isothermal period of 3 h at 1450°C the half-cell is completely flat and it retains this configuration up to the end of the sintering process.

On the other side, sample A1/E2 starts to bend towards the anode side and never recovers a flat configuration, reaching a final curvature of -0,10 mm^{-1}. One can observe that its curvature rate is always lower than A1/E1, indicating that also the mismatch sintering stresses are lower. It is worth of note that the sole knowledge of the final shrinkage difference between anode and electrolyte does not allow to explain the final curvature of the cell. Though the single components of sample A1/E1 show a strain difference of about 5% (Table 6), half-cell is flat at the end of the cycle, while sample A1/E2 is bent despite its components have a strain difference of only 2%.

Also sample A1/E3 shows an initial negative curvature rate, lower than A1/E2. At around 1350°C the sample is almost flat and then a negative curvature increases again (absolute value). One can also see that the effect of small additions of fine YSZ powders to the coarse electrolyte does only slightly reduce the final curvature (from -0.10 to -0.08 mm^{-1}), by increasing the electrolyte sintering rate in the initial stages of the co-sintering process.

Conversely, sample A2/E2 behaves similarly to A1/E1, showing a high initial positive curvature rate, with a maximum of $7.5 \cdot 10^{-6}$ $mm^{-1}s^{-1}$at 1375°C and a maximum curvature of 0.09mm^{-1} at the beginning of the 1450°C holding time. Therefore, the addition of a small fraction of coarse powder to the anode has a very strong effect on the curvature of the resulting half cell, by slowing down the sintering rate of the anode.

Only bi-layers A1/E1 and A2/E3 recover a flat configuration at the end of the sintering step. Nevertheless, the sole observation of the final curvature

does not give much insight in the behavior of the samples during the intermediate stages of sintering. As one can calculate, both layers can be subjected to a tensile stress. Since for an anode supported half-cell the electrolyte is by far the thinner layer (in our case the anode starting thickness is approximately 27 times larger than the electrolyte one), the most critical case occurs when the curvature rate is positive, *i.e.* the electrolyte is the fastest shrinking layer. This is the case of A1/E1 and A2/E3 cells which however appear flat after firing. Their positive and negative peak curvature rates are higher than samples A1/E2 and A1/E3and cracks due to co-firing are expected to appear in such samples. On the other hand, after a careful SEM observation of the electrolyte surfaces and cross sections, no flaws were found in any sample, and this means that the sintering stress mismatch is not exceeding the intrinsic strength of the green ceramic layers.

Fracture surfaces of some selected sample manually broken are reported in Fig. 51. In all cases the electrolyte shows only internal closed porosity and appears gas tight; on the other side, the anodes retain enough porosity as required to limit concentration losses even before reduction from NiO to Ni. The differences in the starting electrolyte microstructures are no longer recognizable upon sintering.

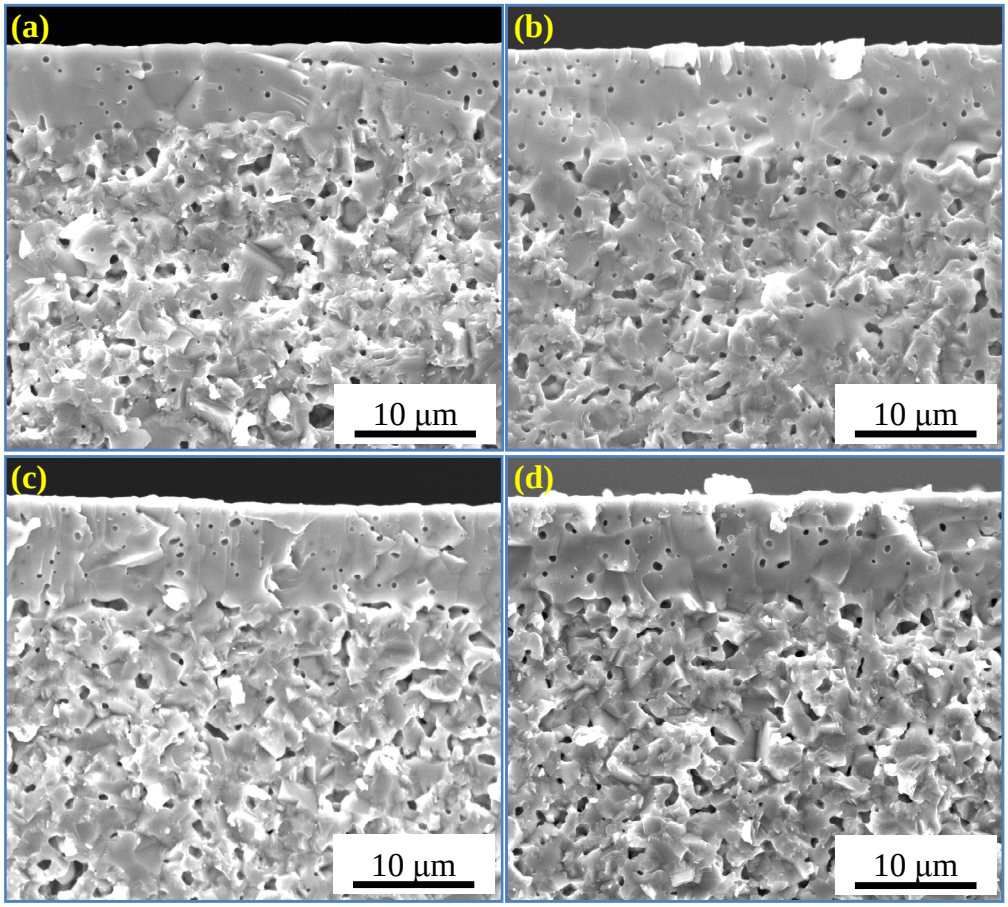

Fig. 51. Cross section of sintered sample A1/E1 (a), A1/E2 (b), A1/E3 (c) and A2/E2 (d). The electrolyte is on the top.

On the basis of the obtained results, A1/E1 combination was considered the optimal one for the manufacturing of anode supported cells. In fact at the end of the sintering cycle it was sufficiently flat to allow screen printing and testing. Polarization curves are reported in Fig. 52. The open circuit voltage (OCV) at 800°C in 3% humidified H_2 is 1075 mV at 700°C, 1068 mV at 750°C and 1060 mV at 800°C, this confirming the gas tightness of the electrolyte and the absence of flaws as suggested by SEM analysis. The

power densities at 0.7 V were 464.1 mW cm^{-2} at 700°C, 609.1 mW cm^{-2} at 750°C and 751.7 mW cm^{-2} at 800°C. High OCV and good performance obtained confirm the suitability of the described manufacturing process for anode supported cells production.

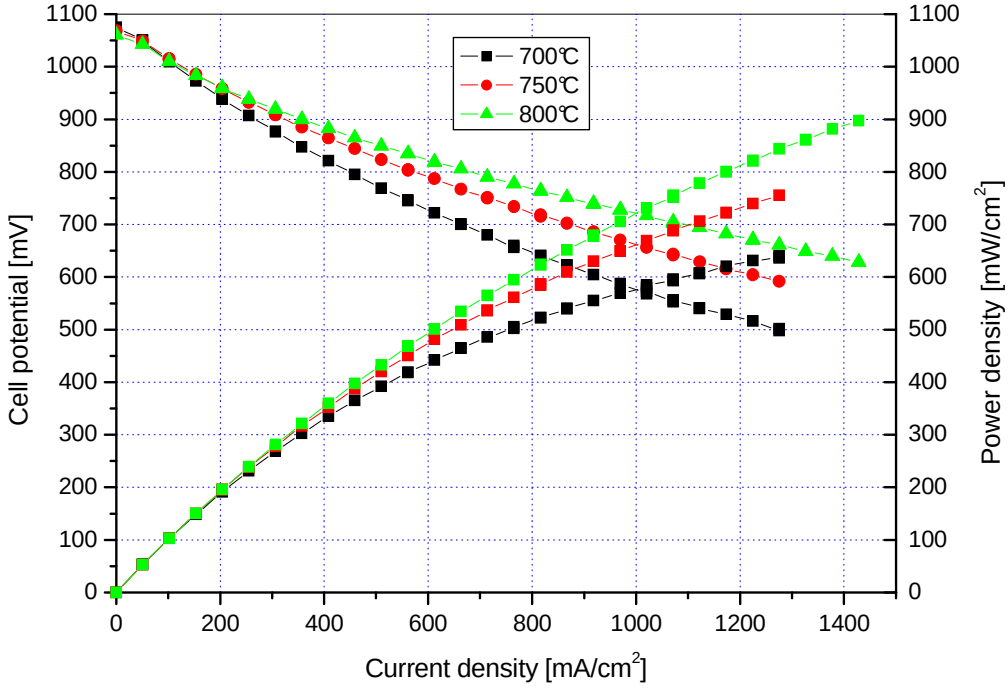

Fig. 52. Polarisation curves of sample A1/E1.

c) Summary

Small changes in the anode or electrolyte starting microstructure have strong effects on the developed curvature. Tailoring the electrolyte composition by adding a fraction of fine powders to coarser powder does not drastically

reduce the residual curvature, but reduces the sintering stresses mismatch during the firing process. On the other side, adding a fraction of coarse powder to the anode has a huge effect on the curvature of the resulting half cell, inverting the sign of the curvature rate. The electrochemical test performed on a flat sintered cell demonstrated the suitability of the process for planar solid oxide fuel cells manufacturing.

Specific mixtures of coarse and fine powders are expected to further reduce the curvature rates, even if the ideal case of a stress free co-sintering is a challenging target for full scale samples.

3.6.3 Effect of NiO powder calcination

a) Material and Methods

Green half cells were prepared as described in the general experimental section. Slurry compositions are reported in Table 7. Fine (d_{50} = 0.3 μm, TZ8-YS, Tosoh, Japan - Ef) and coarse (d_{50} = 0.7 μm, FYT13-002H, Unitec, UK - Ec) 8 mol% yttria stabilised zirconia powders were used for the electrolyte. A mixture of 58 wt% NiO (J. T. Baker, USA, d_{50} < 1 μm) and 42 wt% TZ8-YS was selected for the anode. NiO was used in the form “as received” (Af) or calcined for 10 h at 900°C, ground in a mortar and sieved through a 100 μm mesh (Ac). The dried electrolyte thickness was 10 μm, the anode 370 μm. The specific surface area (SSA) for the as received and

calcined NiO was determined by nitrogen adsorption (BET) method (ASAP 2010, Micromeritics, USA).

An LSM/YSZ cathode was screen printed on selected samples and electrochemical tests were performed as described in the general experimental section.

Table 7. Slurry composition (wt%).

	Electrolyte	Anode
Powder	69	61
Dispersant	3	4
Water	16	10
Binder	12	25

a) Results and discussion

SEM micrographs of the selected powders are reported in Fig. 53. Some differences appear clear. As received NiO (Fig. 53a) is strongly agglomerated and appears much finer compared to calcined NiO (Fig. 53b). The measured specific surface area is 3.3 m^2/g for the first, 1.6 m^2/g for the latter; the thermal treatment at 900°C is therefore significantly decreasing the specific surface area. Coarse YSZ particles (Fig. 53c) possess an irregular shape, while fine YSZ particles (Fig. Fig. 53d) are more regular and round shaped, being produced by a chemical route.

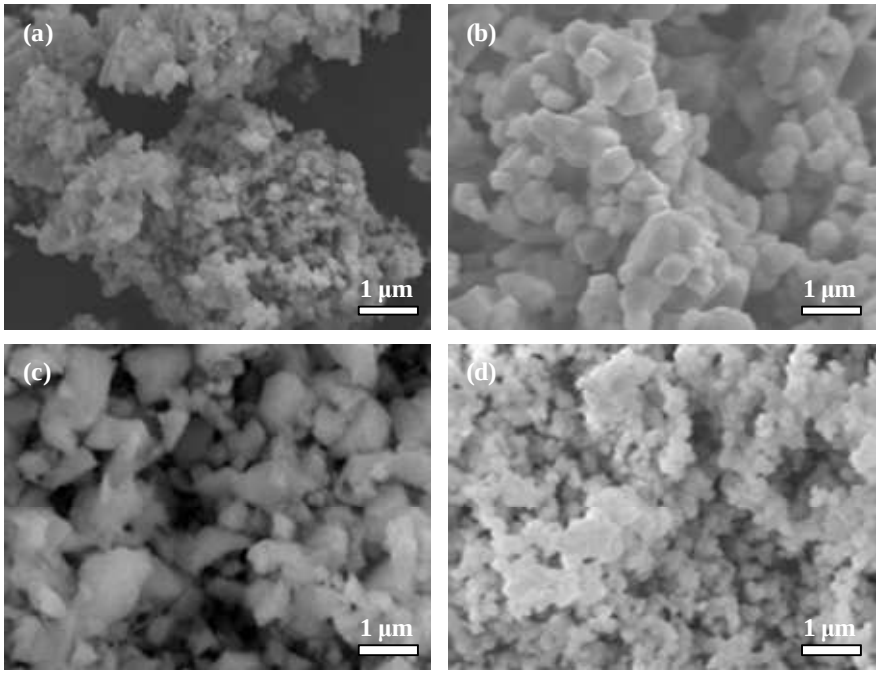

Fig. 53. SEM micrograph of the selected powders. NiO (a), calcined NiO (b), coarse YSZ (c), fine YSZ (d).

True free strain (ε) and strain rate (dε/dt), are reported in Fig. 54 and Fig. 55, respectively. Electrolyte Ef is sintering at lower temperatures and with higher sintering rates compared to Ec. Comparing Ac and Af anodes, the first possesses a lower sintering rate. The coarsening treatment on NiO powders has therefore the effect of significantly diminishing the sintering rate. Comparing anodes and electrolytes sintering rates, the most critical combination with the highest mismatch in the sintering rate is Ac with Ef (0.64×10^{-3} min^{-1} at 1380°C, where Ec shows a linear shrinkage of 14% and Af of 7%, only); conversely, the best combination is Ac with Ec, the sintering rate mismatch being always lower than 0.1×10^{-3} min^{-1} over all the temperature range.

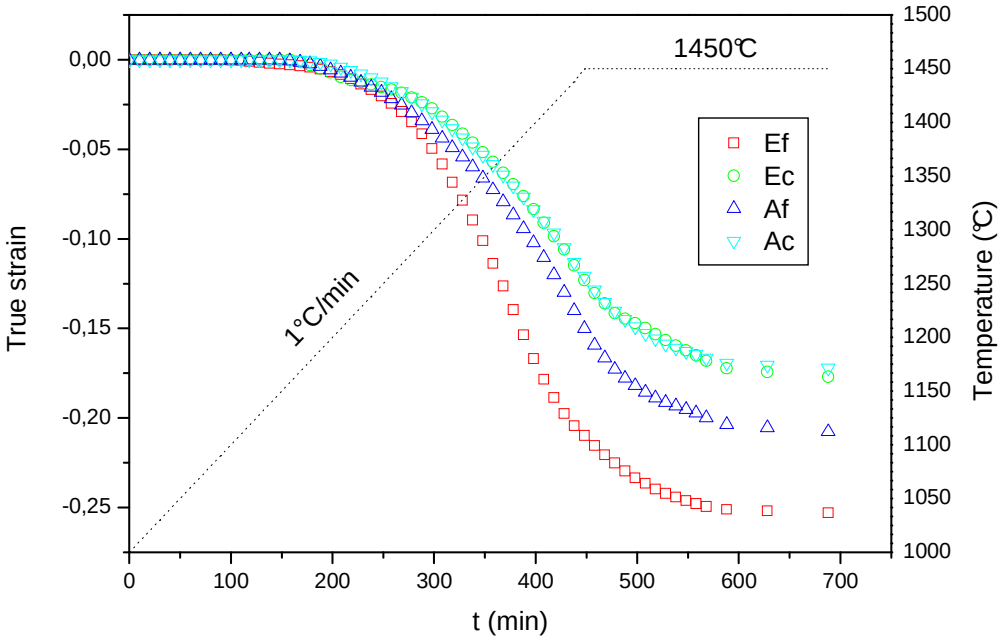

Fig. 54. True strains as a function of time for tapes Ef, Ec, Af and Ac.

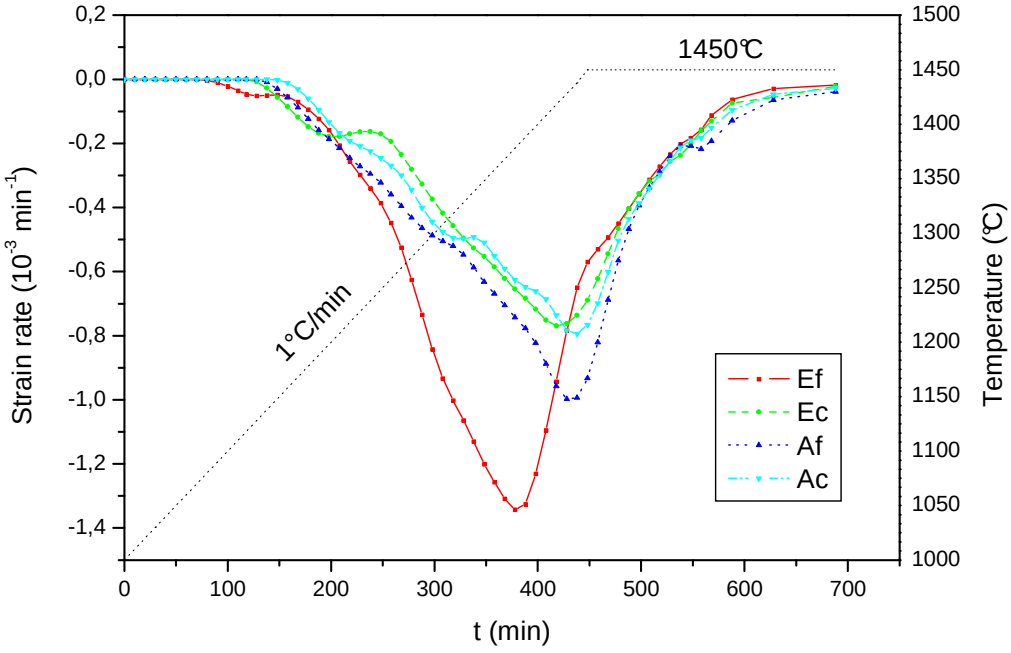

Fig. 55. Strain rate as a function of time for tapes Ef, Ec, Af and Ac.

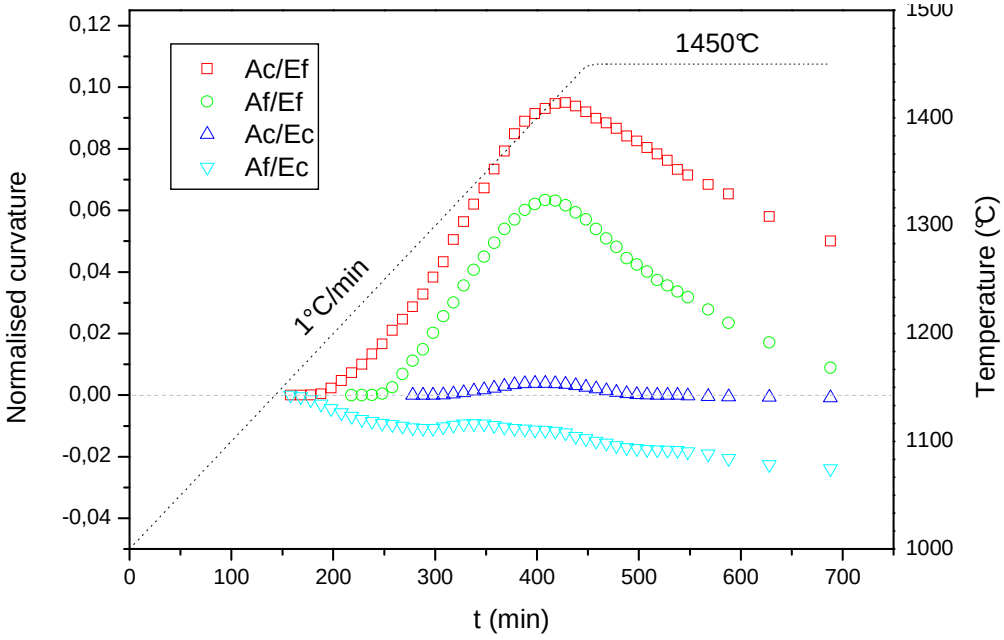

Fig. 56. Normalised curvature as a function of time for the produced cells.

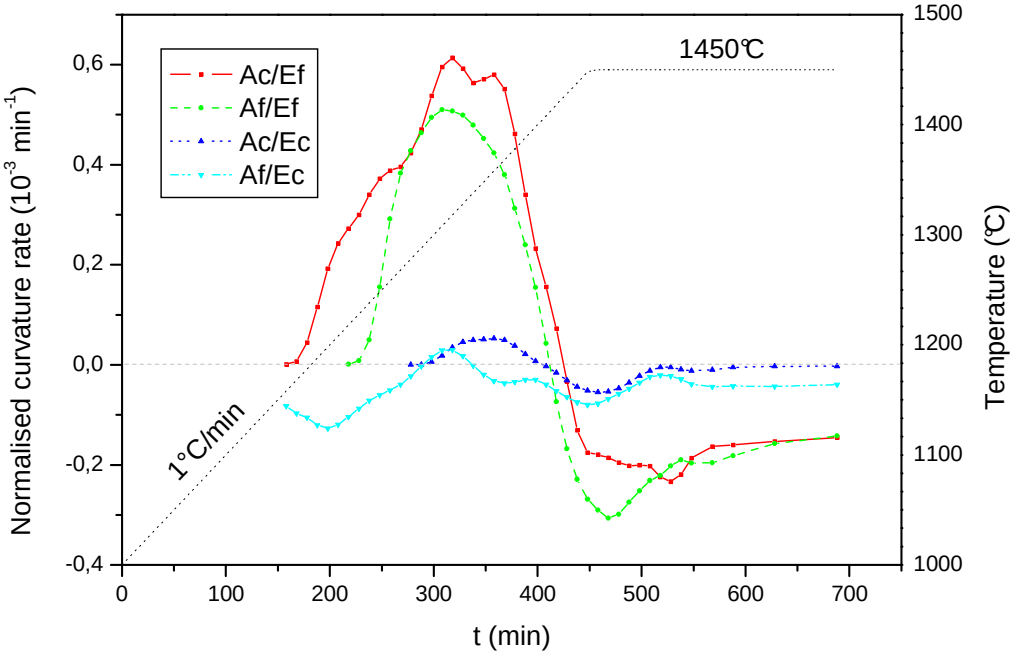

Fig. 57. Normalised curvature rate as a function of time for the produced cells.

The developed normalized curvature k = t/r (t being the bi-layer thickness and r the radius of curvature) and the cells curvature rate are reported in Fig. 56 and Fig. 57, respectively. Both samples in which electrolyte Ef is used (Ac/Ef and Af/Ef) are bending towards the electrolyte side (positive curvature rate) in the first stages of sintering, as the electrolyte shrinks faster than the anode. The normalized curvature is reaching a maximum value (0.095 for Ac/Ef and 0.063 for Af/Ef) after which the curvature rate is inverting its sign. Sample Af/Ef is recovering an almost flat configuration at the end of the sintering process, while Ac/Ef remains strongly curved. The temperatures of curvature rate inversion, which corresponds to a point of zero mismatch stress, relate with a fairly good approximation to the point where the anode free sintering rate equals the electrolyte free sintering rate, both being in the range 1410°C - 1430°C.

On the other hand, sample Af/Ec is bending towards the anode side (negative curvature rate) in the firsts stages of sintering. The normalized curvature remains always negative and is maximal at the end of the sintering (-0.024). Only sample Ac/Ec possesses always a very low curvature rate and remains fairly flat over all the temperature range, being noticeably flat at the end of the sintering.

As it was discussed previously, a positive curvature rate is the most critical condition for anode supported cell sintering process, since the thin electrolyte is subjected to tensile stresses, which retard densification, especially in the firsts stage of sintering, where ceramics possess still a limited strength and stresses may induce crack nucleation and propagation. A negative curvature rate is less critical, the electrolyte being under compression. As a consequence, the most critical sample is Ac/Ef, showing the maximum normalized curvature rate of 0.6×10^{-3}, followed by Af/Ec

(dk/dt_{max} = 0.5 x 10^{-3}). Af/Ec and Ac/Ec possess always a negligible positive curvature rate, one order of magnitude less than the maximum showed by Ac/Ef. Only Ac/Ec has always a very low positive or negative curvature rate, approximating very well the ideal conditions of a completely stress free co-sintering. The curvature trend of the half-cells is in very good agreement with the monolithic layers free sintering data: the cell built with the anode and electrolyte possessing the highest mismatch sintering rate (Ac and Ef) is the one showing the highest curvature rate, while the sample realized with Ac and Ec (mismatch sintering rate always lower than 0.1 x $10^{-3}$$min^{-1}$) is almost flat over all the temperature range. The coarsening treatment on the NiO powders, by reducing the anode sintering rate, has a detrimental effect on the half-cell built using the fine electrolyte, while it is highly beneficial when the coarse electrolyte is used in the half-cell production, resulting in a virtually unconstrained sintering.

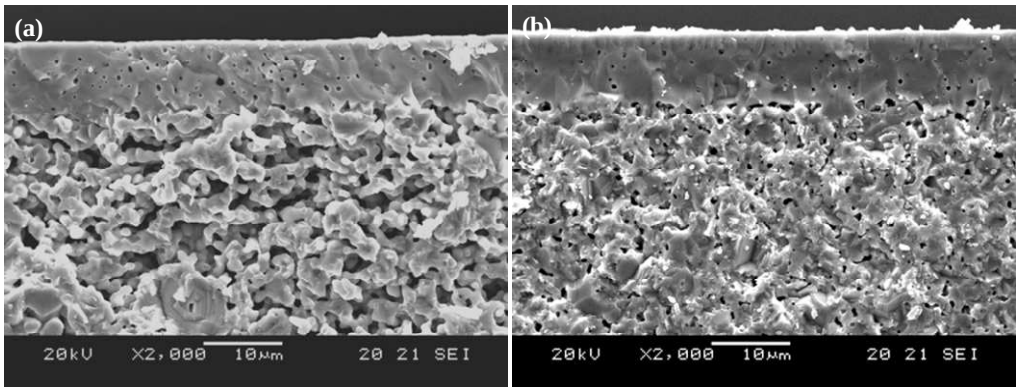

Fig. 58. Cross section of the as sintered cells. Ac/Ec (a) and Af/Ec (b).

The cross section of as sintered Ac/Ec and Af/Ec samples is reported in Fig. 58. The electrolyte is retaining limited porosity, which is however not

interconnected. No signs of delamination are observed. Anode Ac has clearly higher porosity compared to Af. The electrolyte surface of selected samples is shown in Fig. 59. The electrolyte of Af/Ec and Ac/Ec (Fig. 59a) is well densified and no cracks are visible at a careful examination. On the other hand, flaws of tenths of micrometers in length and a few micrometers in width are clearly present on the electrolyte of Af/Ef (Fig. 59b). Crack of few hundreds micrometers in length and tenths of micrometers in width are present on Ac/Ef (Fig. Fig. 59c and Fig. 59d) and are even visible at naked eye.

It is interesting to note that Ac/Ef, which possesses the highest mismatch in free strain rate between anode and electrolyte (Fig. 55), is developing the highest mismatch sintering stresses, which is leading to the development of the highest curvature rate (Fig. 57), crack extension and crack density (Fig. 59c and Fig. 59d). The only samples which are not showing any sintering defects are those showing negative or very limited curvature rate in the initial stages of sintering (anode sintering faster than electrolyte, like in Af/Ec, or anode sintering with the same rate as the electrolyte, like in Ac/Ec). It is worth nothing that for sample Ac/Ec, the anode and electrolyte sintering rate is so well matched, that the resulting half-cell is almost flat during the whole sintering cycle (Fig. 56), and perfectly flat at the end of the process. The very low curvature rate, which is observed in the intermediate stages of sintering (Fig. 57) is a clear indication of the very low stresses mismatch as generated upon sintering. This is a double advantage: first, a flaw free electrolyte and a perfect adhesion between anode and electrolyte can be obtained, as demonstrated by SEM micrographs; second, it allows the direct production of flat SOFCs without any creep flattening step, eliminating all the inherent disadvantages of such process.

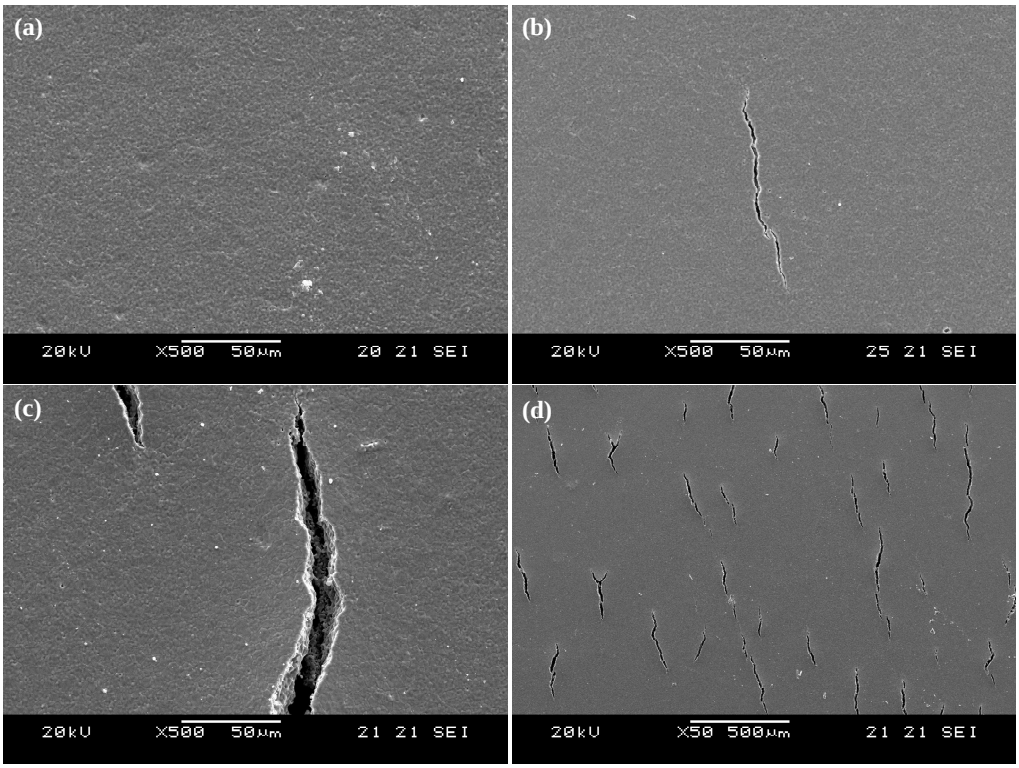

Fig. 59. Electrolyte surface of the as sintered cells. Ac/Ec (a), Af/Ef (b), Ac/Ef (c), Ac/Ef at a lower magnification (d).

By observing Fig. 7 it is clear that Af/Ef and Ac/Ef are not suitable for fuel cells production, since the cracks in the electrolyte would lead to fuel and oxygen mixing, while Af/Ac shows a pronounced curvature for being used without an additional flattening step; for these reasons, an electrochemical test was performed on Ac/Ec only. The data are plotted in Fig. 8.

The power densities at 0.7V at 750°C, 800°C and 850°C are 0.40, 0.49 and 0.62 Wcm^{-2}, respectively. Such performances, although lower than usually measured with samples under the same condition, have to be interpreted by noting that the anode microstructure was not optimized for electrochemical performance maximization. A thin denser anode functional layer (*e. g.* with

the same composition of Af) may be easily inserted between the anode and the electrolyte in order to enhance the triple phase boundaries and the electrochemical performances, without varying the presented procedure and analysis.

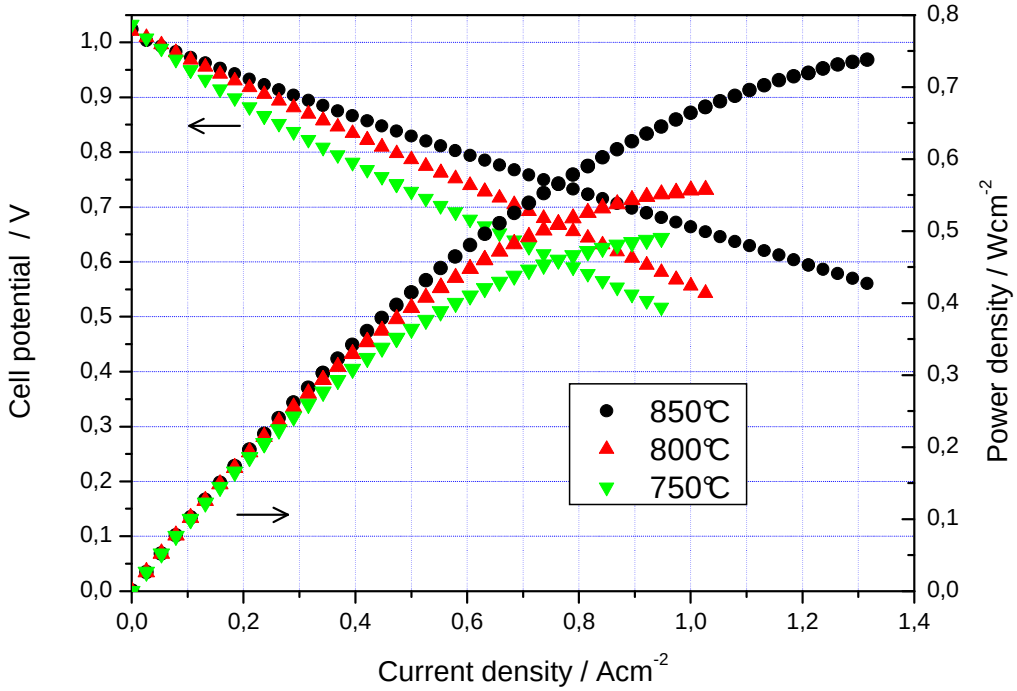

Fig. 60. Electrochemical test of sample AcEc.

b) Summary

An almost perfect matching of anode and electrolyte sintering rates was obtained, resulting in a virtually unconstrained co-sintering and a cell which do not develop any significant curvature during the whole firing process,

thus demonstrating the feasibility of a straightforward anode supported half-cell production. SEM micrographs demonstrated the absence of defects in the samples possessing low sintering rate mismatch between the constituting layers, while when the sintering rate mismatch is high, severely damaged microstructures are developed.

The calcinations of the NiO powder reduced significantly the sinter-activity of the green anode, and matched its sintering curve with the electrolyte one. However the developed anodic microstructure in the proximity of the electrolyte was too coarse, and the electrochemical performances were affected.

3.6.4 Conclusions

Anode supported green half cells were obtained by a sequential tape casting method.

The influence of different parameter on the sintering kinetics and on the developed curvature was studied. Heating rate, powder size, powder calcinations, type and level of doping elements were considered. The curvature developed upon co-firing was monitored during the whole sintering process, this allowing the direct determination of the best condition to get a flat cell without any additional creep flattening. The estimation of the curvature rate allowed some qualitative insight on the developed internal stresses that are the reason for cell failure. The crack development and the crack extensions could be related to the magnitude of the curvature rate.

Cracks were found only in samples where the electrolyte was sintering under a tensile stress.

A slow heating rate was found to be beneficial for limiting the developed curvature. As far as the doping elements are concerned, Al is shown to increase the anode sintering rate and Ce to reduce it. The use of reactive elements, if carefully controlled, can be successfully employed to tailor the anode sintering curves. Small changes in the anode or electrolyte starting powder sizes have strong effects on the developed curvature, and specific mixtures of coarse and fine powders can reduce the curvature rates. By further optimizing the green compositions and calcining the NiO powders, an almost perfect matching of anode and electrolyte sintering rates was obtained, resulting in a virtually unconstrained co-sintering. A cell which did not develop any significant curvature during the whole firing process was developed, thus demonstrating the feasibility of a straightforward anode supported half-cell production. Microstructural observation and electrochemical tests confirmed the absence of defects in the cells produced with the tailored starting microstructure.

3.7 Vertical sintering to measure the uniaxial viscosity of thin layers

3.7.1 Theoretical background

In order to being able to calculate the developed curvature rate and the stresses acting on a multilayer during sintering, which are responsible for deformation an flaws propagation, the knowledge of the viscous material parameters is needed (see Chapter 2). In case of a bi-layer with a beam geometry, the knowledge of viscous Poisson ratio is not required. The only material parameter needed is the uniaxial viscosity. Once the uniaxial viscosity as a function of the green density is known, *Eq. 2-12* can be applied and the curvature rate can be calculated if the layers thicknesses and the layers free sintering rates are known.

Nevertheless, the measure of viscous parameters is not an easy task. The available analysis techniques for measuring uniaxial viscosity are not easily applicable to the direct measurement of the viscosity of thin tape cast layers. The analyzed samples have to be massive and possess specific geometry (*e.g.* for sinter forging, the height/diameter ratio should be larger than 1.5) (73). Thin tape cast layers may not be easily measured. Pressed pellets or several tape cast layers, which are laminated together have to be used. As it is known, this further processing of the tape will result in a different (denser) green microstructure. The measured mechanical parameters will

therefore be those of the processed samples, not of the intended original thin tape cast layer.

In this section we will introduce a novel method for measuring the uniaxial viscosity of a green body during sintering. This approach is based on the application of a very low tensile stress to the green body. The uniaxial viscosity is derived from two separate sintering experiments: in the first the shrinkage rate of a green layer which is sintered hanging on a rod (and thus subjected to its own weight) is measured with an optical method; in the second experiment the shrinkage rate of an identical sample which is sintering in a load-free configuration is measured. The viscosity for an YSZ electrolyte and an NiO/YSZ anode was experimentally determined following such novel method. This data were then used in *Eq. 2-12* in order to determine which would be the developed curvature rate of a cell constituted from the considered layers. Such cell was eventually built, and the curvature rate was experimentally measured, in order to compare the result with the predicted curvature rate, and evaluate the consistency of the measured uniaxial viscosity.

It has been shown that a porous body undergoing densification can be treated as linear viscous at stresses below 1 MPa. For such materials it is expected that the creep rates in slight uniaxial tension or uniaxial compression are the same (79), (91). The approach we developed for determining uniaxial viscosity is based on the same equation which is valid for the well known loading dilatometry and sinter forging methods (154):

$$\eta = \frac{\sigma_1}{\dot{\varepsilon}_1 - \dot{\varepsilon}_{f1}} \qquad \text{Eq 3-1}$$

Where η is the uniaxial viscosity, σ_1 the uniaxial load applied to the green body, $d\varepsilon_1/dt$ is the observed strain rate, and $d\varepsilon_{f1}/dt$, is the strain rate which would be observed in case of free sintering. If a tensile load is applied to the sintering body, it's effect will be to reduce the effective sintering stress and the observed strain rate will be reduced. A similar concept was employed by Cheng and Raj. They measured the sintering pressure in ceramic films as the external load required to have zero axial strain rate (74). In the following description the applied tensile stress is very low, much smaller than the assumed intrinsic sintering stress. It is believed that a low stress is not inducing anisotropy in the material microstructure and thus it can be applied continuously from the beginning of the sintering to the end. In the experimental method we developed, the small load is provided only by the own weight of the green tape, as described below.

3.7.2 Materials and methods

Anode and electrolyte layers with a thickness of approximately 200 µm were produced by tape casting as described in the general experimental section. The ceramic powders consisted of YSZ (FYT13-002H) in the electrolyte and 58 wt% NiO (J.T. Baker) - 42 wt% YSZ (TZ8-YS, Tosoh) in the anode. Tapes were cut in half dog-bone shape with a sharp blade. The initial dimension of the rectangular area of the sample was 20 x 5 mm^2. In Fig. 61 we report a sample picture of an anode layer which is sintering hanged at 1200°C, for clarifying the set-up. The sintering schedule was

1°C/min to 600°C, 5°C/min to 1450°C and 4h isotherm. Three half cells were produced by sequential casting with different thicknesses. The green electrolyte thickness of the three samples was 12 µm, the anode thickness was 180, 278 or 408. The curvature developed upon sintering was observed as described in the general experimental section. A positive curvature refers to a cell with the anode on the concave side.

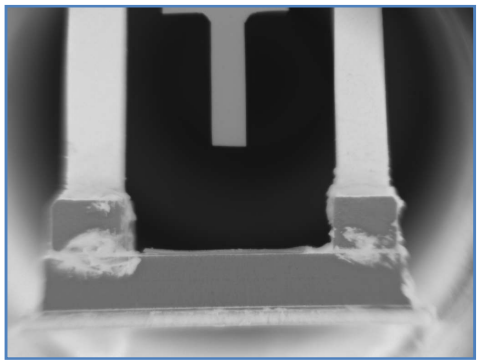

Fig. 61. Sample picture of a thin tape cast NiO/YSZ powder compact sintered hanged on a rod. The furnace temperature is 1200°C.

In the set-up which was specifically designed, the thin ceramic layer is hanging from a support made from a Si_2Mo rod. The coupling between ceramic and support rod is done by wrapping the flexible green tape cast layer around the rod. The green tape has a half dog-bone geometry (Fig. 62). The length of the rectangular section of the sample is measured from pictures which are acquired upon all the sintering cycle. The imaging acquisition process was described in the general experimental section.

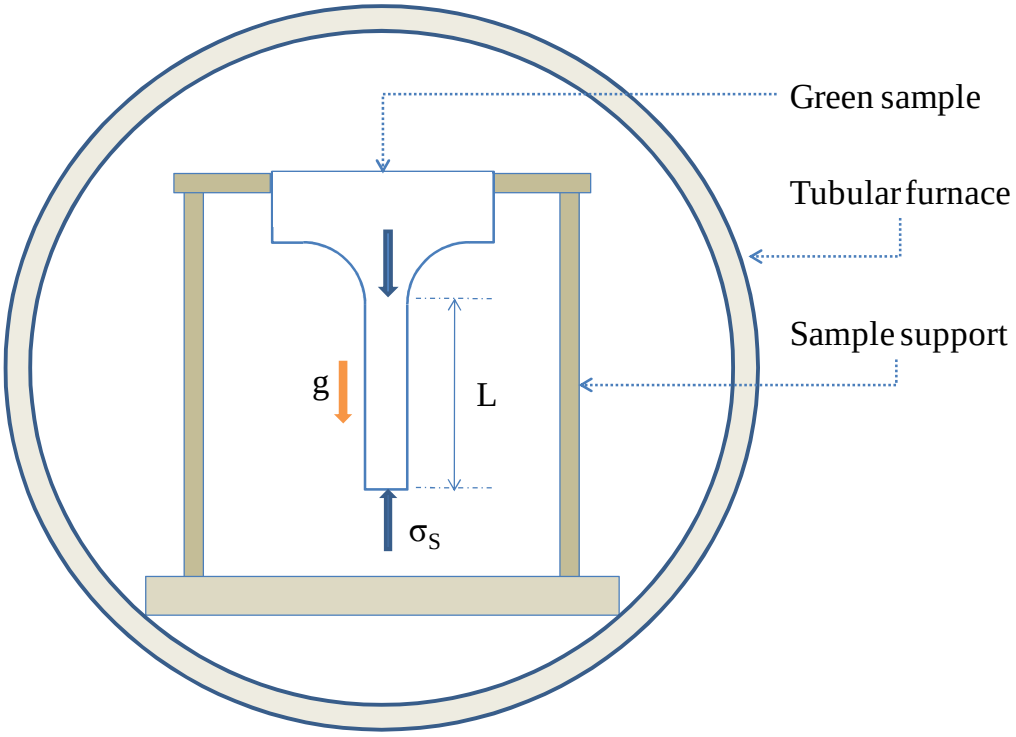

Fig. 62.Set-up for the vertical sintering experiment.

3.7.3 Data analysis

The elastic solution for a beam which is hanging freely and is therefore subjected to its own weight only, can be easily derived as (155):

$$L - L_0 = \frac{\rho g L_0^2}{2E} \qquad \textit{Eq. 3-2}$$

where L_0 is the initial beam length, L the final length, ρ the material density, g the gravity constant and E the Young's modulus. The total elongation of

the beam is thus the same as if a concentrated load equal to half the weight of the beam was applied. As discussed in the introduction, the response to a stress of a porous ceramic material, which is sintering can be considered as linear viscous. It follows that the elastic-viscous analogy can be applied, *i.e.* the Young's modulus can be replaced by the uniaxial viscosity η, while the strain can be replaced by the strain rate $\dot{\varepsilon}$. Applying this analogy, and considering the sintering stress σ_s as well, it follows:

$$\frac{L-L_0}{L} = \frac{\rho g L_0}{2E} + \frac{\sigma_s}{E} \qquad Eq\ 3\text{-}3$$

and since

$$\sigma_s = \eta \dot{\varepsilon}_f \qquad Eq.\ 3\text{-}4$$

it follows:

$$\eta = \frac{\rho g L_0}{2(\dot{\varepsilon} - \dot{\varepsilon}_f)} \qquad Eq\ 3\text{-}5$$

The uniaxial viscosity of a ceramic beam can be therefore determined from two experiments: in the first the free sintering rate of the ceramic compact is determined by sintering it on an horizontal support, then it is determined the sintering rate of a sample with the same characteristics which is sintering hanged.

3.7.4 Viscosity of NiO/YSZ anode

The strain of the anode sintered freely and sintered hanged is reported in Fig. 63 and the correspondingly strain rate is reported in Fig. 64. It is very interesting to note that, while the free sintered sample is beginning to shrink in the first stages of sintering, the sample which is sintering as hanged is increasing its length as a consequence of its own weight. The strain rate is first positive, then it becomes negative. The strain rate curve of the sample subjected to the low tensile load is always above the one of the free sintered sample, up to a time of around 1 h at 1450°C, after which the two samples shrink with similar rates. This is consistent with the fact that a very small load is applied. It can also be considered a proof that this load is not influencing the microstructure dramatically: the low applied load is affecting the sintering rate only when the ceramic compact possesses very low density and creep resistance. As sintering proceeds and density increases, more necks are formed and the small load is ineffective in producing observable differences in strain rate. The stressed sample microstructure is therefore not retaining a “memory” of the applied load.

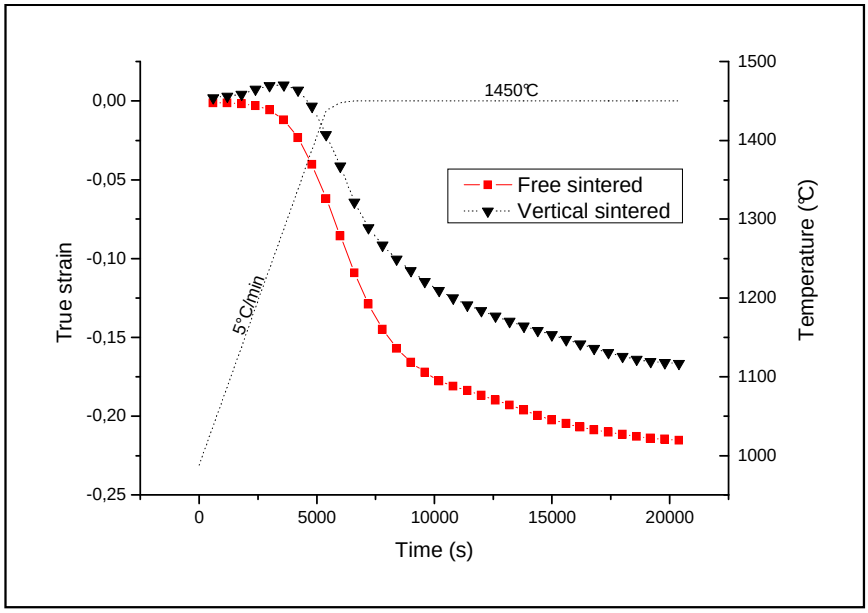

Fig. 63. Sintering strain (NiO/YSZ). Comparison of a free sintered sample with a sample sintered hanged.

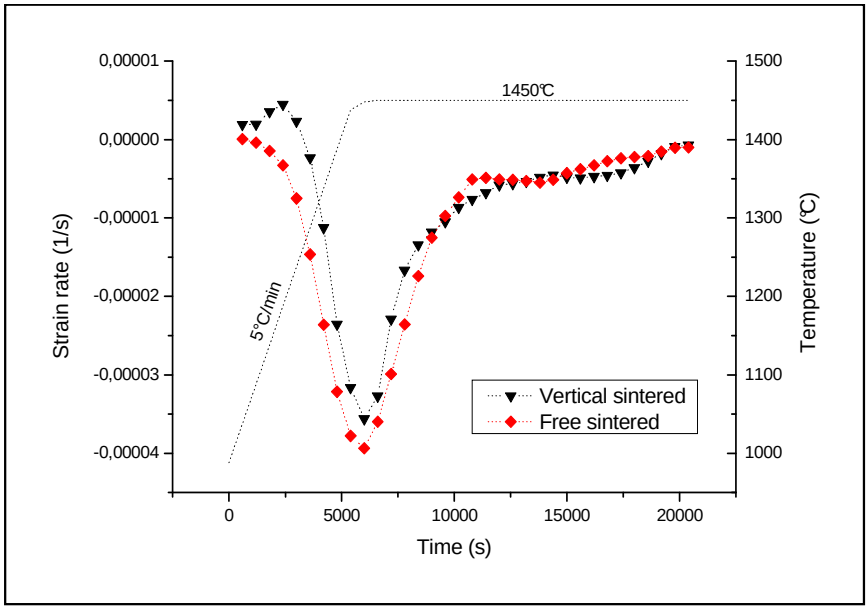

Fig. 64. Strain rate (NiO/YSZ). Comparison of a free sintered sample with a sample sintered hanged.

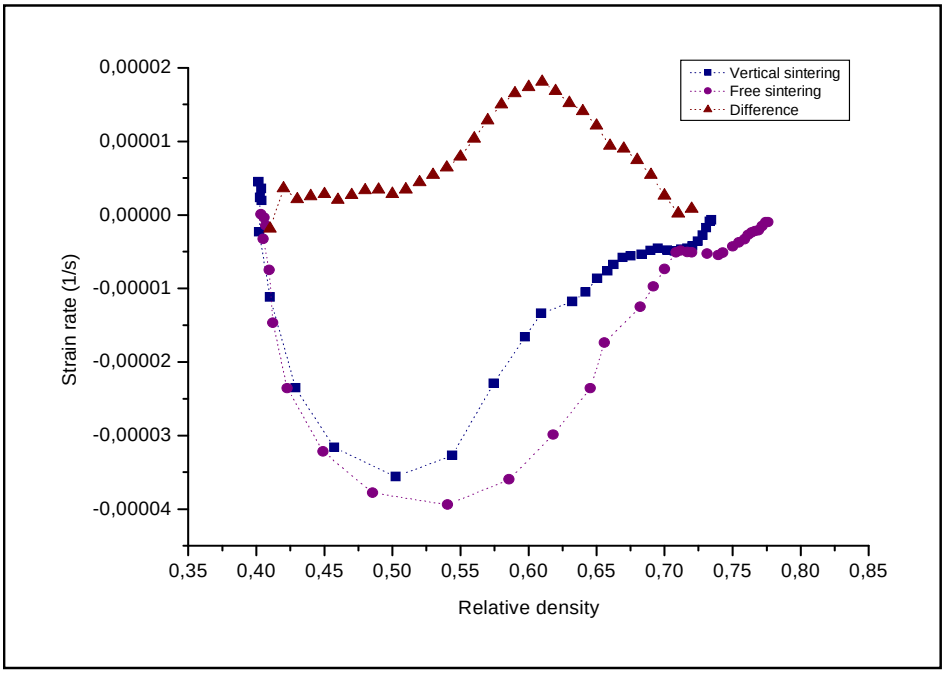

Fig. 65. Strain rate over relative density (NiO/YSZ) of the free sintered sample, the sample sintered hanged and their differences.

The strain rate is plotted in Fig. 65 as a function of the relative density. The relative density is calculated under the hypothesis the sintering of the load free sample is isotropic, and the strain in the directions which are un-loaded is the same as the load free configuration. The measured strain rate in the width direction of the sample sintered hanged was in fact very close to the one of the free sintered sample. The sintering rate in the thickness dimension couldn't be measured (the thickness is only 0.2 mm), but it is assumed to be the same as the width direction. The relative densities are derived from the following equations:

$$\rho_{vertical}\,(t) = \frac{\rho_0}{e^{(2\varepsilon_{free}+\varepsilon_{vertical})}} \qquad \textit{Eq. 3-6}$$

and

$$\rho_{free}\,(t) = \frac{\rho_0}{e^{(3\varepsilon_{free})}} \qquad \textit{Eq. 3-7}$$

The uniaxial viscosity of the NiO/YSZ compact as a function of the relative density, calculated from the stress over the difference of the strain rate at the same density, is plotted in Fig. 66.

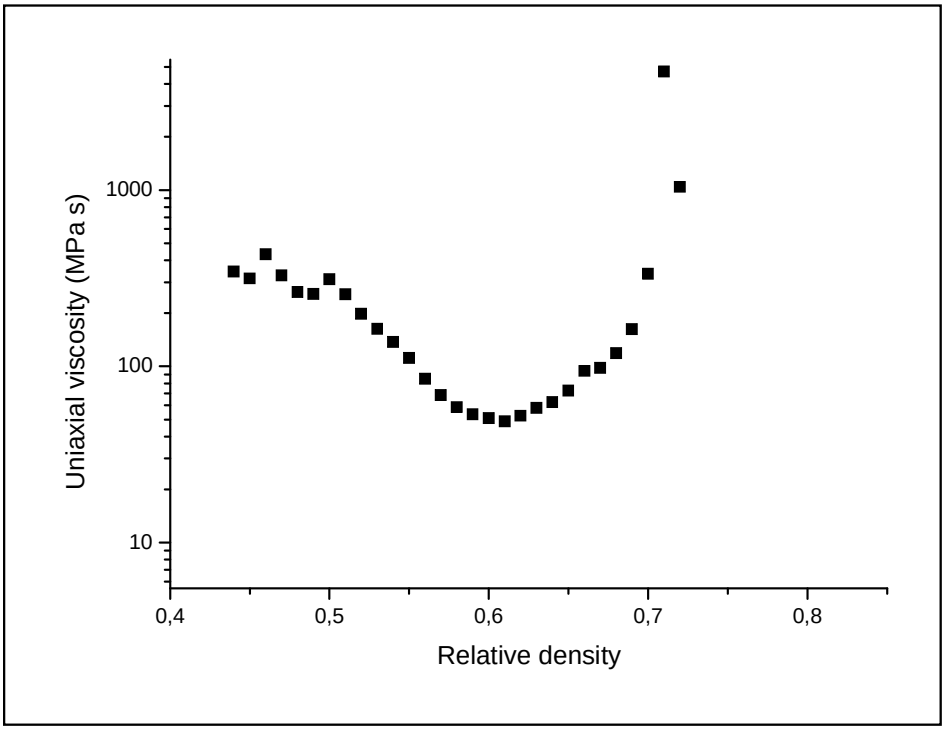

Fig. 66. Uniaxial viscosity (NO/YSZ).

The trend in the viscosity is consistent with the expectations. At low temperature and low density the viscosity is high; then it decreases because of the increasing temperature. As the sample densifies the viscosity increases again. The graph is limited to the zones where the viscosity can be effectively calculated. The viscosity at high density is not calculable with this method, since the very low applied load is not giving any appreciable difference in the strain rate. The viscosity is in fact proportional to the applied stress over the difference in the strain rate between the loaded sample and the load free sample. When this difference goes to zero, *i.e.* at very high viscosities (low temperature or high density), the error becomes high.

3.7.5 Viscosity of YSZ electrolyte

The viscosity of the electrolyte was calculated following the same procedure employed for the anode. The strain of the electrolyte sintered freely and sintered hanged is reported in Fig. 67 and the correspondingly strain rate is reported in Fig. 68. The strain rate as a function of the relative density is plotted in Fig. 69. The uniaxial viscosity of the YSZ compact as a function of the relative density is plotted in Fig. 70. The same considerations are valid as in the case of the anode. The uniaxial viscosity is calculable only in the intermediate stages of sintering up to a maximum relative density of 0.85.

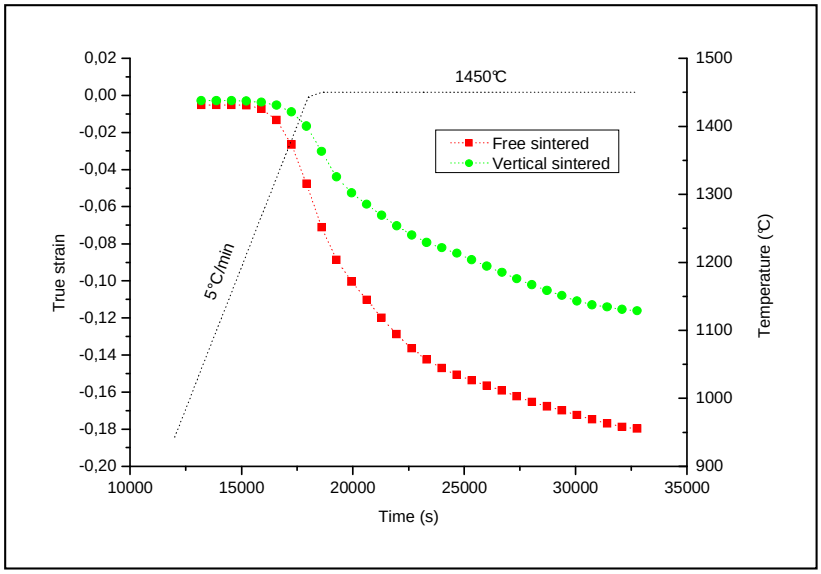

Fig. 67. Sintering strain (YSZ). Comparison of a free sintered sample with a sample sintered hanged.

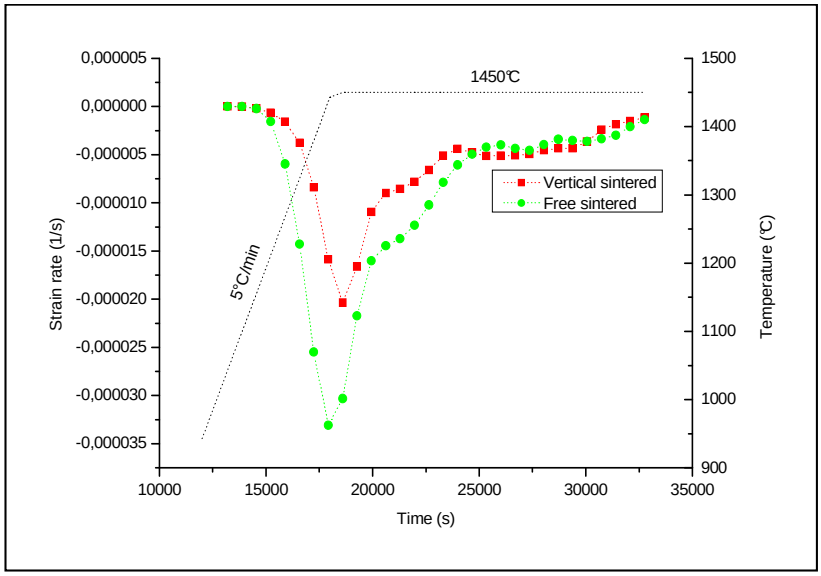

Fig. 68. Strain rate (YSZ). Comparison of a free sintered sample with a sample sintered hanged.

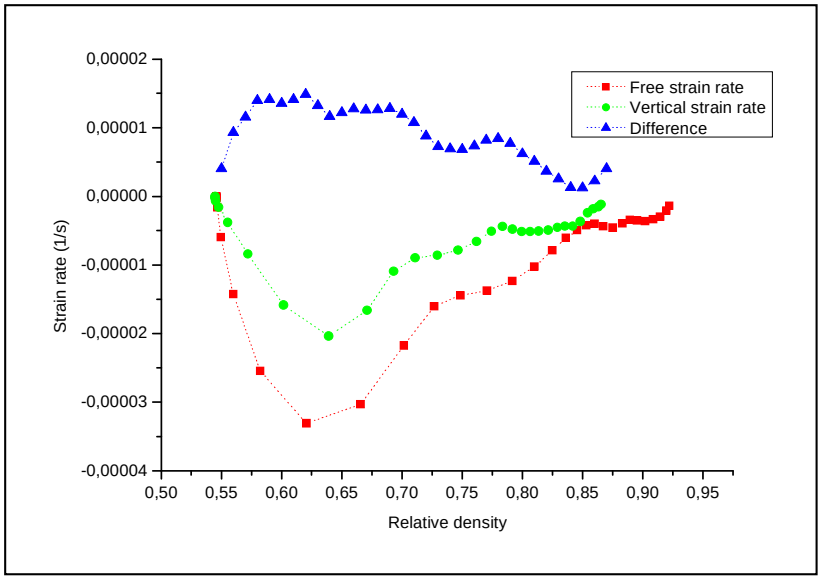

Fig. 69. Strain rate over relative density (YSZ) of the free sintered sample, the sample sintered hanged and their differences.

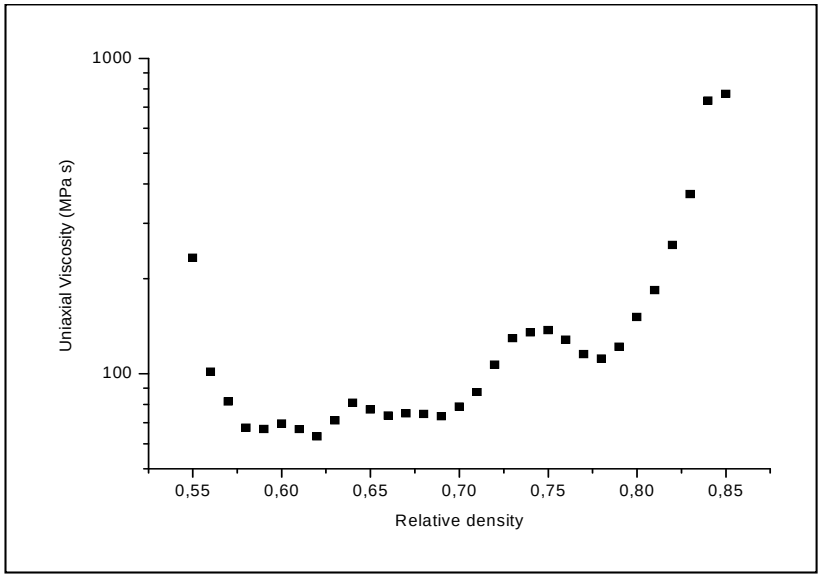

Fig. 70. Uniaxial viscosity (YSZ).

3.7.6 Cell curvature rate

The viscosity of the layers and their free sintering rates were used for calculation the cell normalized curvature rate accordingly to *Eq. 2-12*, which is reported here for convenience:

$$\dot{k} = \frac{t_1+t_2}{r} = \frac{6(m+1)^2 mn}{m^4n^2 + 2mn(2m^2+3m+2)+1}\,\Delta\dot{\varepsilon} \qquad \text{Eq. 3-8}$$

The thickness ratio $m=t_1/t_2$ can be calculated with the following relation:

$$t_i = t_0 e^{\varepsilon_{i,free}} \qquad \text{Eq. 3-9}$$

were i = 1 or 2. The calculated curvature rate for the three cell thicknesses is reported in Fig. 71. In all the three cases the curvature rate is positive in the first stage of sintering (the cells are curving towards the anode side) and reaches a peak at around 1380°C, after which its magnitude is quickly decreasing. The cell possessing the highest peak in the curvature rate is that produced with the thinner anode.

The in situ experimentally measured curvature rate for the three samples with different anode thicknesses is plotted in Fig. 72. The direct comparison between the calculated data and the experimental data for each sample thickness is given in Fig. 73.

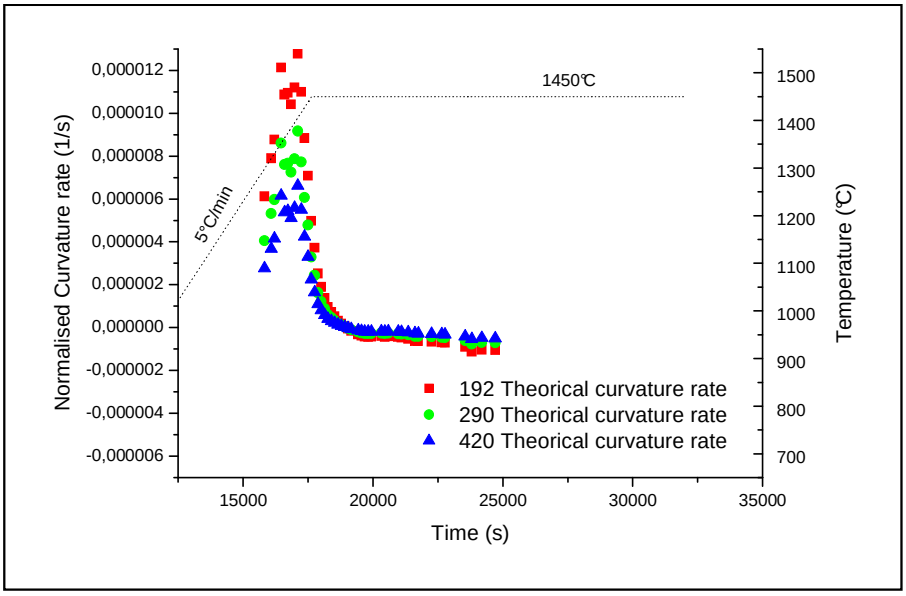

Fig. 71. Normalized curvature rate, calculated for three anode thicknesses.

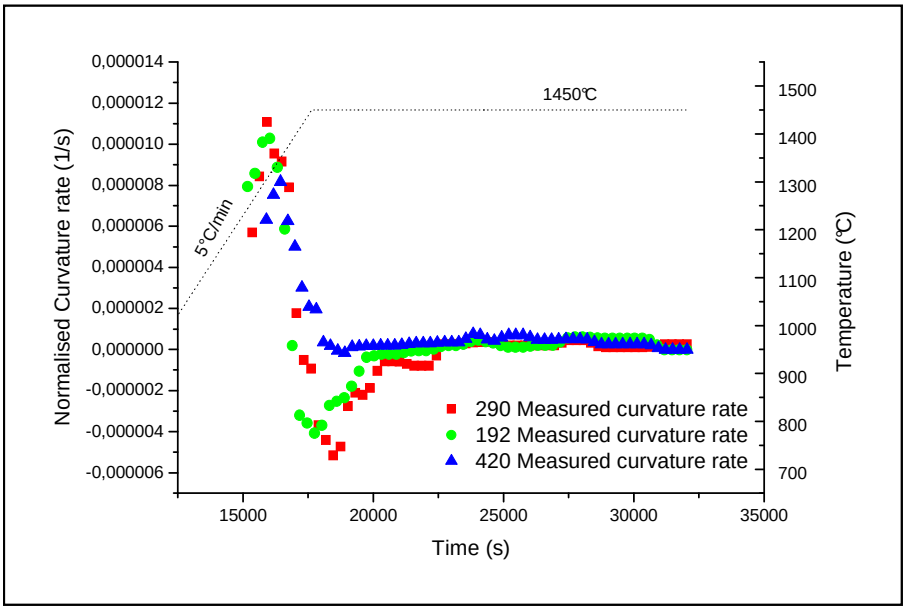

Fig. 72. Normalized curvature rate, experimentally measured on three samples with different anode thicknesses.

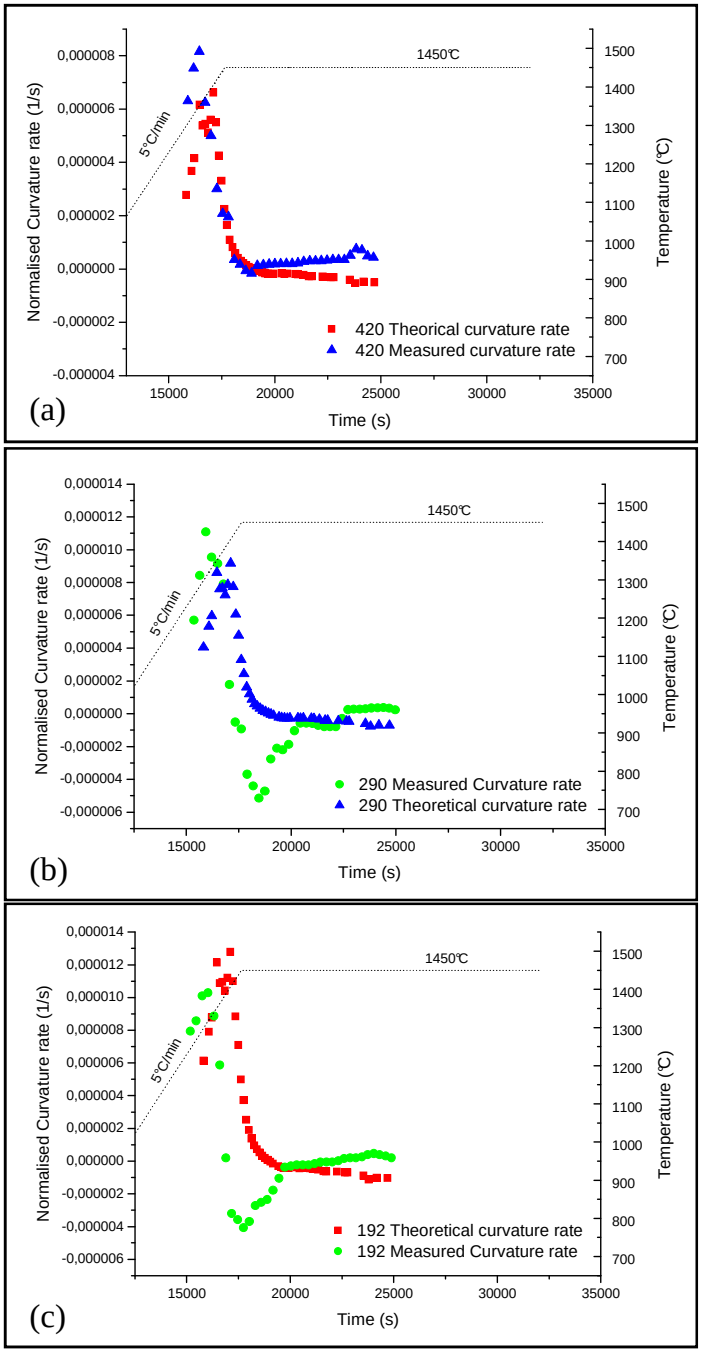

Fig. 73. Comparison between the calculated normalized curvature rate and the experimental data. Sample green thickness is: 420 µm (a), 290 µm (b), 192 µm (c).

The curvature rate prediction follows the experimental data fairly well for the thicker bi-layer in Fig. 73a. By decreasing the total thickness to 290 µm and 192 µm, the mismatch between theoretical and experimental data increases. A possible explanation for this observation could be the following: the bi-layers considered here show an initial positive curvature (anode on concave side). During the sintering process - but in particular when the viscosity is low (at low densities) - the self weight of the sample tends to flatten the cell, thus acting against the curvature rate due to anode faster sintering. This simulates the effect of a faster sintering electrolyte. The thicker the bi-layer, the less the "flattening" effect due to the gravity plays a role. For very thin layers (290 and 192 micrometers) this effect is more prominent.

3.7.7 Summary

A new experimental method for measuring the uniaxial viscosity of thin porous ceramic layers was proposed. This method consists in applying a low tensile load to the ceramic compact, which is undergoing densification. The resulting reduction in the strain rate is used to calculate the viscosity. The tensile load is deriving from the sample weight. For ceramics o a few tenths of millimeters in length, the stress magnitude is in the order of 0.1 kPa. This very low load is orders of magnitude lower than the values of sintering stress found in the literature for polycrystalline oxide ceramics (from 100 kPa to 100 MPa). The small load is therefore thought to not induce any anisotropy in the ceramic microstructure.

The developed method was applied to the measurement of the viscosity of an anode and an electrolyte tape cast layers. The obtained values allowed to model the curvature rate of half-cell upon sintering. The calculated data and the experimental ones are in fairly good agreement in case of relatively thick samples.

The calculations are limited to the zones of low viscosity: being the applied load very low, its effect on the shrinkage rate is measurable only at low viscosities. However, for the purpose of this study, the knowledge of the uniaxial viscosity at high densities and low shrinking rate is not needed. In fact the most severe curvature and curvature rate are always experienced in the firsts stages of sintering. Also the mismatch sintering stresses are more critical in this stage, when the ceramics are still very porous and their strength is low. One of the major limitation in using this approach for modelling the curvature for very large area samples, is the fact that, when a large area half-cell develops a sufficient curvature, not only the mismatch sintering stresses are the driving forces for the cell to bend, but also the gravity force will cause bending stresses which cannot be neglected. This will result in a more complex deformation, not a single sided curvature as in small samples.

3.8 Micro tubular cell with embedded current collector[4]

3.8.1 Introduction

Two main SOFC designs are being studied by researches all over the world and are starting to open their ways towards commercialization, the planar configuration and the tubular one. Among the tubular cells, a general distinction is drawn between the traditional macro-tubular design (diameter > 15 mm) and the more recent micro-tubular one (diameter < 5 mm).

The micro-tubular architecture is gaining increasing interest especially for portable applications. The major advantages in the *micro tubular* SOFC design, are (i) high volumetric power density (power generated per unit volume) compared to the standard tubular design (since the theoretical volumetric power density is inversely proportional to the electrolyte diameter), (ii) high thermal shock resistance, and (iii) rapid turn on/off capability (5), (46), (156), resulting from low thermal mass.

Tubular solid oxide fuel cells, having diameter greater than a few millimeters, are usually produced by extrusion or co-extrusion of the support electrode, which may be the anode or the cathode (57), (157), (158) with the electrolyte. In some cases, an inner sacrificial core of a fugitive material (*e. g.* carbon black), (159) is used; the current collector is then

[4] Adapted from Cologna M., De La Torre R., Sglavo V. M., Raj R., "Micro-tubular solid oxide fuel cells with embedded current collector", Ceramic Engineering and Science Proceeding 2009; Cologna M., Sglavo V. M., Raj R., “Micro-Fibre Solid Oxide Fuel Cells by Dip-Coating”, Proceeding of the 8th European Solid Oxide Fuel Cell Forum, Lucerne, CH, 2008; Italian patent application TO2008A000456.

inserted within the tube in a second step. Efforts have been made to reduce the total cell diameter to the sub-millimeter range. However, one of the limiting factors preventing the cells to be further scaled down are the technological challenges encountered in extruding such small tubes, and in inserting the inner current collector into such very small-diameter hollows (5).

In the new process presented here thin ceramic layers are deposited on to a metallic wire, which serves as the anode current collector, to construct a sub–millimeter tubular fuel cell system. A variety of well established technologies may be employed to deposit thin electrolyte layers in the tubular SOFC design. Examples are: conventional dip-coating from a slurry (159), (160), (161), modified dip-coating (162), sol-gel technique (163), (164), electrochemical vapor deposition (EVD) (165), chemical vapor deposition from metal–organic precursors (MOCVD) (166), (167), physical vapor deposition (PVD) (168), electrophoretic deposition (EPD) (46) and a whole range of more or less conventional processing technologies (4), (16). Among all the fabrication methods, it is usually recognized (although not unanimously) that colloidal processing is the most economical route for producing ceramics with good thermal and mechanical properties (57), (58).

In this work we report the fabrication of a micro tubular solid oxide fuel cell with outside diameter in the sub-millimeter range. In this novel cell design, the support for the cell fabrication consists of a thin metallic wire, on to which the porous anode layer, the electrode and the cathode, are deposited in succession. Environmental impact and cost of the processing was minimized by using only water based technologies. The use of expensive equipment was avoided by using dip coating for cell fabrication. Anode and electrolyte were based on the state of the art materials. Well-established

materials, such as porous nickel–zirconia cermet for the anode catalyst, ytrria–doped zirconia for the electrolyte and mixed conducting oxides deposited on the outer surface of the fiber for the cathode, were used. Slurries suitable for dip coating were developed in order to obtain a thin electrolyte coating onto the anode. The organic binder amount was tailored in order to avoid drying defects.

This new approach allows the simple scaling down of the cell to a few hundred micrometers and potentially less. Micro tubular SOFCs with total diameters in the sub-millimeter range with dense and crack free electrolytes were successfully produced. The electrical characteristics of the fiber–cell are measured using a simple specially designed testing apparatus.

3.8.2 Materials and methods

Commercial ceramic oxides powders were employed for the slurries production: 8 mol% yttria stabilized zirconia (YSZ) for the electrolyte (TZ8-YS, Tosoh, Japan) and a mixture of 58 wt% NiO (J.T. Baker Inc., USA) and 42 YSZ (TZ8-Y, Tosoh) for the anode.

Distilled water was used as dispersing medium and an ammonium polyacrylate water solution (Darvan 821A, R.T. Vanderbilt Inc., USA) as dispersant. A low molecular weight and a higher molecular weight polyethylene glycol were used as water soluble binders (PEG 600 and PEG 20000, Fluka). PEG 600 was used without water addition, being liquid at room temperature (25°C), while PEG 20.000 needed to be predissolved in distilled water. In order to obtain an anode with a high porosity, a fugitive

material was used as pore former (Graphite flake, median 7-10 µm, Alfa Aesar) [15]. Slurries composition is reported in Table 8.

Table 8. Slurries composition (wt%).

Component	Electrolyte	Anode
YSZ	48,21	14,60
NiO	-	20,10
Solvent (Water)	17,36	12,60
Dispersant	2,89	2,10
Pore former	-	5,25
PEG 600	7,86	12,57
PEG 20000	23,65 (23 wt% in H2O)	32,78 (37,5 wt% in H2O)

The process flowchart for the half-cells (anode and electrolyte) production is shown in Fig. 74. The ceramic powders were mixed with water and dispersant in a jar half filled with YSZ grinding media and milled in a high energy vibratory mill. Then the binders were added and the suspension was mixed by a magnetic stirrer.

The metallic supports and inner current collectors consisted of pure Ni wires (Puratronic, Alfa Aesar), with diameters ranging from 50 to 250 µm; the wires were used either straight or coiled around a core with diameter of 100 or 200 µm. The Ni supports were dipped in the anodic slurry and coated

with a withdrawal speed of 0.3 m/min and dried at 80°C. This step was repeated when higher anode thickness was desired.

The anode coated wire was then dipped in the electrolyte slurry and dried. After a slow de-binding step up to 500°C, the coatings were co-sintered at temperatures ranging from 1350°C to 1400°C.

The cathode was then applied by brushing on the sintered electrolyte an ink prepared from commercial LSCF-GDC composite powders (Specific Surface Area 4-8 m^2/g, FuelCellMaterials, Lewis Center, Ohio, USA), and fired for 1 h at 1100°C.

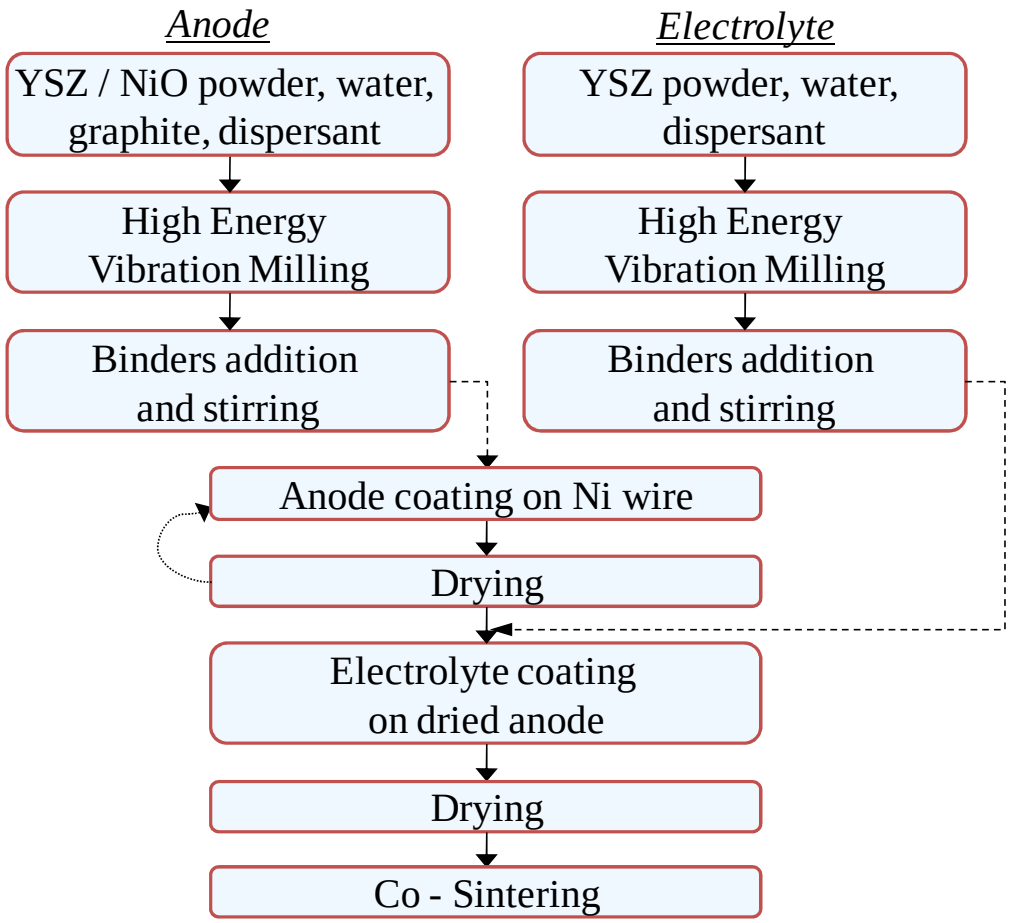

Fig. 74 Process flowchart for half-cell production.

A homemade testing apparatus was specially designed in order to allow the electrochemical characterization of the micro tubular cell; the sketch of the set-up is reported in Fig. 75: one end of the tubular cell was inserted in an alumina tube (fuel feeding tube) and sealed with a high temperature sealant (Ceramabond 885 and 885-T, Aremco Products Inc., USA). A gold wire was wrapped around the cathode for current collecting, while the current from the anode was collected directly through the nickel support coil. The cell mounted on the fuel feeding tube was then inserted in a tubular furnace and heated to 800°C in approximately 30 min. The anode was then reduced in-situ under a forming gas flow and the cell was then tested with the cathode in static air and the anode under humidified hydrogen flow. Labview software (National Instruments, USA) was used to control the data acquisition process.

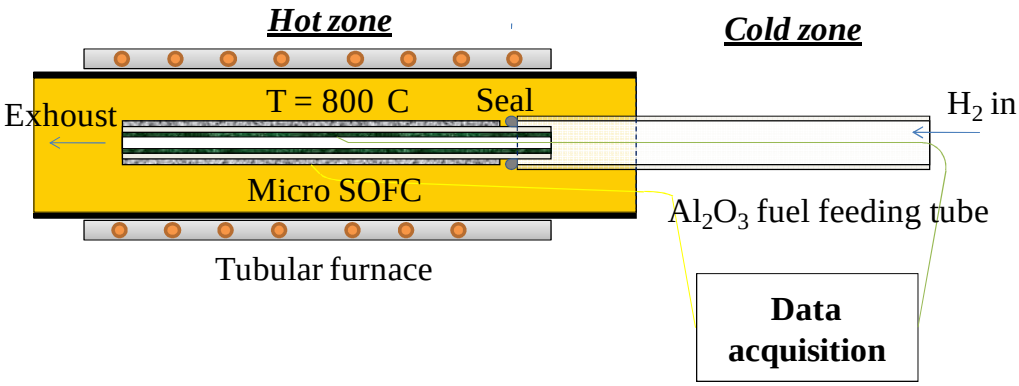

Fig. 75. Sketch of the testing apparatus (not scaled).

3.8.3 Results and discussion

Crack free green layers were produced under uncontrolled humidity conditions even after drying at elevated temperature (80°C). This was achieved by tailoring the quantity of the high and low molecular weight polymers in preliminary experiments. Being the electrolyte layer thinner than the anode, and therefore the drying stresses lower, less organic phase was needed to avoid the drying cracks. Around 35 vol% organic binder was found to be sufficient in the electrolyte slurry, while more than 50 vol% had to be used in the anode slurry. The drying of the anode was relatively quick (less than 5 min) and sequential depositions followed by drying made possible to reach the desired anode thickness. Being the electrolyte layer thinner than the anode, and therefore the drying stresses lower, less organic phase was needed to avoid the drying cracks. Around 35 vol% organic binder was found to be sufficient in the electrolyte slurry, while more than 50 vol% had to be used in the anode slurry.

With this method it was also possible to produce anodes with graded composition and porosity, simply by sequentially dipping the anode in slurries with different compositions and amount of pore former. The viscosity of the electrolyte suspension was tailored by adjusting the water content in preliminary experiments, in order to achieve the deposition of YSZ green layers with thicknesses in the range of 15 - 20 μm.

When the anode coated on a straight Ni wire was sintered, it retained enough porosity and no flaws were observed. A typical anode microstructure developed after sintering for 2 h at 1350°C is reported in Fig. 76.

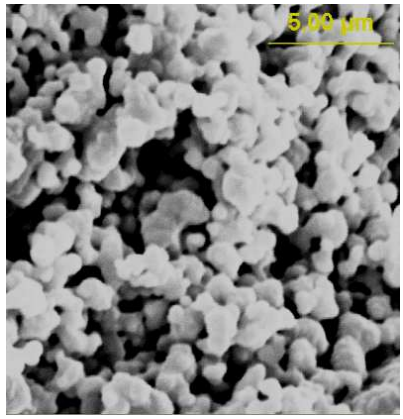

Fig. 76. Typical anode microstructure developed after sintering for 2 h at 1350°C on a straight Ni wire.

However, when the electrolyte and the anode layers were co-sintered on the straight Ni wire at temperatures ranging from 1350 to 1400°C, various types of defects were observed. Such defects included longitudinal cracks or periodical macroscopic cracks along the fiber length and/or insufficient electrolyte densification. Examples of such cracks are shown in Fig. 77 and Fig. 78. The poor YSZ density was attributed to the constrained sintering of the electrolyte powders on the rigid metallic wire, while the periodical cracks were thought to occur due to a combination of thermal stresses and sintering stresses.

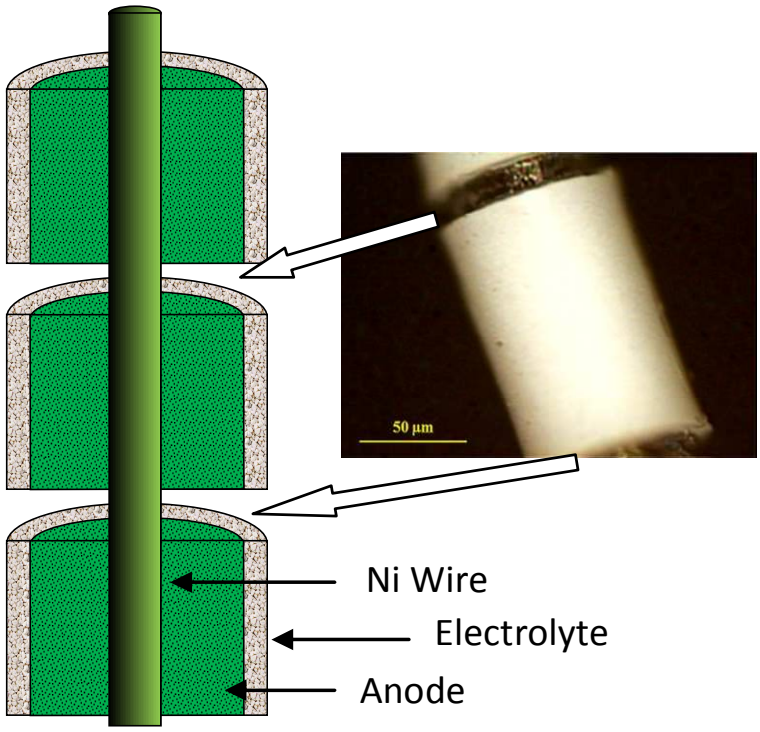

Fig. 77. Example of a periodical crack developed during co-sintering of electrolyte and anode coated on a straight Ni wire support.

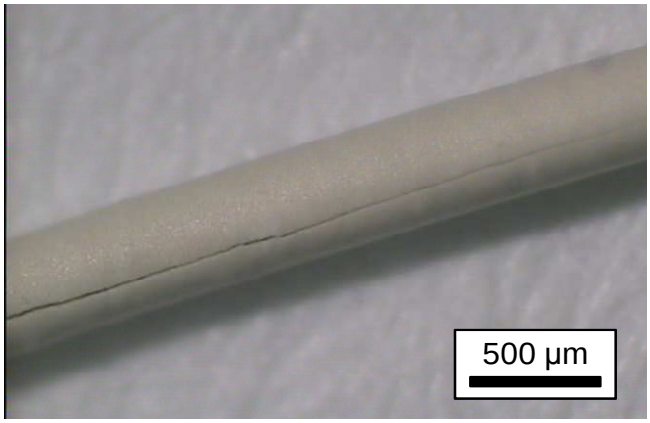

Fig. 78. Example of a longitudinal crack developed during co-sintering of electrolyte and anode coated on a straight Ni wire support.

In order to alleviate the overall stresses, the original cell design was modified and the Ni support wires were used after coiling them around a central core, therefore forming a spiral. The anode and electrolyte sintered on this less rigid support resulted in crack free layers. No defects were found when the Ni support wire was used in the coiled form; in such case a denser microstructure of the electrolyte layer was obtained. It was thought that the coil geometry allowed a less constrained sintering of the thin YSZ layer, thus alleviating the overall stresses. The best results in terms of electrolyte final density and absence of cracks were obtained with smaller wire and coil diameters.

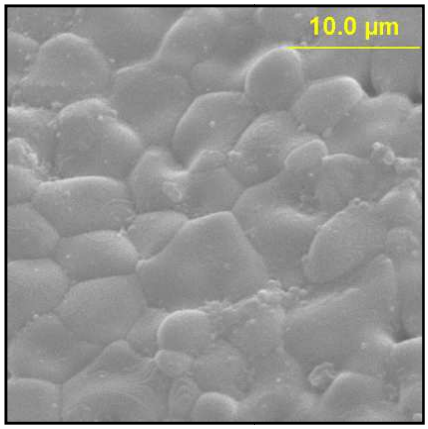

Fig. 79. Electrolyte surface of a half-cell co-sintered for 2 h at 1350°C, obtained by slurry coating a Ni coil support.

The electrolyte thickness was ranging from 10 µm to few tenths of micrometers, depending on the withdrawal speed and the anode support outer diameter. Half cell with a total diameter of 300 µm or even less were successfully obtained by coating nickel wires as thin as 50 µm coiled around a core of 100 µm in diameter. The electrolyte surface of a cell obtained by

co-sintering at 1350°C is shown in Fig. 79, were the dense obtained microstructure is clear. A gas tight electrolyte and a good joining of the layers were therefore obtained.

Moreover, the use of a coiled wire allowed the direct and simple creation of an internal hollow core to facilitate the hydrogen flow and limit the pressure drop along the cell, without the need for any sacrificial layer. By tailoring the coil spacing and geometry and the anodic slurry viscosity, it was possible to obtain hollow cores of various diameters. The micrograph in Fig. 80 reports the cross section of a half-cell, where the central hollow, the support wire, the porous anode and the electrolyte are clearly visible.

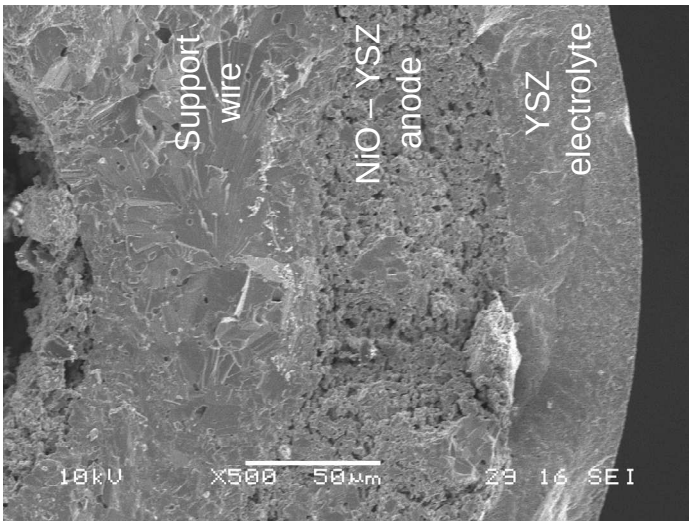

Fig. 80. Cross section of a tubular cell, as sintered.

A cross section of a half-cell pointing out the porous anode microstructure, the dense electrolyte and the inner core is shown in Fig. 81, and an overview of some produced cells is shown in Fig. 82, where the shape of the support coil is evident along the length of the cells.

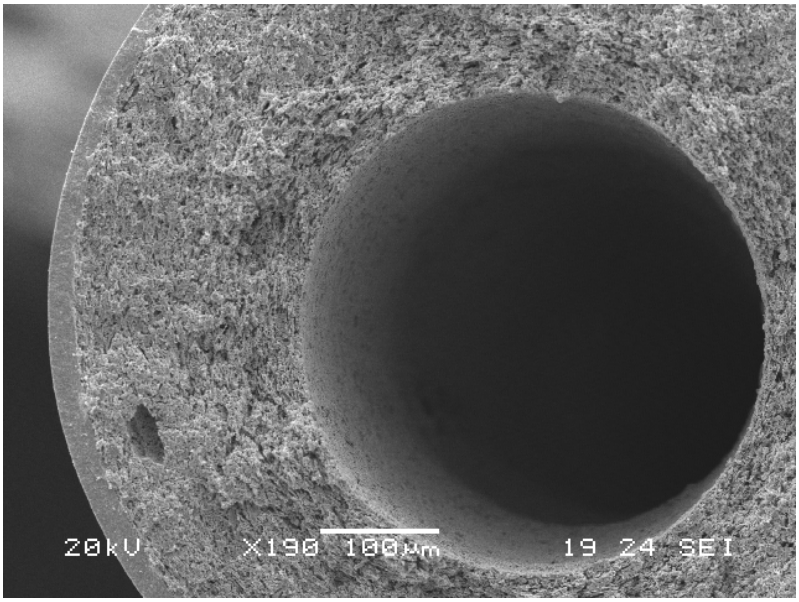

Fig. 81. Cross section of a of a half-cell co-sintered for 2 h at 1350°C, obtained by slurry coating a Ni coil support.

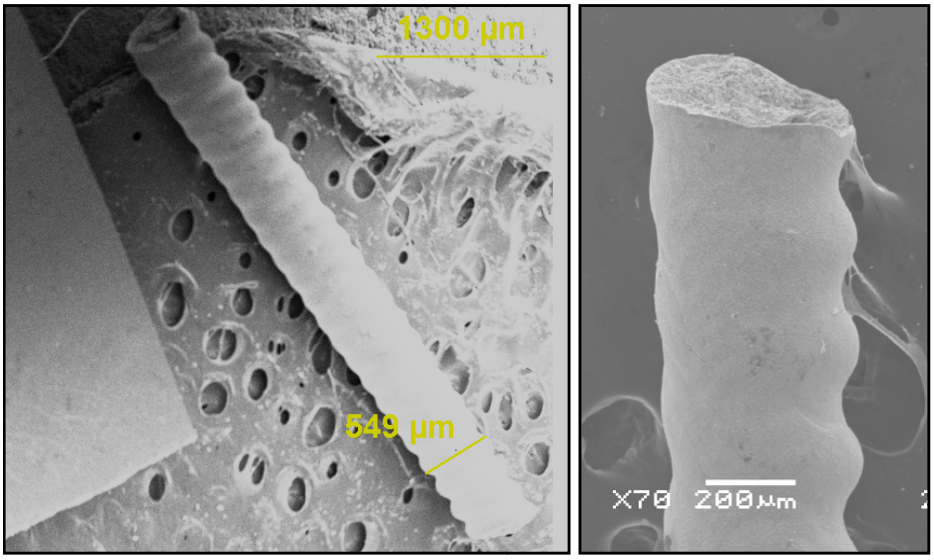

Fig. 82. Example of some of the produced half-cells. The shape or the coiled support Ni wire is evident.

After the cathode application, the cell were tested in the previously described apparatus, showing an open circuit voltage (OCV) of 0,93V and an estimated maximal power density of 0,5 mW/cm^2. While the OCV is in agreement with the expectations, considering the fact that the tested cells were only a few millimeters long and that one end of the cell was exposed to air, the power density seems to be low compared to other state of the art SOFCs. Such limited performance can be attributed to the difficulties of obtaining reliable data under the chosen testing condition, related to problems in positioning the cathode current collector, in measuring exactly the effective active electrolyte area, in obtaining a completely gas tight sealing; in addition, since one end of the cell was not sealed the last portion of the anode was exposed to oxygen and to red-ox cycles. Nevertheless, the viability of the micro tubular SOFC supported on nickel wire, with a dense electrolyte on a porous anode, produced by colloidal deposition and co-sintering was demonstrated.
Improvements in the testing apparatus and in the cathode deposition process as well are expected to improve the measurable performance of the cell further.

3.8.4 Summary

A new design for micro tubular SOFC with embedded current collector has been presented. The cell diameter can be in the sub millimeter range. The cell is built around a thin metallic wire which serves both as a support for cell manufacturing, as well as a current collector. Inexpensive ceramic

powder technologies were chosen for the cell fabrication. When the Ni support was used in the form of a straight wire, cracks related to the firing process were always found and a cell could not be successfully built. Instead, the use of a metallic spiral as a support, allowed the production of tubular cells with diameters as small as a few hundred micrometers, with a hollow core, a porous anode and a dense and crack-free electrolyte microstructure. In spite the power densities obtained are low in these early experiments, the results show the viability of the Micro Fibre Fuel Cell concept. It is believed that optimisation of cathode deposition, current collection and testing set-up will to increase the measured power densities significantly. The feasibility of a straightforward production route for sub-millimeter tubular SOFC with embedded current collector by means of very cheap technologies was thus demonstrated.

Conclusions

A reliable and economic process for the one step fabrication of large area anode supported planar fuel cells has been successfully developed in the present work. Such process is based on sequential tape casting technology, and does not necessitate any lamination step. Defects related to the green compact were reduced by optimizing the powders dispersions. Constrained sintering related defects were eliminated by matching the sintering kinetics of the anode and the electrolyte.

The influence of different parameters on sintering kinetics and developed curvature was studied. Heating rate, powder size, powder calcinations, type and level of doping elements were considered. The curvature developed upon co-firing was monitored during the whole sintering process, by using a specifically built high temperature imaging apparatus, which allows the direct determination of the best condition to obtain flat cell without any additional creep flattening.

The estimation of curvature rate allowed some qualitative insight on the developed internal stresses that account for cell failure. The crack development and crack extensions were related to the magnitude of the curvature rate. Cracks were found only in samples where the electrolyte was sintering under a tensile stress.

A slow heating rate was found to be beneficial for limiting the developed curvature. As far as the doping elements are concerned, Al was shown to increase the anode sintering rate while Ce reduces it. The use of reactive

elements, if carefully controlled, can be successfully employed to tailor the anode sintering curves. High quality cells that show low curvature rates and are flat at the end of the sintering process were obtained starting from 1 mol% Al-doped NiO powder. Such cells show a power density of 670 mW/cm^2 at 0.6 V and 800°C with LSM cathode.

Small changes in anode or electrolyte starting powder size have strong effects on the developed curvature, and specific mixtures of coarse and fine powders can reduce the curvature rates. By further optimizing the green compositions and by calcining NiO powder, an almost perfect matching of anode and electrolyte sintering rates was obtained, this resulting in a virtually unconstrained co-sintering. A cell, which did not develop any significant curvature during the whole firing process was developed, thus demonstrating the feasibility of a straightforward anode supported half-cell production. Microstructural observations and electrochemical tests confirmed the absence of defects in the cells produced with the tailored starting microstructure.

In addition, a new experimental method for measuring the uniaxial viscosity of thin porous ceramic layers was proposed. The developed method was applied to the measurement of the viscosity of an anode and an electrolyte tape cast layers. The obtained values allowed to model the curvature rate of half-cell upon sintering. The calculated data results in fairly good agreement with the experimental ones in case of relatively thick samples.

A novel design for micro tubular SOFC with embedded current collector has also been presented. Also in this case, inexpensive ceramic powder technologies were chosen for the cell fabrication. The formation of cracks upon the firing process was avoided with the use of a metallic spiral as support. Micro-tubular cells with external diameter of a few hundreds

micrometers, with hollow core, porous anode and dense and crack-free electrolyte microstructure were successfully produced. The obtained power densities in the early experiments were low, but the results showed the viability of the micro fibre fuel cell concept. It is believed that optimisation of cathode deposition, current collection and testing set-up will to increase the measured power densities significantly. The feasibility of a straightforward production route for sub-millimetre tubular SOFC with embedded current collector by means of very cheap technologies was therefore demonstrated and is encouraging further research.

References

1. **EG&G Technical Services, Inc.** *Fuel Cell Handbook (Seventh Edition).* Morgantown, West Virginia, USA : U.S. Department of Energy, 2004.

2. **K. Xie, Q. Ma, B. Lin, Y. Jiang, J. Gao, X. Liu, G. Meng.** An ammonia fuelled SOFC with a BaCe0.9Nd0.1O3−δ thin electrolyte prepared with a suspension spray. *Journal of Power Sources.* Vol. 170, 1, p. 38-41.

3. **L. Blum, W. A. Meulenberg, H.Nabielek, R. Steinberger-Wilckens.** Worldwide SOFC Technology Overview and Benchmark. *International Journal of Applied Ceramic Technology.* 2005, Vol. 2, p. 482–492.

4. **K. C. Wincewicz, J. S. Cooper.** Taxonomies of SOFC material and manufacturing alternatives. *Journal of Power Sources.* 2005, Vol. 140, p. 280–296.

5. **S. C. Singhal, K. Kendall.** *High Temperature Solid Oxide Fuel Cells: Fundamentals, Design and Applications.* Oxford, UK : Elsevier Ltd., 2003.

6. **Singhal, S.** Ceramic Fuel Cells for Stationary and Mobile Applications. *American Ceramic Society Bulletin.* 2003, p. 9601-9610.

7. **C.Williams, M.** SolidOxide Fuel Cells: Fundamentals to Systems. *Fuel Cells.* 2007, Vol. 7, 1, p. 78–85.

8. **Srinivasan, S.** *Fuel Cells, From Fundamentals to Applications.* New York : Springer, 2006. lSBN-10: 0-387-25116-2.

9. **Sammes, N.** *Fuel Cell Technology, Reaching Towards Commercialization.* Germany : Springer, 2006. ISBN-10: 1-85233-974-8.

10. **N. Sammes, A. Smirnova, O. Vasylyev.** *Fuel Cell Technologies: State and Perspectives.* Dordrecht, The Netherlands : Springer, 2004. ISBN-10 1-4020-3498-9.

11. **Singhal, S. C.** Solid Oxide Fuel Cells. *The Electrochemical Society Interface.* 2007, Vol. 16, 4, p. 41-44.

12. **Jiang, S. P.** Development of lanthanum strontium manganite perovskite cathode materials of solid oxide fuel cells: a review. *Journal of Material Science.* 2008, Vol. 43, p. 6799–6833.

13. **S. S. Penne, A. J. Appleby, B. S. Baker, J. L. Bates, L. B. Buss, W. J. Dollard, P. J. Farris, E. A. Gillis, J. A. Gunsher, A. Khandkar, M. Krumpelt, J. B. O'Sullivan, G. Runte, R. F. Savinell, J. R. Selman, D. A.**

Shores, P. Tarman. Commercialization of fuel cells. *Progress in Energy and Combustion Science.* 1995, Vol. 21, 2.

14. **Zegers, P.** Fuel cell commercialization: The key to a hydrogen economy. *Journal of Power Sources.* 2006, Vol. 154, 2, p. 497-502.

15. **S. Desouza, S. J. Visco, L. C. Dejonghe.** Thin-Film Solid Oxide Fuel-Cell with High-Performance at Low-Temperature. *Solid State Ionics.* 1997, Vol. 98, 1-2, p. 57-61.

16. **J. Will, A. Mitterdorfer, C. Kleinlogel, D. Perednis, L. J. Gauckler.** Fabrication of thin electrolytes for second-generation solid oxide fuel cells. *Solid State Ionics.* 2000, Vol. 131, 1-2, p. 79-96.

17. **S. Zha, M. Liu.** *Novel Electrode Materials for Low-Temperature Solid-Oxide Fuel Cells.* Atlanta, GA : s.n., 2005. DOE Award Number: DE-FG26-01NT41274.

18. **Y. J. Leng, S. H. Chan, S. P. Jiang, K. A. Khor.** Low-temperature SOFC with thin film GDC electrolyte prepared in situ by solid-state reaction. *Solid State Ionics.* 2004, Vol. 2004, p. 9-15.

19. **W. J. Quadakkers, H. Greiner, M. Hansel, A. Pattanaik, A.S. Khanna, W. Mallener.** Compatibility of Perovskite Contact Layers Between Cathode and Metallic Interconnectrorplates of SOFCs. *Solid State Ionics.* 1996, Vol. 91, p. 55-67.

20. **T. Brylewki, M. Nanko, T.Maruyama, K. Przybylski.** Application of Fe–16Cr Ferritic Alloy to Interconnector for a Solid Oxide Fuel Cell. *Solid State Ionics.* 2001, Vol. 143, p. 131-150.

21. **Steele, B. C. H.** Materials for IT-SOFC stacks 35 years R&D: the inevitability of gradualness. *Solid State Ionics.* 2000, Vol. 134, p. 3-20.

22. **S. Tao, J. T. S. Irvine.** A redox-stable efficient anode for solid-oxide fuel cells. *Nature Materials.* 2003, Vol. 2, p. 320 - 323.

23. **B. C. H. Steele, A. Heinzel.** Materials for fuel-cell technologies. *Nature.* 2001, Vol. 414, p. 345-352.

24. **N. M. Sammes, G. A. Tompsett, H. Naefe, F. Aldinger.** Bismuth Based Oxide Electrolytes - Structure and Ionic Conductivity. *Journal of the European Ceramic Society.* 1999, Vol. 19, p. 1801 - 1826.

25. **S. (R.) Hui, J. Roller, S. Yick, X. Zhang, C.e Decès-Petit, Y. Xie, R. Maric, D. Ghosh.** A brief review of the ionic conductivity enhancement for selected oxide electrolytes. *Journal of Power Sources* . 2007 , Vol. 172, p. 493–502.

26. **Arachi Y., Sakai H., Yamamoto O., Takeda Y., Imanishai N.** Electrical conductivity of the ZrO2-Ln2O3 (Ln=lanthanides) system . *Solid State Ionics.* 1999, Vol. 121, 1, p. 133-139.

27. **M. Mogensen, N. M. Sammes, G. A. Tompsett.** Physical, chemical and electrochemical properties of pure and doped ceria. *Solid State Ionics.* 2000, Vol. 129, p. 63–94.
28. **A. Atkinson, S. Barnett, R. J. Gorte, J. T. S. Irvine, A. J. McEvoy, M. Mogensen, S. C. Singhal, J. Vohs.** Advanced anodes for high-temperature fuel cells. *Nature Materials.* 2004, Vol. 3, p. 17-27.
29. **Spacil, H. S.** *Electrical device including nickel-containing stabilized zirconia electrode. 3,558,360* US, 1970.
30. **H. Koide, Y. Someya, T. Yoshida, T. Maruyama.** Properties of Ni/YSZ cermet as anode for SOFC. *Solid State Ionics.* 2000, Vol. 132, p. 253–260.
31. **W.Z. Zhu, S.C. Deevi.** A review on the status of anode materials for solid oxide fuel cells. *Materials Science and Engineering A.* 2003, Vol. 362, p. 228–239.
32. **S.K. Pratihar, R.N. Basu, S. Mazumder, H.S. Maiti.** Honolulu, Hawaii, : s.n., 17–22 October 1999. Proceedings of the Sixth International Symposium on Solid Oxide Fuel Cells (SOFC-VI). p. 513.
33. **S. K. Pratihar, A. Das Sharma, H.S. Maiti.** Electrical behavior of nickel coated YSZ cermet prepared by electroless coating technique. *Materials Chemistry and Physics.* 2006, Vol. 96, p. 388–395.
34. **S. Mcintosh, J. M. Vohs, R. J. Gorte.** Effect of Precious-Metal Dopants on SOFC Anodes for Direct Utilization of Hydrocarbons. *Electrochemical and Solid-State Letters.* 2003, Vol. 6, 11, p. A240-A243.
35. **Montinaro, D.** *Synthesis and Processing of Oxides Powders for Solid Oxide Fuel Cells (SOFC) Production, PhD thesis.* s.l. : Università degli Studi di Trento, 2007.
36. **M. J. L. Ostergard, C. Clausen, C. Bagger, M. Mogensen.** Manganite-Zirconia Composite Cathodes for SOFC: Influence of Structure and Compositions. *Electrochimica Acta.* 1995, Vol. 40, 12, p. 1971-1981.
37. **V.A.C. Haanappel, J. Mertens, D. Rutenbeck, C. Tropartz, W. Herzhof, D. Sebold, F. Tietz.** Optimisation of processing and microstructural parameters of LSM cathodes to improve the electrochemical performance of anode-supported SOFCs. *Journal of Power Sources.* 2005, Vol. 141, 2, p. 216-226.
38. **E. Ivers-Tiffe´e, A. Weber, D. Herbstritt.** Materials and technologies for SOFC-components. *Journal of the European Ceramic Society.* 2001, Vol. 21, p. 1805–1811.
39. **A. Boudghene Stambouli, E. Traversa.** Solid oxide fuel cells (SOFCs): a review of an environmentally clean and efficient source of

energy. *Renewable and Sustainable Energy Reviews.* 2002, Vol. 6, p. 433–455.

40. **L. Blum, W. A. Meulenberg, H. Nabielek, R. Steinberger-Wilckens.** Worldwide SOFC Technology Overview and Benchmark. *International Journal of Applied Ceramic Technology.* 2005, Vol. 2, p. 482–492.

41. **Y. B. Matusa, L. C. De Jonghe, C. P. Jacobson, S. J. Visco.** Metal-supported solid oxide fuel cell membranes for rapid thermal cycling. *Solid State Ionics* . 2005, Vol. 176, p. 443–449.

42. **D. Stöver, D. Hathiramani, R. Vaßen, R. J. Damani.** Plasma_sprayed components for SOFC applications. *Surface & Coatings Technology.* 2006, Vol. 201, p. 2002–2005.

43. **S. (R.) Hui, D. Yang, Z. Wang, S. Yick.** Metal-supported solid oxide fuel cell operated at 400–600°C. *Journal of Power Sources.* 2007, Vol. 167, p. 336–339.

44. **M.C. Williams, J.P. Strakey, S. C. Singhal.** U.S. distributed generation fuel cell program. *Journal of Power Sources.* 2004, Vol. 131, p. 79–85.

45. **Hassmann, K.** SOFC Power Plants, the Siemens-Westinghouse Approach. [a cura di] 78-84. *Fuel Cells.* 2001, Vol. 1, 1.

46. **P. Sarkar, L. Yamarte, H. Rho, L. Johanson.** Anode-Supported Tubular Micro-Solid Oxide Fuel Cell. *International Journal of Applied Ceramic Technology.* 2007, Vol. 4, p. 103–108.

47. **M. Lang, T. Franco, G. Schiller, N. Wagner.** Electrochemical characterization of vacuum plasma sprayed thin-film solid oxide fuel cells (SOFC) for reduced operating temperatures. *Journal of Applied Electrochemistry.* 2002, Vol. 32, p. 871–874.

48. **R. Vaßen, , D. Hathiramani, J. Mertens, V.A.C. Haanappel, I.C. Vinke.** Manufacturing of high performance solid oxide fuel cells (SOFCs) with atmospheric plasma spraying (APS). *Surface and Coatings Technology.* 2007, Vol. 202, p. 499–508.

49. **J-H Song, S.-I. Park, J.-H. Lee, H.-S. Kim.** Fabrication characteristics of an anode-supported thin-film electrolyte fabricated by the tape casting method for IT-SOFC. *Journal of Materials Processing Technology.* 2008, Vol. 198, 3, p. 414-418.

50. **M. P. Albano, L. B. Garrido.** Aqueous tape casting of yttria stabilized zirconia. *Materials Science and Engineering A.* 2006, Vol. 420, p. 171–178.

51. *Performance and characterisation of anode-supported cells co-cast with thin 8YSZ.* **Ihringer, R., Rambert, S. Van herle.** Switzerland : U, Bossel, 2000. Proceedings of the 4th European Solid Oxide Fuel Cell Forum. p. 241–251.

52. **J. Gurauskis, C. Baudin, A.J. Sanchez-Herencia.** Tape casting of Y-TZP with low binder content. *Ceramics International.* 2007, Vol. 33, p. 1099–1103.
53. **B. Savignat, M. Chiron, C. Barthet.** Tape casting of new electrolyte and anode materials for SOFCs operated at intermediate temperature. *Journal of the European Ceramic Society.* 2007, Vol. 27, 2-3, p. 673-678.
54. **H. Moon, S. D. Kim, S. H. Hyun, H. S. Kimb.** Development of IT-SOFC unit cells with anode-supported thin electrolytes via tape casting and co-firing. *International Journal of Hydrogen Energy.* 2008, Vol. 33, 6, p. 1758-1768 .
55. **H.-G. Jung, Y.-K. Sun, H. Y. Jung, J. S. Park, H.-R. Kim, G.-H. Kim, H.-W. Lee, J.-H. Lee.** Investigation of anode-supported SOFC with cobalt-containing cathode and GDC interlayer. *Solid State Ionics.* 2008, Vol. 179, 27-32, p. 1535-1539.
56. **Bertoldi, M.** *High reliability ceramic laminates by design, PhD thesis.* Trento: Università degli Studi di Trento, 2004.
57. **T. Alston, K. Kendall, M. Palin, M. Prica, P. Windibank.** A 1000-cell SOFC reactor for domestic cogeneration. *Journal of Power Sources.* 1998, Vol. 71, p. 271-274.
58. **Lange, F. F.** Powder Processing Science and Technology for Increased Reliability. *Journal of the American Ceramic Society.* 1989, Vol. 72, p. 3 - 15.
59. **Reed, J. S.** *Principles of Ceramics Processing, 2nd Edition.* USA : John Wiley & Sons, 1995. ISBN 0-471-59721.
60. **Rahaman, M. N.** *Ceramic Processing and Sintering.* New York : Marcel Dekker, 2003.
61. **King, A. G.** *Ceramic Technology and Processing.* Norwich, NY : William Andrew, 2002. ISBN 0-8155-1443-3.
62. **Lewis, J. A.** Colloidal Processing of Ceramics. *Journal of the American Ceramic Society.* 2000, Vol. 83, 10, p. 2341–59.
63. **D. Hotza, P. Greil.** Review: aqueous tape casting of ceramic powders. *Materials science & engineering A.* 1995, Vol. 202, 1-2, p. 206-217.
64. **R. E. Mistler, E. R. Twiname.** *Tape Casting, Theory and Practice.* Westerville, OH : The American Ceramic Society, 2000.
65. **Rohm and Haas.** Duramax® Additives for Ceramic Processing. *Technical Report.* 2001.
66. **B. Bitterlich, C. Lutz, A. Roosen.** Rheological characterization of water-based slurries for the tape casting process. *Ceramics International.* 2002, Vol. 28, p. 675–683.

67. **D.-S. Park, C.-W. Kim.** A modification of tape casting for aligning the whiskers. *Journal of Materials Science.* 1999 , Vol. 34, 23, p. 5827-5832.
68. **M. Wu, G. L. Messing.** Fabrication of Oriented SiC-Whisker-Reinforced Mullite Matrix Composites by Tape Casting. *Journal of the American Ceramic Society.* 2005, Vol. 77, 10, p. 2586 - 2592.
69. **S. Kaji, N. Sakamoto.** Flow properties of aqueous perovskite-type oxide La0.6Sr0.4CoO3 suspension. *Solid State Ionics* . 1998, Vol. 108, p. 235–240.
70. **C. Chiu, M. J. Cima.** Drying of Granular Ceramic Films: II, Drying Stress and Saturation Uniformity. *Journal of the American Ceramic Society.* 1993, Vol. 76, 11, p. 2769–77.
71. **W.D. Kingery, H.K. Bowen, D.R. Uhlmann.** *Introduction to Ceramics, 2nd Edition.* New York : John Wiley and Sons, 1976.
72. **R. Zuo, E. Aulbach, J. Roedel.** Viscous Poisson's Coefficent Determined by Discontinuous Hot Forging. *Journal of Material Research.* 2003, Vol. 18, 9, p. 2170 - 2176.
73. **D. J. Green, O. Guillon, J. Rödel.** Constrained sintering: A delicate balance of scales. *Journal of the European Ceramic Society.* 2008, Vol. 28, p. 1451 – 1466.
74. **T. Cheng, R. Raj.** Measurement of the Sintering Pressure in Ceramic Films. *Journal of the American Ceramic Society.* 1988, Vol. 71, 4, p. 276 - 280.
75. **J. Kanters, U. Eisele, J. Roedel.** Cosintering simulation and experimantation: case study of nanocrystalline zirconia. *Journal of the American Ceramic Society.* 2001, Vol. 84, 12, p. 2757 - 2763.
76. **R. Zuo, E. Aulbach, J. Roedel.** Continuum mechanical approach to sintering of nanocrystalline zirconia. *Advanced Engineering Materials.* 2005, Vol. 7, 10, p. 949 - 952.
77. **Sherer, G. W.** Sintering with Rigid Inclusions. *Journal of the American Ceramic Society.* 1987, Vol. 70, 10, p. 719 - 725.
78. **R. K. Bordia, G. W. Scherer.** On constrained sintering. I. Constitutive model for a sintering body. *Acta Metallurgica.* 1988, Vol. 36, 9, p. 2393 - 2397.
79. —. On constrained sintering. II. Comparison of constitutive models. *Acta Metallurgica.* 1988, Vol. 36, 9, p. 2397-2409.
80. **R. K. Bordia, G. W. Sherer.** On constrained sintering. III. Rigid inclusions. *Acta Metallurgica.* 1988, Vol. 36, 9, p. 2411-2416.
81. **P. Z. Cai, G. L. Messing, D. J. Green.** Determination of the machanical response of sintering compacts by cyclic loading dilatometry. *J. Am. Ceram. Soc.* 1997, Vol. 80, 2, p. 445 - 452.

82. **P. Z. Cai, G. L. Messing, D. L. Green.** Constrained Densification of Alumina/Zirconia Hybrid Laminates, I: Experimental Observations of Processing Defects. *Journal of the American Ceramic Society.* 1997, Vol. 80, 8, p. 1929–1939.
83. **E. Aulbach, R. Zuo, J. Roedel.** Laser Assisted High Resolution Loading Dilatometer And Applications. *Experimental Mechanics.* 2004, Vol. 44, 1, p. 71 - 75.
84. **R. Zuo, E. Aulbach, J. Roedel.** Experimantal Determination of Sintering Stresses and Sintering Viscosities. *Acta Materialia.* 2003, Vol. 51, p. 4563 - 4574.
85. **R. K. Bordia, R. Zuo, O. Guillon, S. M. Salamone, J. Roedel.** Anisotropic constitutive laws for sintering bodies. *Acta Materialia.* 2006, Vol. 54, p. 111–118.
86. **J.- C. Chang, J.- H. Jean.** Self-Constrained Sintering of Mixed Low-Temperature-Cofired Ceramic Laminates. *Journal of the American Ceramic Society.* 829-835, 2006, Vol. 89, 3.
87. **A. Mohanram, S.- H. Lee, G. L. Messing, D. J. Green.** Constarined Sintering of Low-Temperature Co-Fired Ceramics. *Journal of the American Ceramic Society.* 2006, Vol. 89, 6, p. 1923 - 1929.
88. **O. Gillia, C. Josserond, D. Bouvard.** Viscosity of WC-Co Compacts During Sintering. *Acta Materialia.* 2001, Vol. 49, p. 1413 - 1420.
89. **J. B. Ollagnier, O. Guillon, J. Roedel.** Effect of Anisotropic Microstructure on The Viscous Properties of a LTCC Material. *Journal of the American Ceramic Society.* 2004, Vol. 87, 2, p. 192-196.
90. **J-P Ollagnier, O. Guillon, J. Roedel.** Viscosity of LTCC Determined by Discontinuous Sinter-Forging. *International Journal of Applied Ceramic Technology.* 2006, Vol. 3, 6, p. 437 - 441.
91. **S-H. Lee, G. L. Messing, D. J. Green.** Bending creep test to measure the viscosity of porous materials during sintering. *Journal of the American Ceramic Society.* 2003, Vol. 86, 6, p. 877 - 82.
92. **D. C. Blaine, R. Bollina, S.-J. Park, R. M. German.** Critical use of video-imaging to rationaliza computer sintering simulation models. *Computers in Industry.* 2005, Vol. 56, p. 867 - 875.
93. **A. G. Evans, J. W. Hutchinson.** The Thermomechanical Integrity of Thin Films and Multilayers. *Acta metallurgica Materialia.* 1995, Vol. 43, 7, p. 2507-2530.
94. **J.-H. Jean, C.-R. Chang.** Camber development during cofiring Ag-based low-dielectric-constant ceramic package. *Journal of Materials Research.* 1997, Vol. 12, 10, p. 2743-2750.

95. **M. Hagymàsi, A. Roosen, R. Karmazin, O. Dernovsek, W. Haas.** Constrained sintering of dielectric and ferrite LTCC tape composites. *Journal of the European Ceramic Society.* 2005, Vol. 25, p. 2061–2064.
96. **A. Hall A, E. K. Akdogan, A. Safari.** Fatigue properties of piezoelectric-electrostrictive Pb(Mg1/3, Nb2/3)O3–PbTiO3 monolithic bilayer composites. *Journal of Applied Physics.* 2006, Vol. 100, 9, p. 094105-094105-7.
97. **J. Feng, Y. Fan, H. Qi, N. Xu.** Co-sintering synthesis of tubular bilayer a-alumina membrane. *Journal of Membrane Science.* 2007, Vol. 288, p. 20–27.
98. **X.-J. Lu, P. Xiao.** Constrained sintering of YSZ/Al2O3 composite coatings on metal substrates produced from eletrophoretic deposition. *Journal of the European Ceramic Society* . 2007, Vol. 27, p. 2613–2621.
99. **O. Zubacheva, J. Malzbender, R.W. Steinbrech, L. Singheiser, U. Schulz.** Curvature Studies of Uncostrained Thermal Barrier Composites. *Ceramic engineering and science proceedings.* 2005, Vol. 26, 3, p. 29-36.
100. **G. Ye, F. Ju, C. Lin, S. Gopalan, U. Pal, D. Seccombe.** Single-Step Co-firing Technique for SOFC Fabrication. *Ceramic Engineering and Science Proceedings.* 2005, Vol. 26, 4, p. 25-32.
101. **R. Muecke, N. H. Menzler, H. P. Buchkremer, D. Stoever.** Cofiring of Thin Zirconia Films During SOFC Manufacturing. *Journal of the American Ceramic Society.* 2009, Vol. 92, p. 95 – 102.
102. **H. Riedel, H. Zipse, J. Svoboda.** Equilibrium pore surface, sintering stresses and constitutive-equations for intermediate and late stages of sintering. *Acta Metallurgica Materialia.* 1994, Vol. 42, 2, p. 445 - 452.
103. **A. R. Boccaccini, B. Hamann.** Review In Situ high-Temperature Optical Microscopy. *Journal of Material Science.* 1999, Vol. 34, p. 5419 - 5436.
104. **F. Raether, R. Springer, S. Beyer.** Optical dilatometry for the control of microstructure development during sintering. *Material Research Innovations.* 2001, Vol. 4, p. 245–250 .
105. **Raether, F. G.** Current State of In Situ Measuring Methods for the Control of Firing Processes. *J. Am. Ceram. Soc.* 2009, Vol. 92, p. 146–152.
106. **Clemmer, R. M.** *The Processing and Charachterization of Porous Ni/TSZ and NiO/YSZ Composites used in Solid Oxide Fuel Cell Applications, PhD thesis.* Ontario, Canada : Univerity of Waterloo, 2006.
107. **D. Montinaro, S. Modena, S. Ceschini, M. Bertoldi, T. Zandonella, A. Tomasi, V. M. Sglavo.** Anode Supported Solid Oxide Fuel Cells with Improved Cathode/Electrolyte Interface. *Ceramic Transactions.* 2006, Vol. 179, p. 139-147.

108. *Development and Characterization of Doped Ceria Buffer Layers.* **S. Modena, S. Ceschini, D. Montinaro, M. Bertoldi.** Lucerne, CH : s.n. p. Lucerne, CH. Proceedings of the 8th European Solid Oxide Fuel Cell Forum, 30 June – 4 July 2008.
109. **J. Cesarano III, I. A. Aksay.** Processing of Highly Concentrated Aqueous α-Alumina Suspensions Stabilized with Polyelectrolytes. *Journal of the American Ceramic Society.* 1988, Vol. 71, 12, p. 1062 – 1067.
110. **D. H. Lee, B. Derby.** Preparation of PZT suspensions for direct ink jet printing. *Journal of the European Ceramic Society.* 2004, Vol. 24, p. 1069–1072.
111. **F. Tietz, Q. Fu, V. A. C. Haanappel, A. Mai, N. H. Menzler, S. Uhlenbruck.** Materials Development for Advanced Planar Solid Oxide Fuel Cells. *International Journal of Applied Ceramic Technology.* 2007, Vol. 4, 5, p. 436–445.
112. **W. Li, K. Hasinska, M. Seabaugh, S. Swartz, J. Lannutti.** Curvature in Solid oxide fuel cells. *Journal of Power Sources.* 2004, Vol. 138, p. 145-155.
113. **C. H. Hsueh, G. Evans.** Residual Stresses and Cracking in Metal/Ceramic System for Microelectronics Packaging. *Journal of the American Ceramic Society.* 1985, Vol. 68, p. 120-127.
114. **J-H. Jean, C-R. Chang, Z-C. Chen.** Effect of Densification Mismatch on Camber Development during Cofiring of Nickel-Based Multilayer Ceramic Capacitors. *Journal of the American Ceramic Society.* 1997, Vol. 80, p. 2401-2406.
115. **O. Guillon, S. Krauß, J. Rödel.** Influence of thickness on the constrained sintering of alumina films. *Journal of the European Ceramic Society.* 2007, Vol. 27, p. 2623–2627.
116. **R - T. Hsu, J - H. Jean.** Key Factors Controlling Camber Behaviour During the Cofiring of Bi-Layer Ceramic Dielectric Laminates. *Journal of the American Ceramic Society.* 2005, Vol. 88, 9, p. 2429 – 2434.
117. **G.- Q. Lu, R. C. Sutterlin, T. K. Gupta.** Effect of Mismatched Sintering Kinetics on Camber in a Low-Temperature Cofired Ceramic Package. *Journal of the American Ceramic Society.* 1993, Vol. 76, 8, p. 1907-14.
118. **K. R. Venkatachari, R. Raj.** Shear deformation and densification of powder compacts. *Journal of the American Ceramic Society.* 1986, Vol. 69, 6, p. 499-506.
119. **R. K. Bordia, R. Raj.** Sintering Behaviour of Ceramic Films Constrained by a Rigid Substrate. *Journal of the American Ceramic Society.* 1985, Vol. 68, p. 287-292.

120. **T. Cheng, R. Raj.** Flaws Generation during Constrained Sintering of Metal-Ceramic and Metal-Glass Multilayer Films. *Journal of the American Ceramic Society.* 1989, Vol. 72, p. 1649-1655.
121. **C. Hillman, Z. Suo, F. F. Lange.** Cracking of laminates subjected to biaxial tensile stresses. *Journal of the American Ceramic Society.* 1996, Vol. 79, 8, p. 2127-33.
122. **V. M. Sglavo, P. Z. Cai, D. J. Green.** Damage in Al2O3 Sintering Compacts under Very Low Tensile Stress. *Journal of Material Science Letters.* 1999, Vol. 18, p. 895 - 900.
123. **A. Selcuk, G. Merere, A. Atkinson.** The influence of electrodes on the strength of planar zirconia solid oxide fuel cells. *Journal of Material Science.* 2001, Vol. 36, p. 1173 – 1182.
124. **L. Jia, Z. Lub, J. Miaob, Z. Liu, G. Li, W. Sua.** Effects of pre-calcined YSZ powders at different temperatures on Ni–YSZ anodes for SOFC. *Journal of Alloys and Compounds.* 2006, Vol. 414, p. 152–157.
125. **C. Müller, D. Herbstritt, E. Ivers-Tiffée.** Development of a multilayer anode for solid oxide fuel cells. *Solid State Ionics.* 2002, Vol. 152, p. 537–542.
126. **A. Atkinson, A. Selcuk.** Residual stress and fracture of laminated ceramic membranes. *Acta Materialia.* 1999, Vol. 47, p. 867–874.
127. **J. Malzbender, W. Fischer, R.W. Steinbrech.** Studies of residual stresses in planar solid oxide fuel cells. *Journal of Power Sources.* 2008, Vol. 182, p. 594–598.
128. **S-H. Lee, G. L. Messing, M. Awano.** Sintering Arches for Cosintering Camber-Free SOFC Multilayers. *J. Am. Ceram. Soc.* 2008, Vol. 91, 2, p. 421-427.
129. **D. Pohle, M. Wagner, A. Roosen.** Effect of Friction on Inhomogeneous Shrinkage Behavior of Structured LTCC. *J. Am. Ceram. Soc.* 2006, Vol. 89, 9, p. 2731-2737.
130. **Y. J. Leng, S. H. Chan, K. A. Khor, S. P. Jiang, P. Cheang.** Effect of characteristics of Y2O3-ZrO2 powders on fabrication of anode-supported solid oxide fuel cells. *Journal of Power Sources.* 2003, Vol. 117, p. 26–34.
131. **Garino, T.** The Co-Sintering of Electrode and Electrolyte Layered Structures for SOFC Applications. *Ceramic Engineering and Science Proceedings.* 2002, Vol. 23, 3, p. 759-766.
132. **W. Bao, Q. Chang, G. Meng.** Effect of NiO/YSZ compositions on the co-sintering process of anode-supported fuel cells. *Journal of Membrane Science.* 2005, Vol. 259, p. 103 - 109.

133. **S. P. Jiang, S. H. Chan.** A review of anode materials development in solid oxide fuel cells. *Journal of Material Science.* 2004, Vol. 39, p. 4405-4439.
134. **S. Primdahl, B. F. Sørensen, M. Mogensen.** Effect of Nickel Oxide/Yttria-Stabilized Zirconia Anode Precursor Sintering Temperature on the Properties of Solid Oxide Fuel Cells. *Journal of the American Ceramic Society.* 2000, Vol. 83, 3, p. 489–94.
135. **D. Dong, M. Liu, Y. Dong, B. Lin, J. Yang, G. Meng.** Improvement of the performances of tubular solid oxide fuel cells by optimizing co-sintering temperature of the NiO/YSZ anode-YSZ electrolyte double layers. *Journal of Power Sources.* 2007, Vol. 171, p. 495–498.
136. **B. Geller, B. Thaler, A. Fathy, M. J. Liberatore, H. D. Chen, G. Ayers, V. Pendrick, Y. Narayan.** 'LTCC-M: An Enabling Technology for High Performance Multilayer RF Systems. *Journal of Microwave Technology.* 1999, 7, p. 64–72.
137. **C. C. Huang, J. H. Jean.** Stress Required for Constrained Sintering of a Ceramic-Filled Glass Composite. *Journal of the American Ceramic Society.* 2004, Vol. 8, 87, p. 1454 - 8.
138. **C. D. Lei, J. H. Jean.** Effect of Crystallization on the Stress Required for Constrained Sintering of CaO–B2O3–SiO2 glass-ceramics. *Journal of the American Ceramic Society.* 2005, Vol. 88, 3, p. 599–603.
139. *The Determination and Interpretation of Viscosity in Sintering Systems.* **S.-H. Lee, A. Mohanram, G. L. Messing, D. J. Green.** University Park, PA, USA : s.n., Sept. 15-17, 2003. An International Conference on the Science, Technology & Applications of Sintering.
140. **P. Z. Cai, G. L. Messing, D. L. Green.** Constrained Densification of Alumina/Zirconia Hybrid Laminates, II: Viscous Stress Computation. *Journal of the American Ceramic Society.* 1997, Vol. 80, 8, p. 1940–1948.
141. **Tekeli, S.** Influence of alumina addition on grain growth and room temperature mechanical properties of 8YSCZ/Al2O3 composites. *Composites Science and Technology.* 2005, Vol. 65, p. 967–972.
142. **A. A. E. Hassan, N. H. Menzler, G. Blass, M. E. Ali, H. P. Buchkremer, D. Stöver.** Influence of alumina dopant on the properties of yttria-stabilized zirconia for SOFC applications. *Journal of Material Science.* 2002, Vol. 37, p. 3467 – 3475.
143. **Tekeli, S.** The solid solubility limit of Al2O3 and its effect on densification and microstructural evolution in cubic-zirconia used as an electrolyte for solid oxide fuel cell. *Materials and Design.* 2007, Vol. 28, p. 713–716.

144. **O. Kesler, R. L. Landingham.** Improvements in Mechanical Behaviour of SOFC Anodes. *Material Research Society Symposium Proceedings.* 2003, Vol. 756, p. FF3.10.1 - 6.
145. *SOFC Research and Development at NIMTE.* **W. G. Wang, W. B. Guan, H. M. Li, Y. J. Xue, J. X. Wang, Y. N. Wu, J. Wang, K. Liu.** Lucerne, CH : s.n., 30 June – 4 July 2008. Proceedings of the 8th European Solid Oxide Fuel Cell Forum.
146. **P. H. Larsen, C. Chung, M. Mogensen.** *Redox-stable anode. WO patent 2006079558*
147. **C.M. Finnerty, N.J. Coe, R.H. Cunningham, R.M. Ormerod.** Carbon formation on and deactivation of nickel-based/zirconia anodes in solid oxide fuel cells running on methane. *Catalysis Today.* 1998, Vol. 46, p. 137-145.
148. **T. Takeguchia, R. Kikuchia, T. Yanoa, K. Eguchi, K. Murata.** Effect of precious metal addition to Ni-YSZ cermet on reforming of CH4 and electrochemical activity as SOFC anode. *Catalysis Today.* 2003, Vol. 84, p. 217-222.
149. **N. Nakagawa, H. Sagara, K. Kato.** Catalytic activity of Ni-YSZ-CeO2 anode for the steam reforming of methane in a direct internal-reforming solid oxide fuel cell. *Journal of Power Sources.* 2001, Vol. 92, p. 88 – 94.
150. **J. Qiao, K. Suna, N. Zhang, B. Suna, J. Kong, D. Zhoua.** Ni/YSZ and Ni–CeO2/YSZ anodes prepared by impregnation for solid oxide fuel cells. *Journal of Power Sources.* 2007, Vol. 169, p. 253–258.
151. **D. Ravi, D. J. Green.** Sintering stresses and warpage produced by density differences in bi-layer structures. *Journal of the European Ceramic Society.* 2006, Vol. 26, p. 17–25.
152. **O. Guillon, J. Rödel, R. K. Bordia.** Effect of Green-State Processing on the Sintering Stress and Viscosity of Alumina Compacts. *J. Am. Ceram. Soc.* 2007, Vol. 90, 5, p. 1637–1640.
153. **G. Yan, Z. Fu Quiang, H. Hui, Z. Yuan Li, L. Ying.** Sintering behavior of Y-doped ZrO2 ceramics: the effect of additive rare earth oxides. *Journal of Ceramic Processing Research.* 2008, Vol. 9, 3, p. 311-316.
154. **S. M. Salamone, L. C. Stearns, R. K. Bordia,M. P. Harmer.** Effect of Rigid Inclusions on the Densification and Constitutive Parameters of Liquid-Phase-Sintered YBa2Cu3O6+x Powder Compacts. *Journal of the American Ceramic Society.* 2003, Vol. 86, 6, p. 883–92.
155. **F. P. Beer, E. R. Johnston Jr.** *Mechanics of Materials.* New York : McGraw-Hill, 1992.

156. **A. Dhir, K. Kendall.** Microtubular SOFC anode optimisation for direct use on methane. *J. Power Sources.* 2008, Vol. 181, p. 297–303.
157. **F. Tietz, H.- P. Buchkremer, D. Stöver.** Components manufacturing for solid oxide fuel cells. *Solid State Ionics.* 2002, Vol. 152– 153, p. 373–381.
158. **J–J. Sun, Y-H. Koh, W-Y. Choi, H-E. Kim.** Fabrication and Characterization of Thin and Dense Electrolyte-Coated Anode Tube Using Thermoplastic Coextrusion. *Journal of the American Ceramic Society.* 2006, Vol. 89, p. 1713–1716.
159. **T. Suzuki, T. Yamaguchi, Y. Fujishiro, M. Awano.** Fabrication and characterization of micro tubular SOFCs for operation in the intermediate temperature. *Journal of Power Sources.* 2006, Vol. 160, p. 73–77.
160. **Z. Cai, T.N. Lan, S. Wang, M. Dokiya,.** Supported Zr(Sc)O2 SOFCs for reduced temperature prepared by slurry coating and co-firing. *Solid State Ionics.* 2002, Vol. 152– 153, p. 583– 590.
161. **Y. Zhang, J. Gao, D. Peng, M. Guangyao, X. Liu.** Dip-coating thin yttria-stabilized zirconia films for solid oxide fuel cell applications. *Ceramics International.* 2004, Vol. 30, p. 1049-1053.
162. **Y. Zhang, J. Gao, G. Meng, X. Liu.** Production of dense yttria-stabilized zirconia thin films by dip-coating for IT-SOFC applications. *Journal of Applied Electrochemistry.* 2004, Vol. 34, p. 637 – 641.
163. **X. Changrong, C. Huaqiang, W. Hong, Y. Pinghua, M. Guangyao, P. Dingkun.** Sol-gel synthesis of yttria stabilized zirconia membranes through controlled hydrolysis of zirconium alkoxide. *Journal of Membrane Science.* 1999, Vol. 162, p. 181-188.
164. **K. Mehta, R. Xu, A. V. Virkar.** Two-Layer Fuel Cell Electrolyte Structure by Sol-Gel Processing. *Journal of Sol-Gel Science and Technology.* 1998, Vol. 11, p. 203–207.
165. **U. B. Pal, S. C. Singhal.** Electrochemical Vapor Deposition of Yttria-Stabilized Zirconia Films. *Journal of the Electrochemical Society.* 1990, Vol. 137, p. 2937-2941.
166. **K-W. Chour, J. Chen, R. Xu.** Metal-organic vapor deposition of YSZ electrolyte layers for solid oxide fuel cell applications. *Thin Solid Films.* 1997, Vol. 304, p. 106-112.
167. **S. P. Krumdieck, O. Sbaizero, A. Bullert, R. Raj.** YSZ layers by pulsed-MOCVD on solid oxide fuel cell electrodes. *Surface Coating Technology.* 2003, Vol. 167, p. 226-233.
168. **T. H. Shin, J. H. Yu, S. Lee, I. S. Han, S. K. Woo, B. K. Jang, S-H. Hyun.** Preparation of YSZ Electrolyte for SOFC by Electron Beam PVD. *Key Engineering Materials.* 2006, Vol. 317-318, p. 913-916.